Report
R-19-01
April 2019

Upscaling of brittle deformation zone flow and transport properties

Steven Baxter
Lee Hartley
Jaap Hoek
Simon Myers
Vasileios Tsitsopoulos
Thomas Williams

SVENSK KÄRNBRÄNSLEHANTERING AB

SWEDISH NUCLEAR FUEL
AND WASTE MANAGEMENT CO

Box 3091, SE-169 03 Solna
Phone +46 8 459 84 00
skb.se

SVENSK KÄRNBRÄNSLEHANTERING

ISSN 1402-3091
SKB R-19-01
ID 1704928

April 2019

Upscaling of brittle deformation zone flow and transport properties

Steven Baxter, Lee Hartley, Jaap Hoek, Simon Myers,
Vasileios Tsitsopoulos, Thomas Williams

Wood

This report concerns a study which was conducted for Svensk Kärnbränslehantering AB (SKB). The conclusions and viewpoints presented in the report are those of the authors. SKB may draw modified conclusions, based on additional literature sources and/or expert opinions.

A pdf version of this document can be downloaded from www.skb.se.

© 2019 Svensk Kärnbränslehantering AB

Sammanfattning

En förståelse för egenskaperna hos naturliga sprickor är ett grundläggande krav för att kunna göra en bedömning av den långsiktiga säkerheten av ett kärnbränsleförvar i kristallint berg med låg permeabilitet såsom för de planerade förvaren i Forsmark (Sverige) eller i Olkiluoto (Finland). Grundvattenflödet genom de öppna sprickorna i det sammanlänkade nätverket i berggrunden är den dominerande vägen för transport av eventuella frigjorda radionuklider. De geometriska, hydrauliska och mekaniska egenskaperna hos sprickor är också relevanta vid planering av anläggning och drift av ett kärnbränsleförvar; detta genom egenskapernas koppling till hantering av vatteninflöde och berggrundstabilitet. Vidare är sprickegenskaperna viktiga för operativa förfaranden vid bestämning av förvarsvolymer och för förslutningsdesign. Av dessa skäl är en kvantitativ beskrivning och analys av sprickor en viktig komponent i både SKB:s och Posivas program.

I samråd med SKB har Posiva utvecklat sin metodologi för diskret spricknätverksmodellering (engelska: Discrete Fracture Network – DFN) till stöd för Olkiluotos platsbeskrivande modell (SDM) 2018. DFN-metodiken har utvecklats på flera sätt för att uppnå en större integration mellan geologiska sub-modeller (duktila domäner, litologi och spröda deformationszoner) och hydrogeologiska modeller; detta med syfte att minska osäkerheten i platsspecifika prediktioner. Det kan emellertid vara svårt att kommunicera de effektiva egenskaperna hos dessa komplexa modeller inklusive deras känslighet för osäkra DFN-parametrar såsom storleksfördelning och intensitet. Därför inkluderar denna studie även utvecklingen av metoder för uppskalning av komponenter i en DFN-modell till en förenklad representation av viktiga egenskaper; detta antingen genom att härleda ekvivalenta kontinuerliga porösa mediumegenskaper (ECPM) på lämplig upplösning, eller genom att förenkla representationen av sprickzoner modellerade som en svärm av sprickor till ekvivalenta plan-projicerade egenskaper. De viktigaste metodologiutvecklingarna i denna studie är:

1. En metodologi för att beräkna geocellulära transportparametrar (advektiv gångtid och flödesrelaterad transportmotstånd) och deras statistik genom att utföra en ensemble av flödes- och transportberäkningar inom varje ECPM-gridelement och att använda dessa för att härleda ECPM-sprickegenskaper i både bergmassa och sprickzoner.
2. En metodologi för att projicera dessa ECPM-egenskaper på mittplanet av sprickzoner, så att effektiv transmissivitet, transportapertur, flödesvätteyta samt tjocklek erhålls.
3. En metodologi för att beräkna den rumsliga statistiken för de effektiva egenskaperna på sprickzoners mittplan och vidare att möjliggöra en effektiv generering av multipla realiseringar av transmissivitet och porositet för att kunna bedöma stokastisk osäkerhet utan att behöva beräkna och skala upp multipla DFN-realiseringar.

För var och en av dessa tre utvecklingar görs jämförelser och bekräftande test inom ramen för Posiva ODFN 3.0-modellen; detta för att bedöma användbarheten och användningspotentialen av prototyp-metoderna i framtida DFN-modellering till stöd för SKB:s program.

Abstract

An understanding of the properties of natural fractures is a fundamental requirement for a performance assessment of the long-term safety of a spent nuclear fuel repository located in low permeability crystalline rocks such as those at Forsmark, Sweden or Olkiluoto, Finland. Groundwater flow through the void space of the interconnected fractures in the bedrock is the dominant pathway for the migration of any arising radionuclides. Geometric, hydraulic and mechanical properties of fractures are also relevant to planning the construction and operation of a disposal facility, through their implications for managing water inflows and bedrock stability. Furthermore, related fracture characteristics are important to operational procedures for determining disposal volumes and to the closure design. For these reasons, a quantitative description and analysis of fracturing is an important component of both the SKB and Posiva programmes.

In consultation with SKB, Posiva have been developing their methodology for discrete fracture network (DFN) modelling in support of the Olkiluoto site descriptive model (SDM) 2018. The DFN methodology has been elaborated in several ways in order to achieve greater integration between geological sub-models (ductile domains, lithology, and brittle deformation zones) and hydrogeological models, aimed toward reducing the uncertainty of location specific predictions. However, it can be difficult to communicate the effective properties of these elaborated models, including their sensitivities to uncertain DFN parameters such as size distribution and intensity. As such, this study details the development of methodologies to upscale components of DFN models to a simplified representation of key features, either by deriving equivalent continuous porous medium (ECPM) properties on a suitable grid, or by simplifying the representation of fault zones modelled as swarms of fractures to equivalent properties on a planar representation. The key methodological developments in this study include:

1. An approach to accurately calculate geocellular transport parameters (travel time and flow-related transport resistance) and their statistics by carrying out an ensemble of flow and transport calculations within each ECPM grid element, and to use these to derive ECPM properties for fracturing in both the rock mass and fault zones.
2. An approach to project these ECPM properties onto the mid-plane of fault zones, providing effective transmissivity, transport aperture, and flow wetted surface, as well as thickness.
3. An approach to calculate the spatial statistics of the effective properties on the fault zone mid-planes and to enable the efficient generation of multiple realisations of transmissivity and porosity, to assess stochastic uncertainty without having to run and upscale many DFN realisations.

For each of these three developments, comparison/confirmatory tests are made within the framework of the Posiva ODFN 3.0 model, to assess the applicability and potential for use of the prototyped methodologies in future DFN modelling in support of the SKB programme.

Contents

1 Introduction 7
1.1 The Olkiluoto site 8
1.1.1 Brittle deformation zones 8
1.2 Objectives of this study 12
1.3 Report structure 12

2 Conceptual models of fracturing at Olkiluoto 13
2.1 Structural model of fracturing at Olkiluoto in the rock mass 13
2.1.1 Sets and orientations 13
2.1.2 Location model and intensity-size 14
2.1.3 Illustrations 14
2.2 Structural model of brittle fault zones (BFZ) at Olkiluoto 15
2.2.1 Fracture zones versus mid-planes 15
2.2.2 Structural conceptualisations 15
2.2.3 Illustrations 18
2.3 Hydraulic conceptualisations 20
2.3.1 Spatial distribution of openings 20
2.3.2 Aperture distribution and hydromechanics 23

3 ECPM upscaling of flow and transport properties 27
3.1 Flux-based upscaling methodology 27
3.2 Transport-based upscaling methodology 29
3.2.1 Geometric-based transport upscaling 29
3.2.2 Flow-based transport upscaling 29
3.3 Evaluation of transport-based upscaling 31
3.3.1 Dependence on cell size 31
3.3.2 Dependence on depth and method 38
3.4 Example results for Olkiluoto 44
3.4.1 Comparison of kinematic porosities 44
3.4.2 Comparison of pathways 50

4 Upscaling and projection of BFZ flow and transport properties 59
4.1 Integrating BFZ with ECPM models of Olkiluoto site 59
4.1.1 Downscaling of brittle fracture zones 59
4.1.2 Upscaling BFZ to planar properties 60
4.2 Example results for Olkiluoto 65
4.2.1 Island scale flows 74
4.2.2 Pathline comparison through BFZ 74

5 Geostatistical models of planar BFZ 81
5.1 The geostatistical approach for simulating BFZ 81
5.1.1 Generation of variograms 83
5.2 Example results for Olkiluoto 85
5.2.1 Geostatistics based on the measured data 85
5.2.2 Geostatistics based on the upscaled fault zones 87

6 Summary and conclusions 97
6.1 Transport-based upscaling 97
6.2 Plane upscaling of BFZ properties 98
6.3 Geostatistical models for planar BFZ 99

References 101

1 Introduction

An understanding of the properties of natural fractures is a fundamental requirement for a performance assessment of the long-term safety of a spent nuclear fuel repository located in low permeability crystalline rocks such as those at Forsmark, Sweden (Joyce et al. 2010) or Olkiluoto, Finland (Hartley et al. 2012). Groundwater flow through the void space of the interconnected fractures in the bedrock is the dominant pathway for the migration of any arising radionuclides. Geometric, hydraulic and mechanical properties of fractures are also relevant to planning the construction and operation of a disposal facility, through their implications for managing water inflows and bedrock stability. Furthermore, related fracture characteristics are important to operational procedures for determining disposal volumes and to the closure design. For these reasons, a quantitative description and analysis of fracturing is an important component of both the SKB and Posiva programmes.

For large scale structural features such as brittle deformation zones, fracturing can typically be described deterministically based on an integration of geophysical, surface-based drillholes, monitoring, and underground characterisation. For all other fractures it is either not practical or impossible to determine their properties, and so they are described in terms of probability distributions, geostatistical models or as correlations. Such a treatment is necessary to predict fractures between drillholes and underground openings below the resolution of geophysical methods. Such fractures can then either be modelled as a statistical equivalent set of fractures with all properties sampled; or stochastic conditioning methods could be used to assign the undetermined properties to each observed fracture.

In consultation with SKB, Posiva have been developing their methodology for DFN modelling toward the Olkiluoto site descriptive model (SDM) 2018. The DFN methodology has been elaborated to achieve greater integration between geological sub-models (ductile domains, lithology, and brittle deformation zones) and hydrogeological models. One key element of these methodology changes is the integration of structural/geometrical DFN descriptions with hydrogeological ones into a single DFN model covering both aspects. This philosophy has been applied to both the representation of brittle deformation zones (referred to in Posiva terminology as “brittle fault zones” [BFZ]; this term is used interchangeably with “brittle deformation zones” in this report) and to the rock mass between them.

In the new methodology, BFZ are modelled as zones of individual fractures each having their properties sampled from statistical distributions rather than being modelled as a single triangulated plane (or surface) with effective hydraulic and transport properties (Hartley et al. 2012). Stochastically generated fault related fractures are located around the core of each fault according to an exponential distribution of fracture centres around the core, with a defined intensity at the core and a decay of intensity according to distance from the core. The resulting DFN models associated with each BFZ better reflect the structural geology observed around faults, and capture much of the site data including spatial distribution, intensity, orientation, traces in tunnel, as well as magnitudes of flow. Representing the BFZ in this way provides a consistent approach to the description of connectivity, hydraulic properties, anisotropy and heterogeneity, as well as transport properties. This consistency between the representation of fractures in the BFZ and remaining rock mass is a key improvement over previous DFN models, enabling unified data analysis, calibration and prediction methodologies to be applied across the whole rock volume.

Although this methodology is an improvement in many aspects, it carries an increased computational cost; for example, it is likely not feasible to use the explicit swarm representation of BFZ to carry out all of the site-scale particle tracking transport calculations required in a typical safety assessment. Thus, a need arises for reducing the computational burden of transport calculations while preserving as much as possible the desirable features of the swarm representation, such as its small-scale heterogeneity structure and directionality. One method for reducing computational cost is to map fracture network properties, using appropriate upscaling methods, to equivalent continuous porous medium (ECPM) hydraulic conductivities, kinematic porosities and flow wetted surface area per unit volume for a defined scale or grid. When applied to BFZ, this provides a hydraulic and transport description that can be modelled as either explicit DFN or ECPM, depending on the requirements of end-users.

The upscaling method previously implemented in the ConnectFlow groundwater modelling software suite (Wood 2016a) to calculate the transport properties of each grid cell uses simple geometric approximations that do not reflect the effects of heterogeneity, channelling or hydraulic gradient.

A better approach, developed as part of this study, is to use flow paths through each grid cell to obtain a distribution of travel times, tortuosity and flow resistance for each direction and each element, which can subsequently be used to derive anisotropic values of equivalent porosity and flow wetted surface area for the grid cells, reflecting more accurately the underlying transport behaviour of the DFN.

While an ECPM representation decreases computational cost, it can be difficult to communicate the properties this representation implies and the sensitivity of those properties to uncertain DFN parameters such as size distribution and intensity. Related to this is the issue of how to parameterise models of BFZs where the end-user requires a simplification of the zone to a plane with effective properties (transmissivity, porosity, and flow wetted surface). A further issue is how to extrapolate property descriptions derived for well characterised BFZ to those BFZ that only have limited or no borehole intersections (e.g. interpreted from 3D seismic alone or magnetic lineaments), or for stochastically generated BFZ that will be required for describing far-field flow and transport.

As a response to these issues, a novel method is developed as part of this study to project averaged ECPM properties onto the mid-plane of a BFZ fault, returning to a planar representation but retaining spatial heterogeneity of transmissivity and porosity across the two-dimensional surface. An important benefit of such a representation is that it enables the use of geostatistical methods to generate multiple realisations of transmissivity and porosity as an expedient way to assess stochastic uncertainty (i.e. without having to run and upscale several DFN realisations), thus significantly reducing the computational effort involved.

1.1 The Olkiluoto site

Olkiluoto is an island (~10 km^2) on the Baltic Sea coast and separated from the mainland by a narrow strait. The Olkiluoto nuclear power plant, with two reactors in operation, a third under construction, as well as the VLJ repository for low and intermediate-level waste, is located in the western part of the island. It is intended that the repository for spent nuclear fuel will be constructed in the central and eastern part of the island, see Figure 1-1.

A site characterisation programme at Olkiluoto has been taking place for over 30 years by means of ground- and air-based methods, from shallow and deep (300–1 000 m) drillholes and from the ONKALO, providing an ever-increasing level of confidence in the Olkiluoto Site Description. Supplementary site investigations are still being carried out, both from the surface and from the ONKALO.

The underground parts of the ONKALO consist of an access tunnel and shaft from which a system of characterisation and demonstration tunnels are accessed. The main characterisation level is located at a depth of about 420 m. Demonstrations and tests of repository technologies are mainly carried out at the main characterisation level, but characterisation of the rock mass has already taken place during the excavation, using pilot holes drilled along parts of the tunnel axis (prior to its excavation), by tunnel mapping, by monitoring the impact of construction, and in special investigation niches.

1.1.1 Brittle deformation zones

As part of the current Olkiluoto site description, Version 3 of the Olkiluoto brittle fault zone (BFZ) model has been developed, and consists of 299 core volumes of BFZs defined by Surpac string and digital terrain model files (see Figure 1-2). The lateral extents of these structures are defined by both the intersection of BFZs with drillholes as well as seismic P-Wave (compression), resistivity and magnetic measurements. A complimentary table of all the drillhole intersects with the BFZs is also available and includes: core and damage zone thicknesses, style of deformation (brittle fault, brittle joints, semi-brittle), overall orientation of the fault plane, and kinematic sense of movement. Two horizontal slices through this BFZ model, one taken near ground level, the other at –420 m, are shown in Figure 1-3. In the well-characterised area towards the centre and east of Olkiluoto Island, where drilling and the ONKALO construction have confirmed the existence of structures, a higher intensity of interpreted small scale BFZ is clearly evident; this is an artefact of the increased density of drillhole data, which is addressed in Hartley et al. (2018) by the stochastic generation of additional BFZ planes outside the well-characterised area.

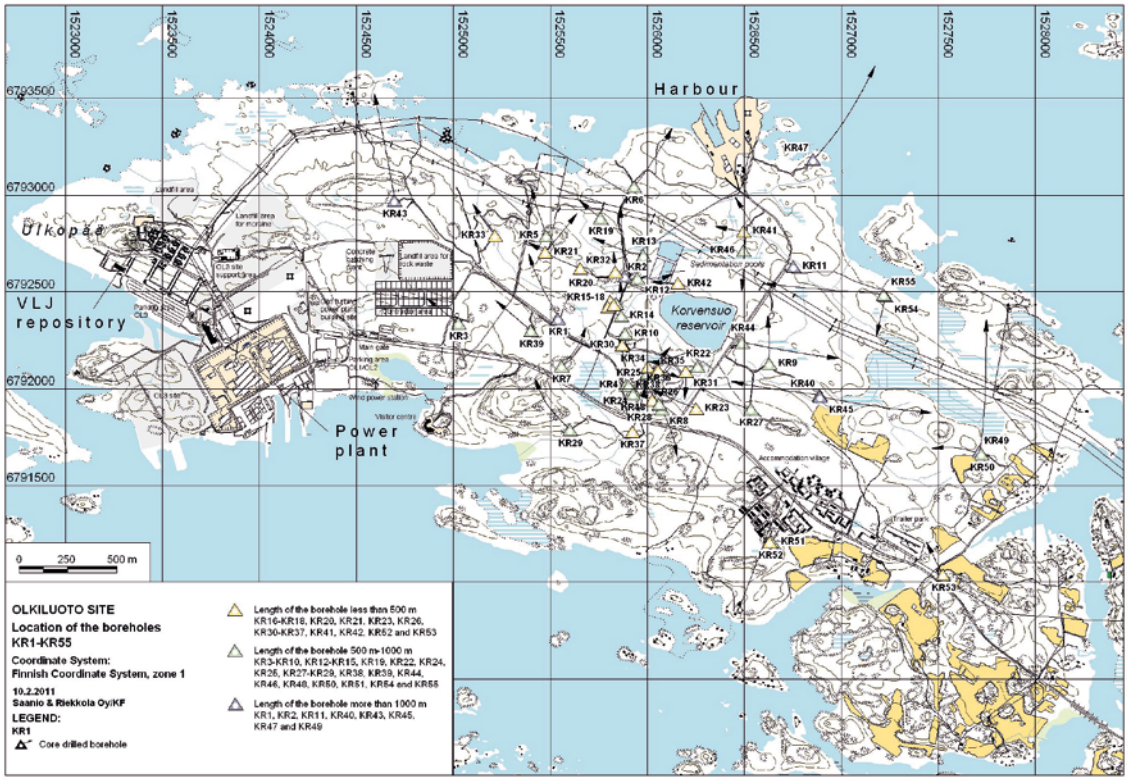

Figure 1-1. *Locations of the site drillholes (triangles) at Olkiluoto. The grid squares are of side 500 m.*

For numerical modelling purposes, the BFZ Version 3 model has also been delivered as a set of mid-planes through the centre of the core for 298 out of the 299 fault zones. The zone excluded from numerical modelling is BFZ102, which is a strongly altered ductile shear zone at shallow depths and gently dipping, forming a complex non-tabular geometry without any clear core.

In this study, six of the well characterised BFZ are selected for further investigation and to prototype the methodology for upscaling flow and transport properties of deformation zones. These are

- BFZ020a: a hydraulically active fault zone dipping to the Southeast with high transmissivity (significantly higher than the average) ~10^{-6} m^2/s at repository depth.
- BFZ045: a vertical fault identified as hydraulically active and cutting through the proposed repository layout. Associated with HZ056 from the hydrostructural model (Vaittinen et al. 2019).
- BFZ084: a sub-vertical fault steeply dipping to the South and cutting through the proposed repository layout. This fault is also associated with HZ056 from the hydrostructural model (Vaittinen et al. 2019).
- BFZ099: a sub-vertical hydraulically active major fault zone dipping to the Southeast and bounding the northern extent of the proposed repository layout.
- BFZ100: a hydraulically active vertical fault cutting the proposed repository layout.
- BFZ146: a fault zone dipping to the South and bounding the southern extent of the proposed repository layout. Similarly to BFZ020a, this fault zone is observed to have distinctly higher transmissivities than most of the faults at Olkiluoto.

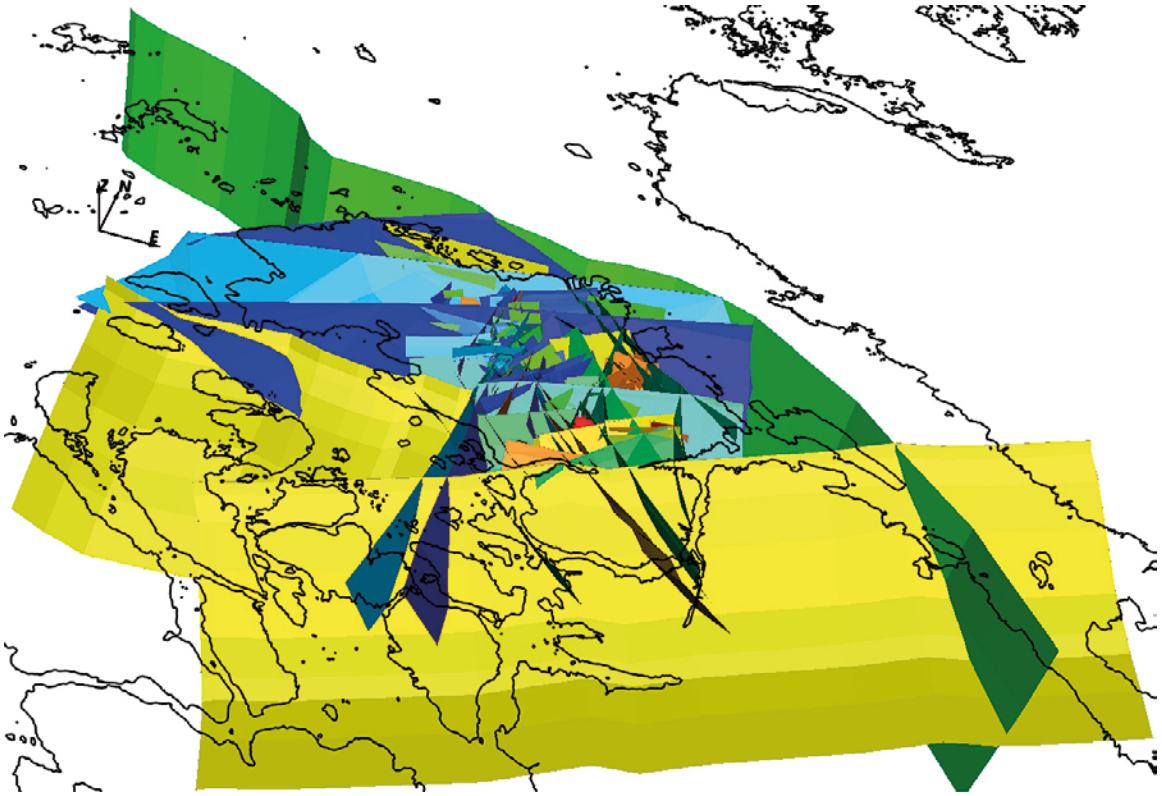

Figure 1-2. *Version 3 of the Brittle Fault Zone model, viewed from above and to the southeast. This figure is reproduced from Hartley et al. (2018).*

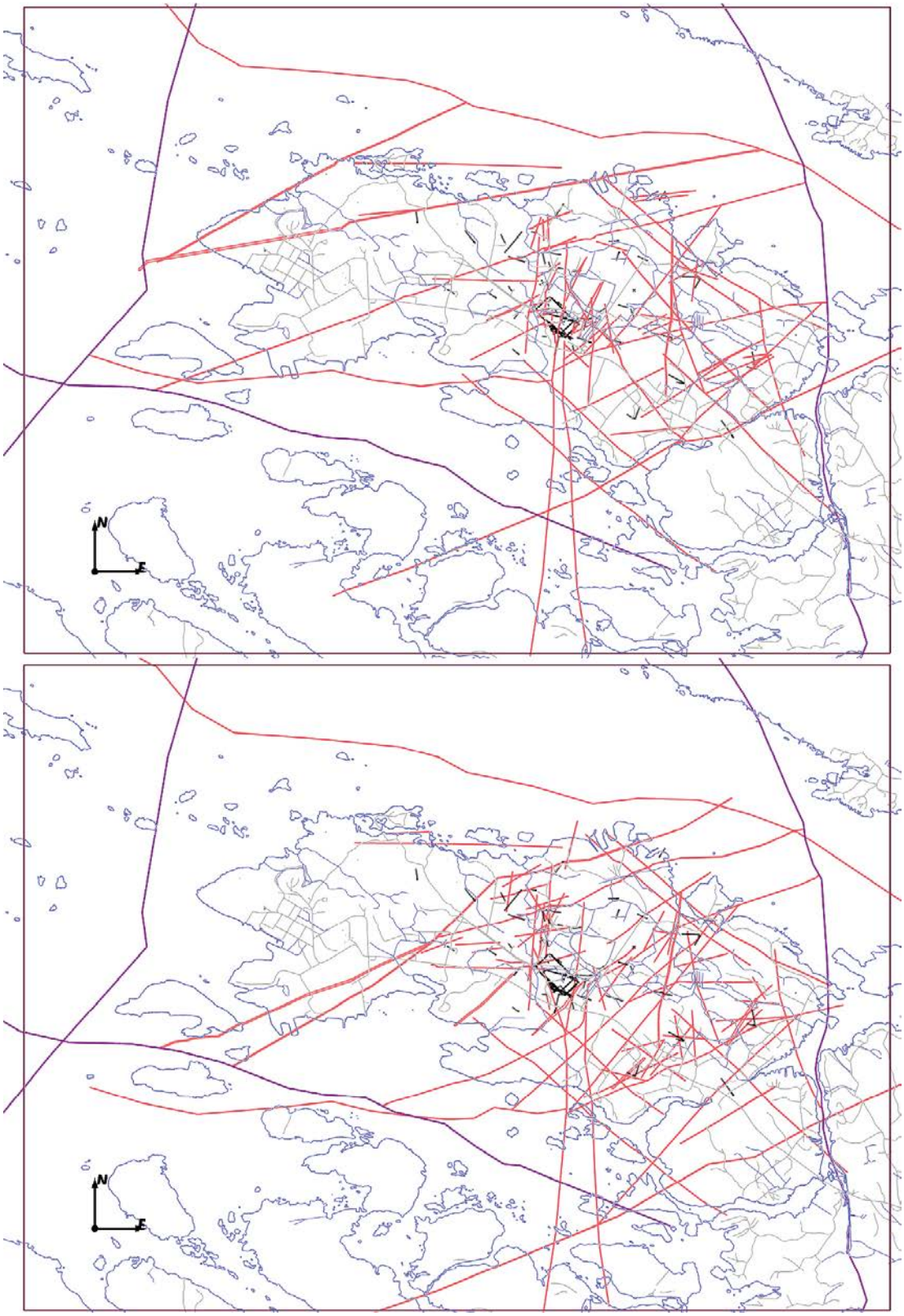

Figure 1-3. *Slices through BFZ model v3 (red) at –10 m (top) and –420 m (bottom) with the site-scale boundary (brown), 3 bounding lineaments (purple), and drillholes (black). This figure is reproduced from Hartley et al. (2018).*

1.2 Objectives of this study

The objectives of this study are to:

1. Provide a methodology to derive accurate geocellular transport properties (travel time and flow-related transport resistance) and their statistics, and to use these to derive ECPM properties for both the background fractures and BFZ.
2. Project the upscaled properties onto the mid-planes of each of the fault zones, providing values for the effective transmissivity, transport aperture, and flow wetted surface, as well as thickness. This will provide an alternative method for modelling BFZ within either simplified DFN models or ECPM models.
3. Analyse the variability in the effective transmissivity and porosity calculated on the fault zone mid-plane, and to provide a geostatistical model for these properties. Such a model enables the generation of realisations of transmissivity and porosity as an expedient way to assess stochastic uncertainty (i.e. without having to run and upscale several DFN realisations).

For each of the above objectives, this report documents the proposed methodology; example application within the framework of Posiva's ODFN 3.0 model; and comparison/confirmatory tests for a number of the layout-critical faults.

1.3 Report structure

The workflow and modelling performed in this study for the achievement of the objectives are reported in the following chapters:

- The conceptual models developed for describing the geometric and hydraulic properties of BFZ as part of Posiva's ODFN 3.0 model are detailed in Chapter 2.
- Chapter 3 presents an approach for transport-based upscaling of DFN models to equivalent porous media properties (corresponding to Objective 1 above).
- Algorithms for projecting the transport upscaled BFZ models onto the mid-planes of the core of the fault zones are detailed in Chapter 4 (corresponding to Objective 2 above).
- Spatial statistics for the effective properties upscaled onto the mid-planes of the fault zones are presented in Chapter 5 (corresponding to Objective 3 above) and used to represent stochastic uncertainty in these effective properties.
- Chapter 6 summarises the key conclusions from this study.

2 Conceptual models of fracturing at Olkiluoto

In consultation with SKB, Posiva have been developing their methodology for DFN modelling toward the Olkiluoto site descriptive model (SDM) 2018. The DFN methodology provides integration between geological sub-models (ductile domains, lithology, and brittle deformation zones) and hydrogeological models to form a single DFN model, denoted ODFN 3.0. This philosophy has been applied to both the representation of brittle deformation zones and to the rock mass between BFZ. In the latest methodology, BFZ are modelled as zones of individual fractures each having their properties sampled from statistical distributions. This is in contrast to previous DFN modelling of the site which included BFZ as a single triangulated plane (or surface) with effective hydraulic and transport properties (Hartley et al. 2012). In this chapter, the ODFN 3.0 models for Olkiluoto are synthesised, providing a summary of the work reported in Hartley et al. (2018) and for further information the reader is referred to this study. It is noteworthy, however, that this study was performed alongside the development of ODFN 3.0, and as such the model parameterisation used herein will not necessarily correspond directly to the final calibrated ODFN 3.0 model.

- Section 2.1 provides a review of the structural model of fracturing in the rock mass of Olkiluoto between BFZ. Although the focus of this study is on the upscaling of BFZ properties, some of the confirmatory tests and example analyses presented in later chapters of this report apply to the full ODFN 3.0 model (i.e. including fractures in the rock mass as well as BFZ). Therefore it is beneficial for the reader to have a brief understanding of how fracturing in the rock mass is represented within ODFN 3.0.
- Section 2.2 provides a detailed synthesis of the BFZ modelling applied in ODFN 3.0, including a review of the conceptual developments made since previous versions of the DFN model. In particular the benefits of representing the BFZ as a clustering of individual fractures in contrast to single tabular structures are presented.
- Section 2.3 reviews the hydraulic description for fractures at Olkiluoto both associated with the rock mass and BFZ. This includes a description of fracture openings as well as the dependence of fracture aperture on stress.

2.1 Structural model of fracturing at Olkiluoto in the rock mass

Hartley et al. (2018) identified geological models of ductile deformation and lithology as a tectonic framework for the description of heterogeneity in the background rock. Analysis performed therein determined correlations between the orientation (summarised in Subsection 2.1.1) and intensity-size (summarised in Subsection 2.1.2) of fractures with these geological properties and depth. The following presents only a synthesis of the final structural model developed, and for further details of the data and analysis underpinning this model the reader is referred to Chapters 2 through 6 of Hartley et al. (2018).

2.1.1 Sets and orientations

The structural model for ODFN 3.0 consists of six global sets (FP, NS, EW, EW_h, NE, NW) and three more sporadic moderately dipping sets (NS_moddip, NW_moddip, NE_moddip) for the bedrock outside of BFZ. The global sets are assumed pervasive throughout the modelling domain, although the relative intensity is adjusted to reflect both lateral and vertical variations in their measured relative importance. In contrast, the moderately dipping sets are restricted to lithology/ductile domain combinations where they occur in at least 50 % of drillholes and make up more than 5 % of the relative fracture intensity. This limits the NS_moddip and NW_moddip sets to only a handful of the lithologies, ductile domains and depths considered; whilst the NE_moddip can be neglected by these criteria.

In the modelling, a 3D map is constructed of the variation in mean pole across all lithology/ductile domains and depths for each global set using inverse distance weighting interpolation between drillhole/tunnel data. For moderately dipping sets, piecewise constant mean poles were used. A Fisher distribution is used for each set and domain. Fracture generation is then performed using geocellular models (or 3D maps) of the ductile domain and lithological properties of the bedrock with the appropriate interpolated mean pole used to sample fractures within each of the geocells in turn.

2.1.2 Location model and intensity-size

The intensity, P_{32}, of background fractures is heterogeneous varying by lithology, ductile domain and depth. Similarly to the orientation model, spatial variation in intensity is represented by a geocellular grid of the lithology and ductile domains at Olkiluoto. In order to capture the interpreted dependence of intensity on lithology, a geocell size of 10 m is used in the central well characterised area so as to capture the effects of several thin lithological bodies/lenses that occur within the geological model. The total intensity is divided between the six global and two modelled moderately dipping sets (see Subsection 2.1.1) which also varies by ductile domain and depth. Hence, the geocellular values of total intensity are multiplied by the fractions belonging to each orientation set, providing the relative intensity to be used to generate a particular orientation of fractures in each geocell.

The intensity-size parameters restrict the fractures to a certain size window for practical reasons. The maximum size for individual fractures is set to r_{max} = 113 m, as being a conceptual transition between fractures and fracture zones. The smallest fractures generated, r_{min}, could in theory be equal to the location parameter, r_0, but this would give a DFN model too large to compute. For site-scale modelling, the minimum size of fractures generated throughout the rock mass, $r_{min\text{-}ss}$, is set to 7 m, giving about 50 million background fractures (prior to removal of sealed parts) to represent the main backbone of the water conducting network between BFZs. For simulated drillholes or tunnels, such a limit could significantly reduce the connectivity between such features and the network, and for example could lead to under-prediction of pumped inflows. Therefore a smaller truncation is used, $r_{min\text{-}dh}$ = 1 m within cylindrical volumes of radius 20 m around every drillhole and tunnel which is represented in the model. This adds an extra 4 million localised small fractures to the site-scale model.

2.1.3 Illustrations

Figure 2-1 shows a horizontal slice through part of a DFN realisation of the fractures in the rock mass at Olkiluoto at –420 m, with fractures coloured by set. The fracture swarms associated with BFZ are excluded. Only part of the model is shown near the base of the ONKALO over about a 500 m E-W scale so that individual fractures can be seen. Most of this area is either ductile region SDZ or CTU1, neither of which contain the moderately dipping sets, so only the six global sets are seen here. All fractures are shown according to the recipe for the geometric DFN parameters, and prior to the removal of any fracture area modelled as being sealed or of low transmissivity. As can be seen, most of the fracture area, except for the smaller ones, are connected under these conditions even at this depth. For this illustration, the size distribution is truncated at radius 1 m everywhere.

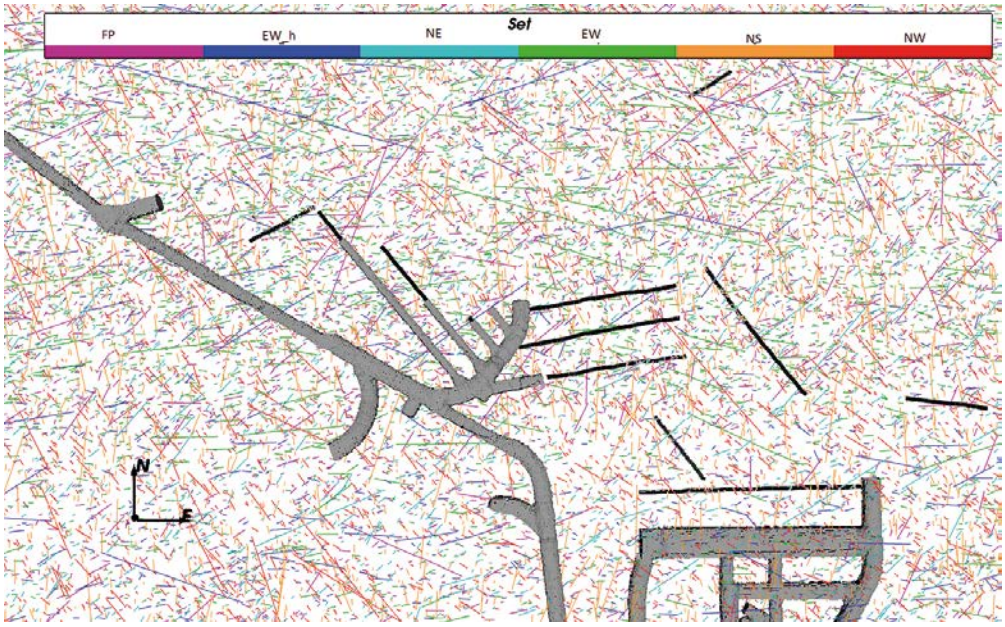

Figure 2-1. *A slice at z = –420 m through the DFN model of all fractures outside BFZ prior to removing sealed parts of fractures. The scale of the rock volume shown is 500 m E-W, and fractures are coloured by set. The ONKALO (grey) and drillhole (black) are shown. This figure is reproduced from Hartley et al. (2018).*

2.2 Structural model of brittle fault zones (BFZ) at Olkiluoto

2.2.1 Fracture zones versus mid-planes

The increased fracture intensity within the brittle deformation zones (BFZ) can make these features significant for flow and transport on the site-scale, affecting both the degree of connectivity and the available fracture surface area for diffusion and water-rock interaction processes. However, the DFN v2 fracture models (Hartley et al. 2012) did not include a description of fracture properties within the damage zone and core of the BFZ at Olkiluoto, instead representing the BFZ as semi-planar structures with effective properties. For hydrogeology, only a subarea were recognised as hydraulically active where they were confirmed as such by pumping, monitoring or groundwater sampling data, and denoted as hydrogeological zones (HZ) with latest interpretations by Vaittinen et al. (2019). These hydrogeological zones were then modelled as semi-planar features with effective transmissivity and storativity for flow simulations, and total aperture and fracture surface area per unit volume for transport. Modelling flow and transport as being limited to essentially single continuous planes may overly constrain the spatial distribution of flow, assume too much flow continuity within a zone, and underestimating both the fracture volume and flow wetted surface area and hence retardation processes.

An alternative methodology involves modelling of fault zones as tabular volumes within the rock mass containing fractures with potentially different properties, e.g. intensity and orientation. This approach was first considered in the prototype DFN study of the Demonstration Area (Hartley et al. 2017), limited to the detailed scale geological model of the Demonstration Area and technical facilities of the ONKALO on a characterisation scale of about 550 m × 550 m × 100 m. The methodology was further elaborated in ODFN 3.0 (Hartley et al. 2018) to consider all 298 BFZ within Version 3 of the deformation zone model. For each of these fault zones, relationships between properties of the individual fractures comprised by the fault (including flow properties) and the structural properties of the fault (such as size, thickness and orientation) were identified. By approaching the modelling of BFZ in this way, a number of the limitations in the DFN v2 model regarding flow and transport within fault zones are addressed. The following section provides further details on this conceptual methodology to modelling BFZ.

2.2.2 Structural conceptualisations

The concept of modelling BFZ as fracture swarms was prototyped in the Demonstration Area DFN study (Hartley et al. 2017), where an increase in fracturing within a fault zone was observed such that within the core of the fault, or within 2 m of it, the intensity was found to be approximately three times that of fracturing in the rock mass (i.e. in volumes away from BFZs). When considering all BFZs in the Demonstration Area, fracture intensity was also found to be about double the background within 5 m of the core. Even when excluding fractures within the interpreted BFZ damage zones, intensity was shown to be about 50 % higher within 5 m of the core of the fault zone. Much of this additional fracture intensity is made up of fractures sub-parallel to the general fault orientation, mostly within 30–40° of the fault plane. Hartley et al. (2017) also showed that a significant portion of water-conducting fractures (WCF) are concentrated in and around faults, with again about three times the intensity of WCFs in the remaining rock mass. This is most likely a direct consequence of the increased intensity of fracturing giving a higher probability of there being connected fractures. Although these statistics provide a general picture of fracturing within volumes of rock associated with fault zones, the Demonstration Area DFN study (Hartley et al. 2017) did not consider a detailed characterisation of individual BFZs, whose properties vary considerably in terms of thicknesses of core and damage zones, and the fracture intensities within them.

For ODFN 3.0, characterisation of the thickness and intensity of fractures relative to structural properties of each fault zone are quantified. A schematic of typical fault zone structures in a crystalline rock is shown in Figure 2-2 for both a single fault core and multiple fault cores, with associated damage zones. In addition, photographs of the fault zone BFZ100, a large steeply dipping fault repeatedly intersecting the ONKALO access tunnel, is shown in Figure 2-3 (reproduced from Aaltonen et al. (2016)) for intersection at chainages 520 m and 900 m. At both intersections, the core is clearly definable and transition zones are observed, although the core width is variable, ranging from a few tens of centimetres up to a couple of metres. Data available from Version 3 of the Olkiluoto BFZ model and supporting documentation is focussed primarily on the definition of this core of the fault structure. However, for characterising the flow associated with a fault zone, the damaged rock volume surrounding the

fault zone core is of particular interest. Interpretation of this damage zone at Olkiluoto is limited to estimations from geological investigations and recorded in the tabulation of drillhole/tunnel intersects. Specifically, flow measurements are not used in the definition of these damage zones.

Therefore, before characterising the properties of the individual fractures comprised by the fault (including their flow properties) to the structural properties of the fault zone itself, it is first appropriate to define an integrated damage zone for each BFZ structure considering both structural and hydraulic data. An iterative approach is used: first taking the original geologist's interpretations of the damage zone to see whether they are sufficient for partitioning fracture characteristics between inside/outside the fault, and extending where necessary to envelope additional nearby flows and fractures consistent with those in the original damage zone. Based on these integrated damage zones, statistics for thickness, intensity and flows within each fault zone are determined.

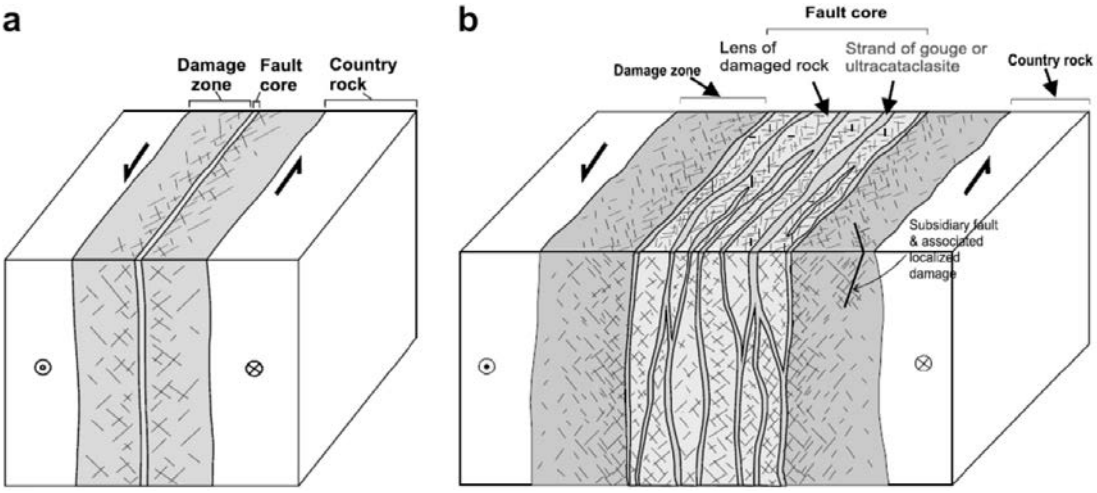

Figure 2-2. *Typical fault zone structure in crystalline rocks showing (a) a single fault core and (b) multiple fault cores, with associated damage zones. This figure is reproduced from Aaltonen et al. (2016).*

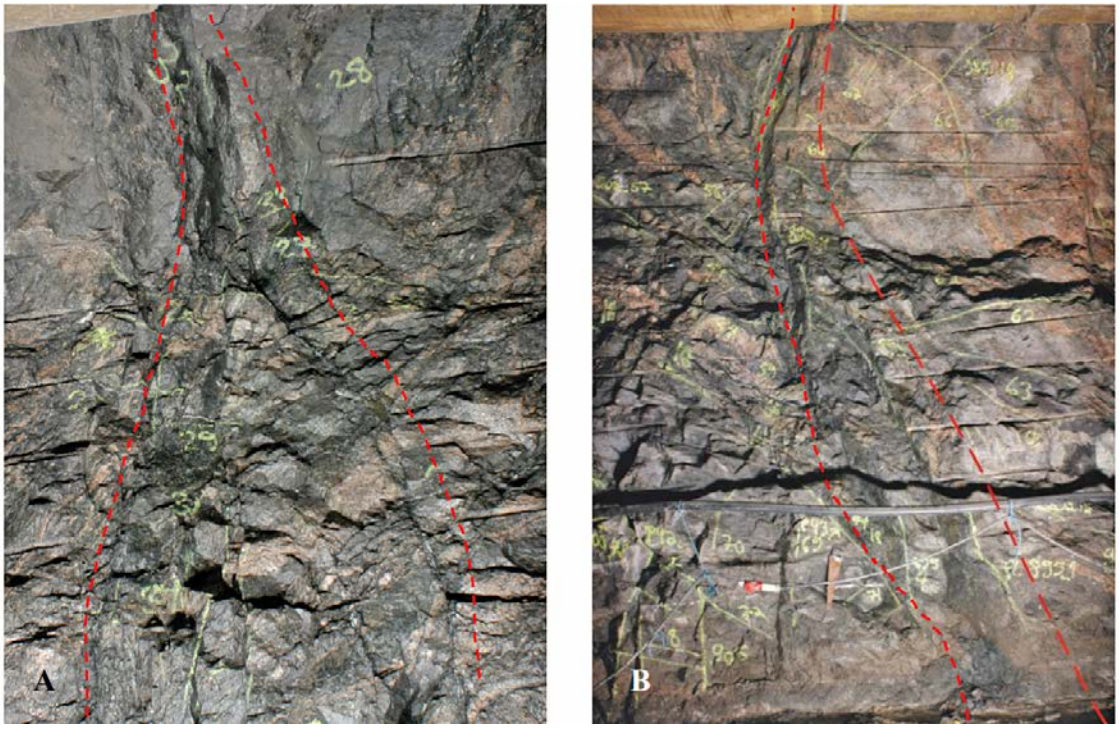

Figure 2-3. *A. Ol-BFZ100 in the left wall of the ONKALO access tunnel, chainage 520–524 m with a view approximately from the NE. B. OL-BFZ100 in the right wall of the ONKALO tunnel, chainage 900–905 m. The view is approximately from the SW. This figure is reproduced from Aaltonen et al. (2016).*

Based on the above analysis, the DFN models for BFZ are conceptualised as swarms of fractures generated stochastically around a deterministic mid-plane centred on the fault core and overlaying background fractures generated in the rock mass. A parent-daughter method (e.g. Al Qassab et al. 2002) is used whereby each fault zone is treated as a parent deterministic structure (defining location, extent, orientation and thickness) about which individual daughter stochastic fractures are generated. In this method, intensity at the core of the fault zone (defined by the triangulated mid-plane) is specified along with a length scale, λ, such that the intensity of fractures falls off with distance x from the mid-plane according to $\exp(-x^2/\lambda^2)$. The length scale is usually set to about one quarter of the thickness of the damage zone, but was calibrated by simulation in Hartley et al. (2018) to ensure the total Terzaghi corrected fracture count of fault related fractures at each BFZ drillhole intersect (averaged over 10 realisations of the model) matched the data. The parameters used in the parent-daughter method for generating fracture swarms around each fault zone are given in Table 2-1, including a general prescription for faults with no or limited drillhole intersects. For those fault zones with drillhole intersects, the calibrated intensity decay constant parameters are presented in Table 2-2.

Table 2-1. Parameter for generating fracture swarms using a parent-daughter method around each BFZ. This table is reproduced from Hartley et al. (2018).

BFZ parameter	Setting
Intensity, I_{gdz}	$I_{gdz} = 17.0 \times Log_{10}(strike\ length) - 34.9$
Damage zone thickness, w_{gdz}	If there are 2 or more drillhole intersects: Use IDW interpolation of both hanging wall and footwall, exponent 2 Else: $w_{gdz} = 11.5 \times Log_{10}(strike\ length) - 22$ Hanging wall = footwall
Intensity decay constant, λ	$0.34 \times w_{gdz}$, Length ≤ 1 000 m $0.28 \times w_{gdz}$, 1 000 m < Length ≤ 2 000 m $0.21 \times w_{gdz}$, Length > 2 000 m Specific value for drilled BFZs
Orientation distribution	Fisher
Mean pole	Orthogonal to core plane
Fisher concentration, κ	20
Power-law size exponent, k_r	2.8
Power-law size location, r_0	0.2 m
Minimum radius away from drillholes, $r_{min\text{-}ss}$	7 m
Minimum radius at drillholes, $r_{min\text{-}dh}$	1 m

Table 2-2. Calibrated intensity decay constants $\lambda = c_\lambda \times w_{gdz}$ for specific BFZ intersected by drilling. This table is reproduced from Hartley et al. (2018).

BFZ	c_λ	BFZ	c_λ	BFZ	c_λ
BFZ005	0.15	BFZ099	0.25	BFZ216	0.15
BFZ012	0.15	BFZ100	0.05	BFZ230	0.2
BFZ020a	0.2	BFZ121	0.5	BFZ265	0.1
BFZ020b	0.2	BFZ122	0.5	BFZ284	0.4
BFZ021	0.2	BFZ130b	0.2	BFZ297	0.6
BFZ024	0.3	BFZ135	0.1	BFZ300	0.15
BFZ028	0.1	BFZ146	0.2	BFZ306	0.01
BFZ036	0.3	BFZ147	0.5	BFZ311	0.3
BFZ039	0.3	BFZ149	0.5	BFZ321	1.2
BFZ045	0.2	BFZ150	0.5	BFZ324	0.5
BFZ046	0.1	BFZ152	0.2	BFZ328	0.3
BFZ055	0.4	BFZ156	0.01	BFZ329	0.6
BFZ063	0.05	BFZ159	0.5	BFZ330	0.4
BFZ069	0.5	BFZ169	0.5	BFZ343	0.05
BFZ070	0.5	BFZ170	0.5	BFZ346a	0.5
BFZ084	0.2	BFZ175	0.4	BFZ346b	0.5

This study considers a methodology for deriving the effective flow and transport properties for each fault zone on the mid-plane of the core volume, using an approach of upscaling to an equivalent porous continuous medium (see Chapter 3) followed by projection of these properties onto the midplane (see Chapter 4). These upscaled and plane projected BFZ provide an equivalent, simplified representation of the fault zone useful for both modelling convenience and for presentation. However, the important point to note here is that the property description is derived from conceptualisation of the fault zones as explicit DFN models of individual fractures as supported by integrated interpretation of structural and hydraulic data. This contrasts with the previous Olkiluoto DFN (Hartley et al. 2012), which used a direct interpolation/extrapolation of measured properties between drillhole intersects, which are typically few for individual fault zones.

2.2.3 Illustrations

Figure 2-4 through Figure 2-6 illustrate one realisation of the fault-related fractures on a horizontal slice through part of the model around the base of the ONKALO. These figures are reproduced from Hartley et al. (2018). Figure 2-4 shows the modelled deterministic mid-planes (black) about which stochastic fault-related fractures are generated, as well as the modelled damage zone extents (grey), noting that some BFZ such as BFZ020b and BFZ160 are gently dipping and so their thickness is exaggerated. The true thicknesses vary, and in the absence of drillhole data, scales with size (see Table 2-1), as seen when comparing the long sub-vertical BFZ045 with shorter BFZ063 and BFZ046. Figure 2-5 shows the resulting swarms of fractures around these mid-planes, generated according to a BFZ specific intensity and thickness. It can be seen that where a zone is either thick (e.g. BFZ020b and BFZ160) or has a high intensity (e.g. BFZ045), then the swarms are well connected, whilst for thinner (e.g. BFZ046 and BFZ346a) or less intense zones (BFZ230 and BFZ265) fractures only connect over parts of the fault area. Hence, the modelling of fault-specific width and intensity has a strong influence on the potential hydraulic importance of each fault zone.

Finally, Figure 2-6 superimposes the fault zone-related fractures on the same background network as shown in Figure 2-1 to complete the illustration of the structural DFN model. It is seen that several of the fault zones significantly enhance connectivity of the network along near planar channels, while others only offer a localised enhancement of connectivity.

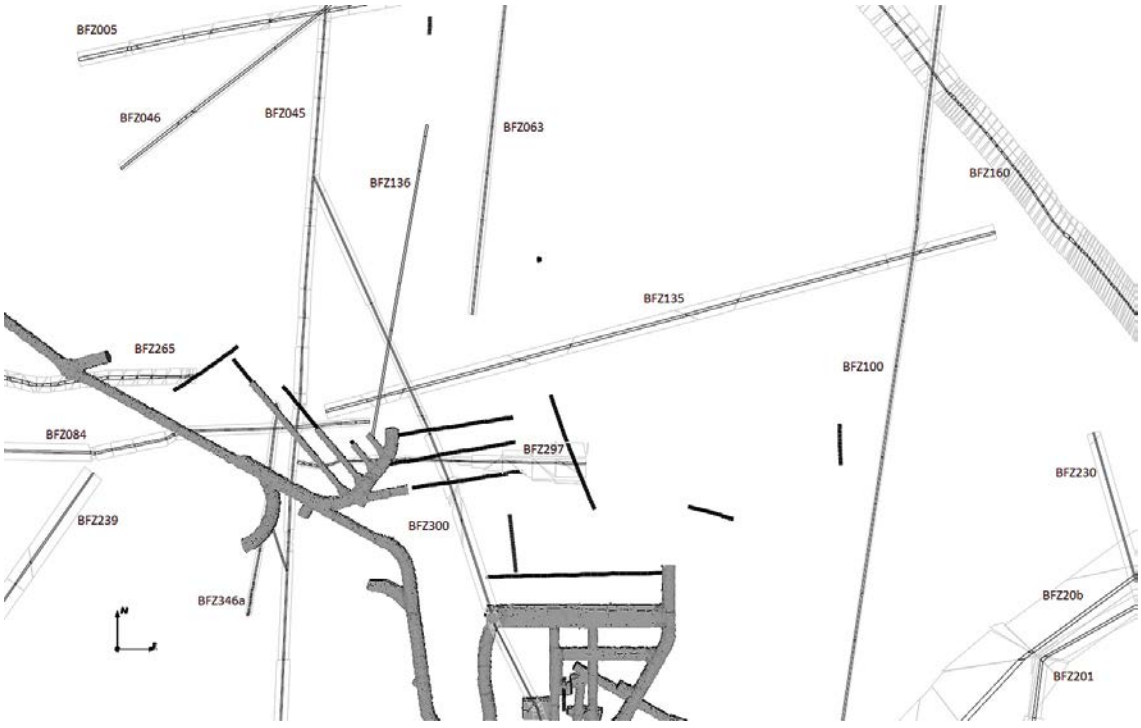

Figure 2-4. *A slice at z = –420 m through the fault zones around the base of the ONKALO shown on a scale of 800 m E-W. The black lines show the fault mid-planes with the damage zone shown by the surrounding grey volume. This figure is reproduced from Hartley et al. (2018).*

Figure 2-5. *A slice at z = –420 m through the fault associated fractures (brown) around the base of the ONKALO shown on a scale of 800 m E-W. No sealed parts of the fractures are removed at this stage. This figure is reproduced from Hartley et al. (2018).*

Figure 2-6. *A slice at z = –420 m through the combined DFN model for fault associated fractures (brown) and the background fractures in the rock mass (see Figure 2-1). The slice is shown local to the base of the ONKALO on a scale of 800 m E-W. This figure is reproduced from Hartley et al. (2018).*

2.3 Hydraulic conceptualisations

2.3.1 Spatial distribution of openings

A cornerstone of integrating the geological and hydrogeological description of fractures is to establish how much of the fracture surface area contains openings/voids and how these openings might be distributed spatially. The geological records from core characterisation provide only limited means to put bounds on how many fractures are open versus closed. However, the following was identified by Hartley et al. (2018) to provide an estimate of the proportion of open fracture area:

- When combining fracture logs with high resolution resistivity measurements from PFL logging, the proportion of electrically conductive (and hence potentially open) fractures was estimated to be between ~50 % to ~70 % near surface, decreasing to ~25 % to ~40 % at depth. Splitting the analysis into inside and outside the damage zones of faults, the portion of open surface area might be up to 10 % higher inside fault zones compared to outside.
- Based on mechanical arguments, fracture apertures are likely to scale with fracture size (see Hartley et al. (2018), Section 4.1 therein). In addition, the fault zones (akin to the largest fractures) include both a higher proportion of electrically-conductive fractures as well as the majority of the highest flows observed. Therefore it is asserted that the portion of open fracture area will typically correlate with fracture size.

Based on the above, a functional form for the portion of open fracture area is proposed based on the size, r, and depth of the fracture, $\omega(r, z)$. Flow will occur in these openings provided the open part of the fracture connects with openings in other intersecting fractures to form inter-connected channels through the fracture system. Clearly, as ω decreases, the connectivity of openings will diminish and flow will be restricted to fewer and fewer connected open channels. Therefore, this is a key parameter in constraining the spatial distribution and magnitudes of flow.

In addition to the proportion of fracture area open to flow, a conceptual model is required for distributing this area spatially across the fracture. This is difficult to quantify remotely within the rock on useful scales of tens-hundreds of metres. The simplest model is to take $\omega(r, z)$ as the probability that all of a particular fracture is open, and then just sample from a uniform distribution to provide a realisation of the open part of the system. However, as rocks in the crust are typically in compression, it is unphysical to suppose that a large fracture could remain open over its entire area. It is more reasonable to assume that parts of a fracture surface will be asperities (i.e. with both sides in mechanical contact) or sealed by minerals or gouge, as observed in direct measurements of laboratory samples of natural fractures (e.g. Brown and Scholz 1985). These regions of the fracture surface are closed to flow, causing the flow through the fracture to become channelised, as has been confirmed by field experiments (e.g. Abelin et al. 1994) and numerical studies (e.g. Glover et al. 1998).

A simple model of such a situation, bridging this geological description with a practical large-scale DFN modelling approach, is to assign individual openings a characteristic length, L_h, such that fractures smaller than this size can be considered either open or closed according to the probability $\omega(r, z)$, and all larger fractures are made up of patches that are either open or closed according to the same probability $\omega(r, z)$. In this way, the distribution of openings on fractures larger than L_h becomes a heterogeneous chequerboard. An illustration of this for a few large fractures of c 500 m length is shown in Figure 2-7 where $\omega(280, -420) \sim 0.5$ and $L_h = 20$ m, and the openings are generated by a pure nugget process. Clearly, flow through a distribution of openings such as this becomes channelised and is attracted toward fracture intersections since they offer additional connections either into neighbouring fractures or through by-passing asperities.

Initial prototyping of this concept for channelised flow was developed in the previous iteration of DFN modelling at Olkiluoto (Hartley et al. 2012), as a model variant denoted Case C. There, the modelling choice was made to set L_h to 20 m as this allowed the concept to be feasibly implemented in a site-scale model; a smaller length would have generated a total number of fractures larger than could be practically solved over in a DFN flow simulation. In support of this choice, drillhole data indicates that 20 m coincides with the approximate spacing of water conducting fractures at depth (spacing can be taken as $1/P_{10,corr}$, which is c. 17 m for $T > 10^{-10}$ m^2/s WCF, or c. 30 m for $T > 10^{-9}$ m^2/s).

Based on the above, an L_h of 20 m is deemed an appropriate hypothesis for representing the channelisation of flow in ODFN 3.0.

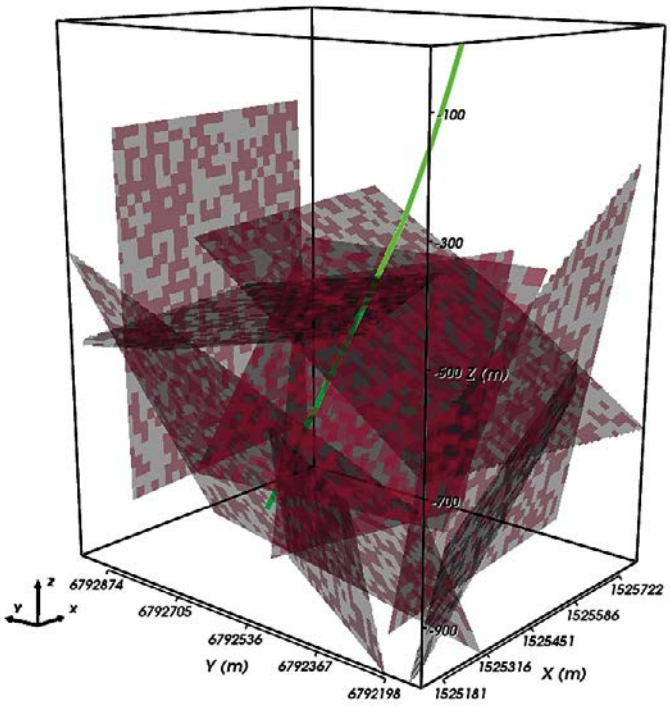

Figure 2-7. *Example of a DFN model where a random portion of fracture area is open to flow for a rock volume local to drillhole OL-KR1 (green line). Only the large fractures are shown here (i.e. 564 m > r > 284 m). The sealed area is coloured grey, the open area is red; with about 50 % of the fracture area open for these large fractures. This figure is reproduced from Hartley et al. (2012).*

The functional form for the open fracture area, $\omega(r, z)$ is a key parameter for calibrating the modelled frequency of flow to measurements due to the significant effect the proportion of individual fracture area open to flows has on the hydraulic connectivity of the fracture network. The final parameterisation of $\omega(r, z)$ is selected (Hartley et al. 2018) to ensure the frequency of simulated water conducting fractures is consistent with measured flows. The absolute value and depth trend in $\omega(r, z)$ needs to be adjusted to get the correct frequency for each elevation region, while its dependence on size provides one control (along with the underlying distributions of fracture size and aperture) of the shape of simulated transmissivity distribution and the difference between flow frequency inside and outside fault zones.

Figure 2-8 provides an illustration of the fracture area open to flow for a section of the ODFN 3.0 model local to the base of the ONKALO. Many blue segments can be seen along the traces of long fractures as a result of the chequerboard distribution of openings. The lower figure demonstrates how sparsely connected the open part of the network becomes after removal of sealed parts of the fractures. A 3D illustration of the distribution of openings on the largest stochastic fractures, $r > 80$ m, is shown in Figure 2-9. This illustrates that although some open channels are evident across whole fractures, generally connections only occur through the formation of channelised flow paths via the addition of open patches on intersecting fractures.

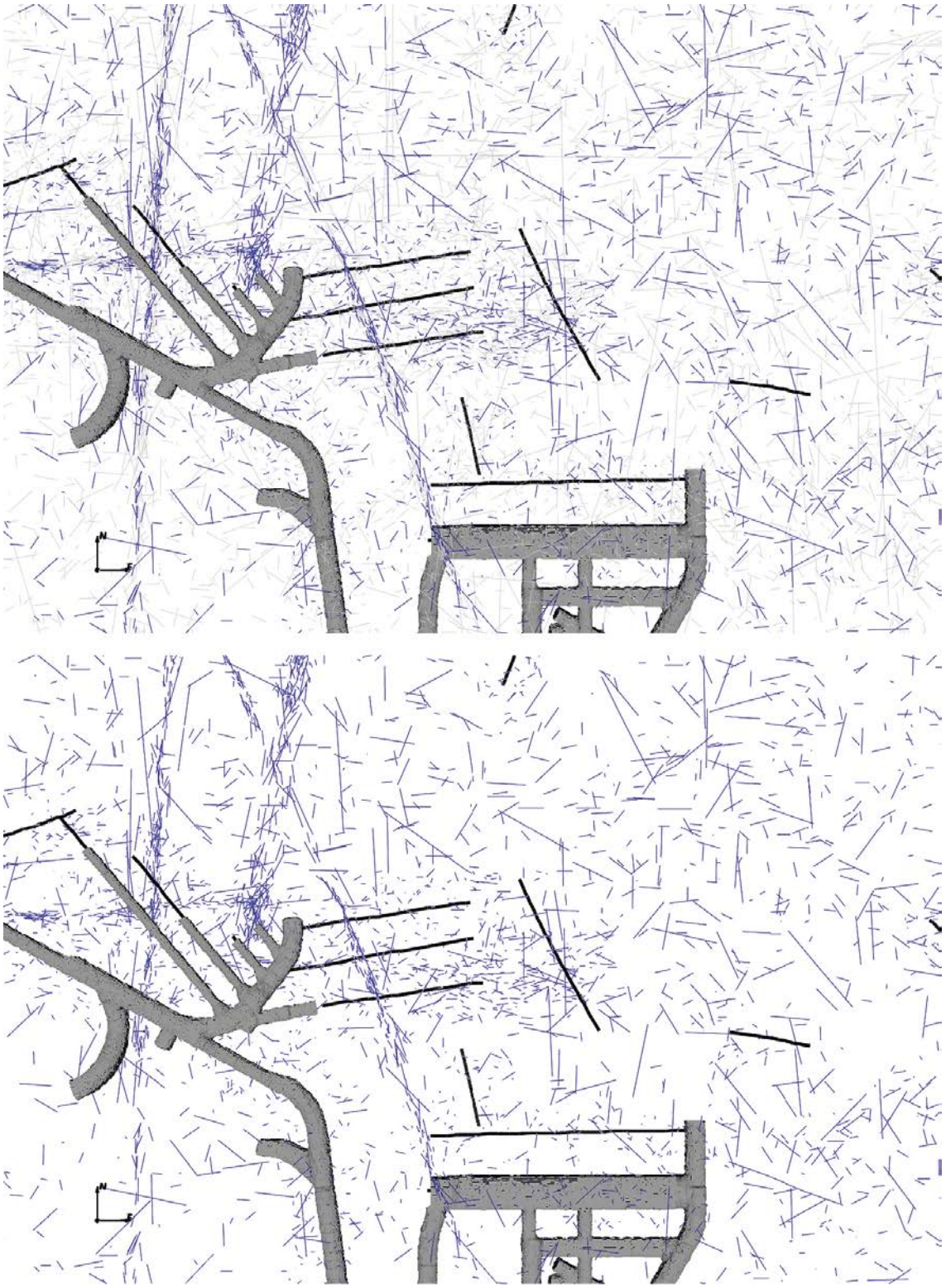

Figure 2-8. *Slice through all fractures at –420 m around base of ONKALO on a scale c 450 m E-W. Top: Fractures are coloured by hydraulic openness: blue-open, grey-closed; Bottom: only open fractures are shown. Here, ω(r, –420) varies from 0.25 to 0.45 with Log10(r), and L_h = 20 m. This figure is reproduced from Hartley et al. (2018).*

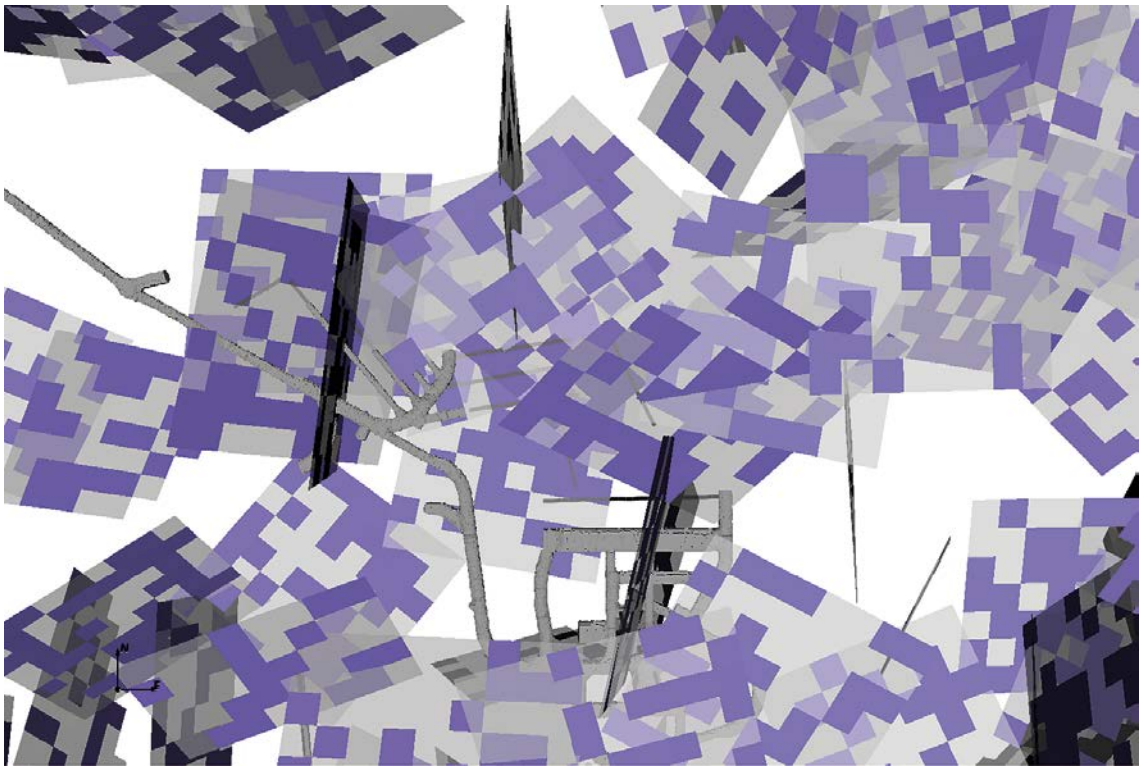

Figure 2-9. *3D view of the largest stochastic fractures around the base of ONKALO on a scale c. 900 m E-W with fractures coloured by hydraulic openness: blue-open, grey-closed. This figure is reproduced from Hartley et al. (2018).*

2.3.2 Aperture distribution and hydromechanics

Analysis in Hartley et al. (2017) identified a power law relationship ($e = aL^b$) between fracture aperture (e) and size (L) as appropriate for the initial aperture distribution (prior to modification by stress and the application of certain geological criteria – see below). The authors of that report set the coefficient, a, to be 1.12×10^{-5} m and interpreted a possible range for the exponent, b, of between 0.3 and 0.7; in the hydraulic modelling performed, the central value of 0.5 was used. Based on this parameterisation, the starting point for calibration by Hartley et al. (2017) used the following formulation of initial aperture, $e_{h,0}$ prior to coupling to stress:

$$Log(e_{h,0}) = \mathrm{Log}(1.12 \cdot 10^{-5}) + 0.5Log(L) + 0.3N(0,1) \quad (2\text{-}1)$$

where L is the length of a whole fracture before removal of sealed parts. Some additional randomness about the size trend is allowed for in the last term, i.e. a semi-correlation between hydraulic aperture and size.

Following the initial assignment of hydraulic aperture for each fracture according to size, the hydromechanical hyperbolic fracture law model of Willis-Richards et al. (1996) is used to include the effects of normal closure on fracture aperture:

$$e_h = e_r + \left(\frac{e_{h,0}}{1 + \frac{9\sigma'_n}{B}} \right) \quad (2\text{-}2)$$

where e_h is the hydraulic aperture after stress modification, e_r is the residual aperture at closure, $e_{h,0}$ is the initial aperture (see (2-1)), σ'_n is the effective normal stress on the fracture (total normal stress minus pore pressure) and B is the 90 % closure stress. The final term in (2-2) therefore represents the closure or dilation of the fracture according to changes in normal stress. The normal stress observed at any given fracture can vary as a function of space (as the *in situ* stress field components can vary throughout the rock volume), of the fracture orientation (with respect to the *in situ* stress field components) and of time (with changes in stress occurring throughout the glacial cycle due to the presence/absence of an ice sheet).

Calibration of the model by Hartley et al. (2018) determined the residual aperture, e_r to be 10^{-6} m, and the 90 % closure stress, B to be 65 MPa, in order to agree with the observed trends in flow magnitudes with fracture orientation and depth, when coupling aperture to a site-scale stress field derived from stress measurements. This stress field is described by the "Mean" values given in Table 4-19 of Hartley et al. (2018); it is separated into three tiers by two major zones (BFZ020 and BFZ099), with the magnitude of each stress component generally increasing with depth due to the increasing mass of the overlying rock.

The same aperture-stress formulation was used for both background fractures and fault related fractures, with the exception that the initial aperture $e_{h,0}$ was:

- Increased by a factor of 3 for fractures in the damage zones of six BFZ: BFZ020a/b, BFZ19a/c, BFZ021 and BFZ146 based on the observation by Hartley et al. (2018) that these appear to have distinctly higher transmissivities.
- Increased by a factor 2.2 if $\sigma_n < (\sigma_2 + \sigma_3)/2$ for 80 % of large fractures ($r > 11.2$ m) or fault zone related fractures, reducing to 40 % for small fractures ($r \leq 1$ m) in the rock mass. This is based on high flows typically associated with fractures with low normal stress for a subset of fractures that are smooth or semi-rough. The analysis of Hartley et al. (2018) could not identify geological or spatial constraints on smooth and semi-rough fractures, but the ONKALO did reveal their prevalence in fractures of longer trace. Therefore this is applied stochastically to enhance a subset of fractures at low normal stress based on J_r/size fracture statistics from the systematic mapping data.

An illustration of the resulting transmissivity distribution is shown in Figure 2-10 on a horizontal slice at –420 m around the ONKALO. Several trends can be perceived: transmissivities of small fractures (c 1–10 m) are low around 10^{-10} m^2/s, while larger (c. 50–200 m) background fractures are up to around 10^{-7} m^2/s; E-W aligned fractures (parallel to maximum principal stress) tend to have higher transmissivity than similar sized N-S fractures; and transmissivity is significantly higher, around 10^{-6} m^2/s, in BFZ020a/b.

The trend of reducing transmissivity with depth is illustrated in Figure 2-11 on a vertical slice through the site-scale model. This demonstrates where the intensity of sub-horizontal fractures is increased in ER1 near the surface, while the network is more sparsely connected below this. It is also shown that sub-horizontal fractures tend to have higher transmissivity than sub-vertical ones. Most individual fractures within BFZ have similar transmissivity to the background, but are evident as swarms of more connected systems, with the exception of BFZ020a/b and BFZ019a/c that are clearly more transmissive.

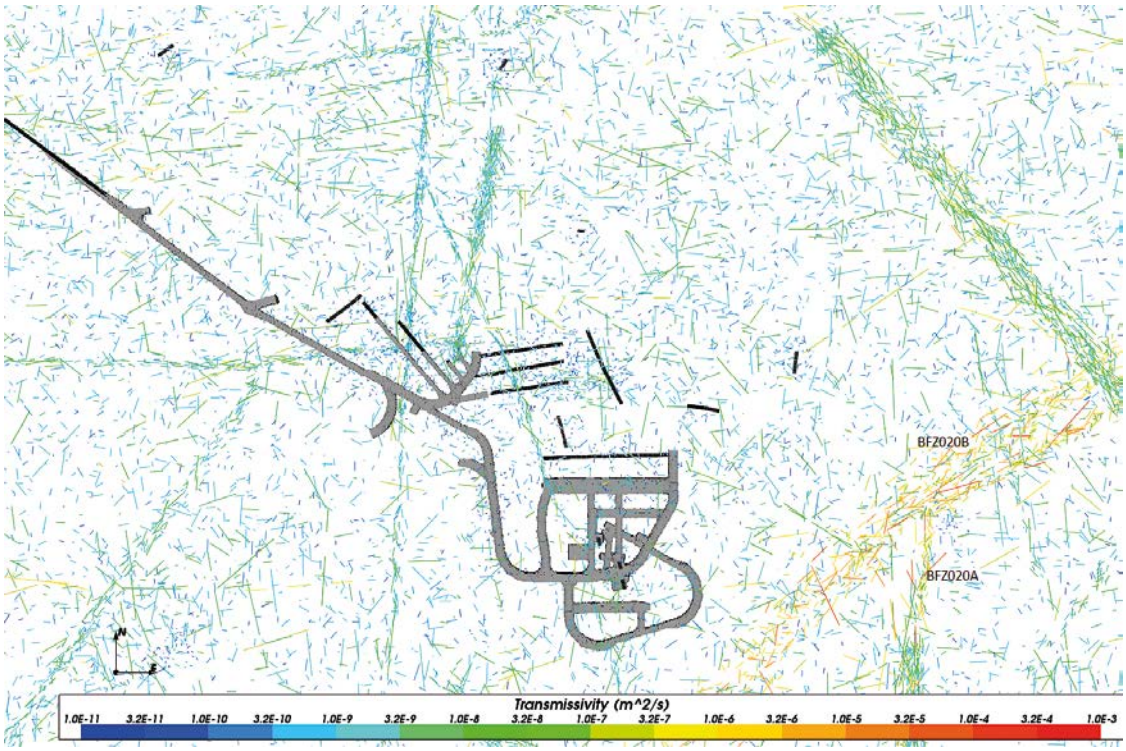

Figure 2-10. *Horizontal slice through part of the ODFN 3.0 model around the base of the ONKALO at –420 m shown on a scale of about 1 000 m E-W. Fractures are coloured by transmissivity after application of aperture-stress coupling. This figure is reproduced from Hartley et al. (2018).*

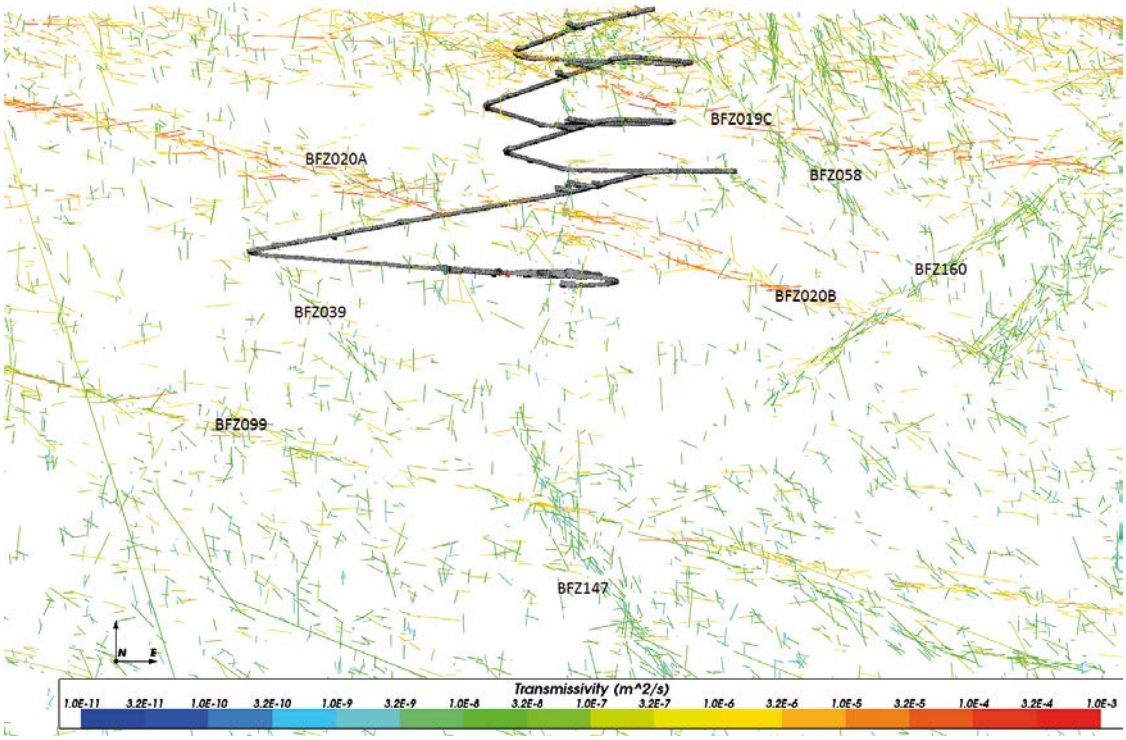

Figure 2-11. *Vertical slice through part of the ODFN 3.0 model shown on a scale of about 1 900 m E-W and 1 200 m vertical. Fractures are coloured by transmissivity after application of aperture-stress coupling. This figure is reproduced from Hartley et al. (2018).*

3 ECPM upscaling of flow and transport properties

The site-scale ODFN 3.0 model developed in Hartley et al. (2018) and summarised in Chapter 2 can be used to understand flow and transport at Olkiluoto. Specifically, it can be used to carry out flow-related transport calculations, based on the conceptual representation of the bedrock, to determine likely flow-paths to the surface. It is expected that such a representation of flow and transport through a network of sparsely distributed discrete flow conduits reproduces many characteristics of the real system, albeit through a simplified and stochastic approach. However, the discrete nature of the approach has implications for flow and transport, such as the lack of communication between adjacent fractures via the intervening rock matrix. Although such compartmentalisation of flow is an observed feature of the hydraulic system at Olkiluoto (Posiva 2012) and the rock matrix is of low hydraulic conductivity, it can still be sufficient to provide some limited connectivity over very short distances, for example between the repository and a high-conductivity BFZ, with implications for safety. For such conceptual reasons, and for practical reasons (i.e. a reduction in computational cost for large models), it can be valid to consider alternative model approaches, and in particular the commonly used continuous porous medium approach.

In this case, flow and transport properties of the DFN model of the Olkiluoto bedrock are represented using an equivalent continuous porous medium (ECPM) model. The ECPM model can be used by itself, for example for palaeohydrological evolution or as part of a combined model with discrete fracture network models representing the area around the repository, with the ECPM model used for parts further away. The ECPM model is obtained by upscaling the properties of the fracture network onto a grid with variable block size: $(10\ \text{m})^3$ in the central well characterised area so as to capture the locally enhanced resolution of geological sub-models, and $(30\ \text{m})^3$ further from the centre of the island. Upscaling is done grid element by grid element, calculating the hydraulic conductivity, kinematic porosity and flow wetted surface area per unit volume for each element.

In this chapter, an alternative approach for upscaling the DFN models is presented, determining geocellular transport properties (travel time and flow-related transport resistance) and their statistics, and using these to derive ECPM properties for the ODFN 3.0 model. This flow-based transport upscaling method (see Subsection 3.2.2) is compared to existing geometric-based techniques (defined in Subsection 3.2.1) through comparison of the upscaled properties. Transport pathways through a DFN representation of the bedrock and the two ECPM models considered are also presented.

3.1 Flux-based upscaling methodology

In ConnectFlow (Wood 2016a), a flux-based upscaling method is currently implemented that requires several flow calculations through a DFN model to be performed in different directions (Jackson et al. 2000) and verified in (Wood 2016b). The approach first subdivides the DFN model into a number of submodels, defined by the grid cells; for each of these submodels, flow calculations are performed for a linear hydraulic gradient in each of the 3 axial directions. The hydraulic conductivity tensor, K, is subsequently evaluated for each submodel to provide a best fit to the DFN flux responses.

Figure 3-1 shows an illustration of how flow is calculated in a DFN model (a 2D network is shown for simplicity). To calculate equivalent hydraulic conductivity for the grid cell shown, the flux through the network is calculated for a linear head gradient in each of the axial directions. Due to the variety of connections across the network, several flow-paths are possible, and may result in cross-flows non-parallel to the head gradient. Cross-flows are a common characteristic of DFN models and can be approximated in an ECPM by an anisotropic hydraulic conductivity tensor.

One refinement of the upscaling methodology is to simulate flow through a slightly larger domain than the grid cell required for the ECPM properties, but then calculate the flux responses through the original grid cell. The reason for this is to avoid over-prediction of hydraulic conductivity from flows through fractures that just cut the corner of the grid cell but that are unrepresentative of flows through the in-situ fracture network (Figure 3-2). This problem is most significant in sparse heterogeneous networks in which the flux through the network of fractures is affected by “bottlenecks” through low transmissivity fractures and is quite different to the flux through single fractures. The enlarged domain used is known as a “guard-zone”; an appropriate choice for its thickness is approximately one fracture equivalent radius (about half the fracture side length).

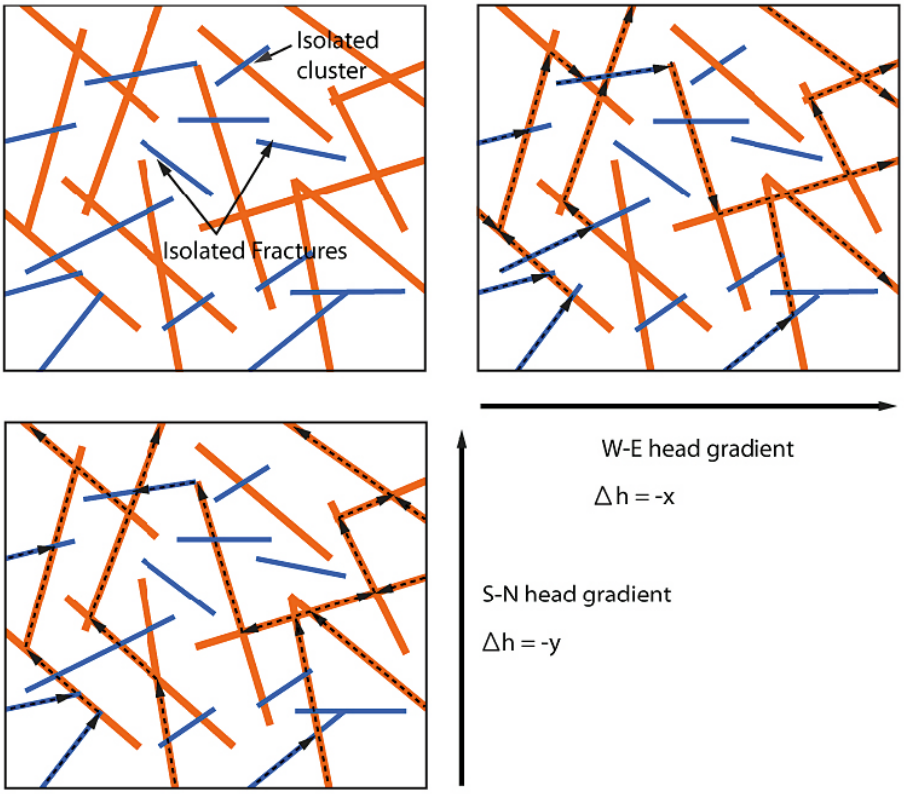

Figure 3-1. *2D illustration of flow through a network of fractures. A random network of fractures with variable length and transmissivity is shown top left (orange fractures have high transmissivities, blue have low). Top right: flow-paths (dotted arrows) for a linear head gradient E-W decreasing along the x-axis. Bottom left: flow-paths through the network for a linear head gradient S-N decreasing along the y-axis.*

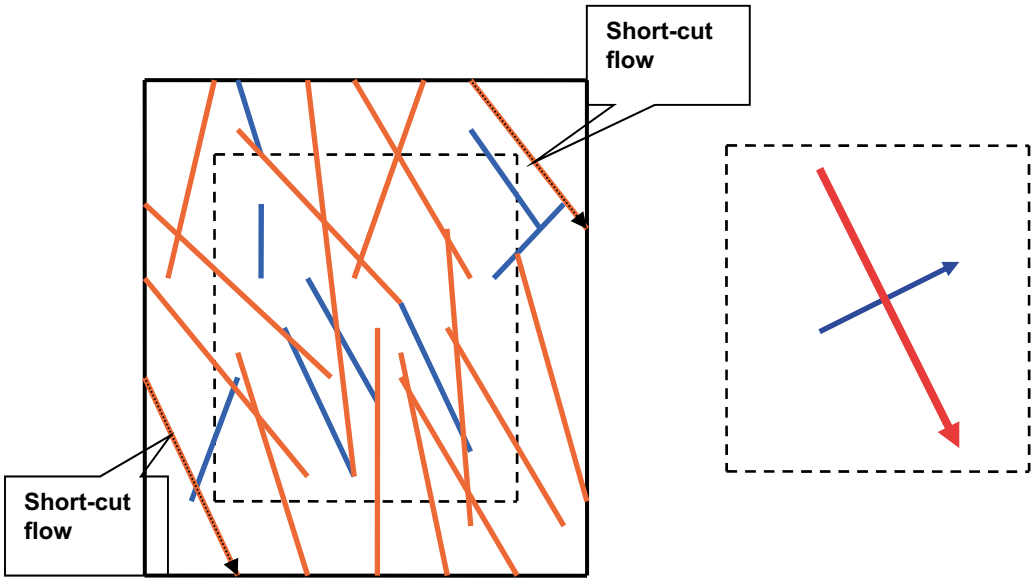

Figure 3-2. *2D illustration of how hydraulic conductivity calculated on the grid cell can be overestimated.*

3.2 Transport-based upscaling methodology

3.2.1 Geometric-based transport upscaling

Within ConnectFlow (Wood 2016a), the current approach for calculating the equivalent kinematic porosity is to sum the fracture area times transport aperture for each connected fracture within the grid cell. The fracture surface area is calculated as the sum of the fracture area in the grid cell. The transport properties are therefore just simple geometric approximations that do not reflect effects of heterogeneity, channelling or hydraulic gradient.

3.2.2 Flow-based transport upscaling

Instead of the geometric approach currently adopted, an alternative methodology for calculating equivalent kinematic porosity and fracture surface area is proposed. For each of the grid cells, the 3 axial flow calculations are first performed to extract a hydraulic conductivity tensor, K, (see Section 3.1) with the computed flow fields subsequently used to perform particle tracking in each of the 3 axial directions from the upstream face (releasing particles according to a flux weighting). Based on these particle tracking simulations, distributions of travel times, tortuosity and flow-related transport resistance for each direction and each grid cell are evaluated. An example of the transport legs (defined as particles tracked between fracture intersections) from which the pathways are built for the three axial flow calculations performed is shown in Figure 3-3. Though the three figures look similar, they have different transport legs (although many of the transport legs can carry flow in more than one of the axial flow cases).

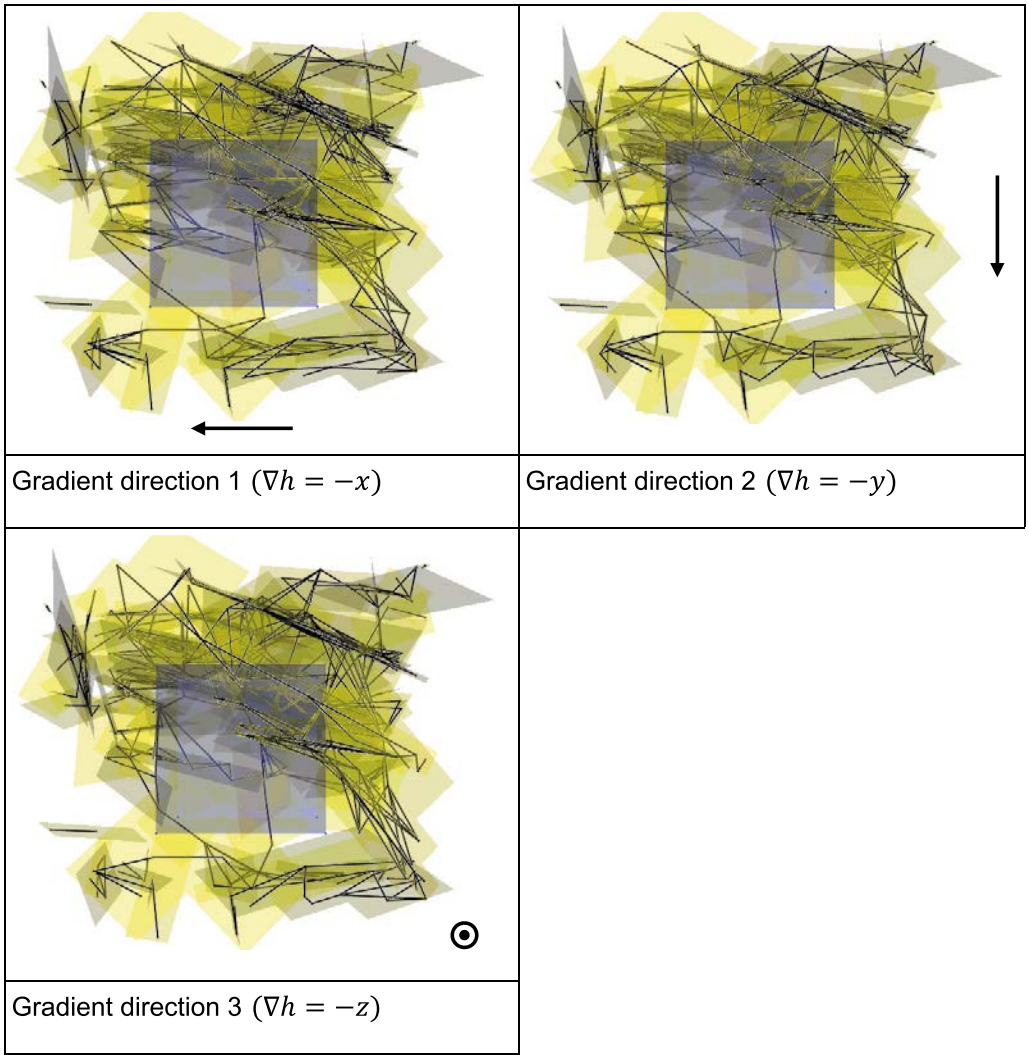

Figure 3-3. *Transport legs used to determine flow-related transport properties for three directions of the applied pressure gradient.*

The particle tracks generated for each of the three axial flow calculations performed consider the release of a number of particles for each possible start point on the upstream face of the model. The number of particles is proportional to the number of possible start points, typically 100 times the number of start points, and the particles are released based on a flux weighting approach. Only the part of the pathway inside the grid cell are used in the estimates below, the transport legs in the guard zone or outside the grid cell are excluded.

The pathway information can be used to estimate transport properties in a number of ways. Two approaches considered are:

1. To use the median pathway for the relevant transport property, this is the default approach.
2. To use a large fraction of the pathways (excluding some fraction of extreme paths at both ends of the distribution) and calculating the transport properties from the ensemble average over the remaining paths. This approach is explored in Subsection 3.3.2.

The definition chosen in this report for the equivalent kinematic porosity in each direction, ϕi, is

$$\phi_i = \langle {t_{ij}}/{L_{ij}} \rangle_m \, {Q_i}/{A_i} \tag{3-1}$$

where Q_i is the total flow-rate out of the downstream face; A_i is the transverse cross-sectional area; and t_{ij} and L_{ij} are the travel time and projected length between the start and end of the path inside the grid cell for the applied pressure gradient (in direction *i)* for path *j*. The subscript *m* indicates that the value used is for the median of the distribution of *t/L*.

The total flow rate can also be written as

$$Q_i = A_i \, n_i \cdot K \cdot (\nabla h)_{\mathrm{i}} \tag{3-2}$$

where K is the fitted conductivity tensor; $(\nabla h)_{\mathrm{i}}$ the hydraulic gradient applied in the relevant axial direction; and n_i a unit vector in that axial direction. Therefore the equivalent kinematic porosity can be calculated as

$$\phi_i = \, n_i \cdot K \cdot (\nabla h)_{\mathrm{i}} \langle {t_{ij}}/{L_{ij}} \rangle_m \tag{3-3}$$

which is the equation used in ConnectFlow to calculate this property. Note that apart from the median (50 percentile), this estimate can be used for any other porosity percentiles as well, based on the travel time over projected length distribution. The estimate for kinematic porosity is anisotropic, reflecting anisotropy in the orientations, connectivity and transmissivity of the underlying DFN. This generality is beyond the functionality of most porous medium software. As a simplification, a geometric mean of the 3 directional components is calculated for each transport property. Some care needs to be taken since there may not be any pathways in particular directions due to the nature of the intersecting fractures. For such directions, ϕ_i is set to zero. The mean porosity is calculated as

$$\phi = \begin{cases} 0 \; if \; all \; \phi_i \; are \; zero \\ \left({1}/{3} \right) exp \left({\sum_{i:\, \phi_i \neq 0} \log \phi_i}/{\sum_{i:\, \phi_i \neq 0} 1} \right) \end{cases} \tag{3-4}$$

That is, first, the geometric average is taken over all directions for which a value is available; following this, the arithmetic average is taken of the resulting value with the other directions that have zero porosity.

Similarly, the equivalent flow wetted surface for each axial direction, a_{ri}, is estimated by

$$a_{r,i} = \langle {F_{ij}}/{L_{ij}} \rangle_m \, {Q_i}/{A_i} \tag{3-5}$$

where Fij is the transport resistance calculated in the DFN model for the relevant direction i and path j. The subscript m indicates that the median of this distribution is used. This can be rewritten as

$$a_{r,i} = \, n_i \cdot K \cdot (\nabla h)_{\mathrm{i}} \langle {F_{ij}}/{L_{ij}} \rangle_m \tag{3-6}$$

which is the equation used in ConnectFlow to calculate this property. The mean flow wetted surface is again calculated as

$$a_r = \begin{cases} 0 \; if \; all \; a_{r,i} \; are \; zero \\ \left(\sum_{i:\, \phi_i \neq 0} 1 \Big/ 3\right) exp\left(\sum_{i:\, a_{r,i} \neq 0} \log a_{r,i} \Big/ \sum_{i:\, a_{r,i} \neq 0} 1\right) \end{cases} \quad (3\text{-}7)$$

Another property of interest is the tortuosity of the path, $\tau = l/D$, where l is the particle travel distance through the network and D is the distance between the end points of the particle track.

In the element property files used by ConnectFlow, values are required for each element for porosity and flow wetted surface (or P_{32}). With the flow-based transport properties, a facility has been added to export percentiles for each of the directional properties calculated. If no pathways exist for a particular direction, missing values are recorded in the export.

3.3 Evaluation of transport-based upscaling

In this section, the transport-based upscaling methodology detailed in Section 3.2 is evaluated on a number of models related to the ODFN 3.0 model for Olkiluoto. A summary of the ODFN 3.0 model is detailed in Chapter 2 and contains:

1. Fractures within the bulk of the rock mass at Olkiluoto, with the minimum fracture size truncated at 7 m.
2. Similar fractures, but with a cut-off of 1 m near drillholes and repository structures.
3. Swarms of nearly parallel fractures representing the known fracture zones at Olkiluoto.
4. Stochastic brittle fracture zones represented as planar structures with properties derived from the known fault zones.
5. Lineaments represented as planar structures with properties derived from the known fault zones.

Although the full ODFN 3.0 model contains all of these, the models used for comparing geometrically upscaled properties with the flow-based ones in this section use a reduced version of the model which only incorporates fracturing in the rock mass (Points 1 and 2 above).

3.3.1 Dependence on cell size

In this subsection, a series of models with size 120 m cubed are considered, located with the bottom of the model at elevations –150 m, –390 m, –630 m and –810 m. Only fractures within the rock mass of Olkiluoto (i.e. excluding fault zones and lineaments) are considered. Grid cells of 10 m, 20 m and 30 m are used, resulting in models with 1 728, 216 and 64 grid cells respectively.

The dependence of model depth and grid cell size on the upscaled equivalent kinematic porosity are shown in Figure 3-4 for the transport-based upscaling method. With the smaller grid cell sizes better able to represent the inherent heterogeneity of the underlying DFN model, the results for cell size 10 m show the greatest variability in porosity. The median kinematic porosity also shows a dependence on the size of grid cell considered. Generally, the larger grid cells produce a lower median porosity, though at –150 m the median for the 10 m and 30 m cells are similar. The approach for the flow-based upscaling calculation using particle tracking in the network of fractures for each grid cell surrounded by a guard zone is shown explicitly in Figure 3-5 and Figure 3-6.

The next set of figures compare the flow-based and geometric porosity for a series of horizontal slices through the middle of the model (i.e. at an elevation 60 m above the bottom). In general, one would expect the flow-based porosity to be lower than the geometric porosity for the following reasons:

- In the geometric method equivalent kinematic porosity is calculated as the sum of the area times transport aperture of each connected fracture within the element. This includes any part of the fracture outside of the grid cell and although the fracture is trimmed to the grid cell, in general some corners of the fracture will still protrude.

- Whereas the geometric method considers the contribution to porosity for all fractures within the grid cell, the flow-based approach restricts the contribution to flowing fractures only. This effect will be increasingly prevalent as the grid cell size is increased.

This expectation is confirmed in a statistical sense, as shown in Figure 3-7. The median of the flow-based upscaled porosity is smaller than the geometric one for all models bar one (depth –630 m, cell size 10 m). One would also expect to observe this trend on a grid cell by grid cell basis. Horizontal slices through the models are shown in Figure 3-8 through Figure 3-11. Though for most cells the flow-based method has a lower porosity than the geometric one, there are cells for which this is not true. Although the reasons for this are not fully clear, the comparison of a scalar quantity (geometric porosity) with a value derived from a directional one (flow-based porosity) may not be a straight-forward one in all cases.

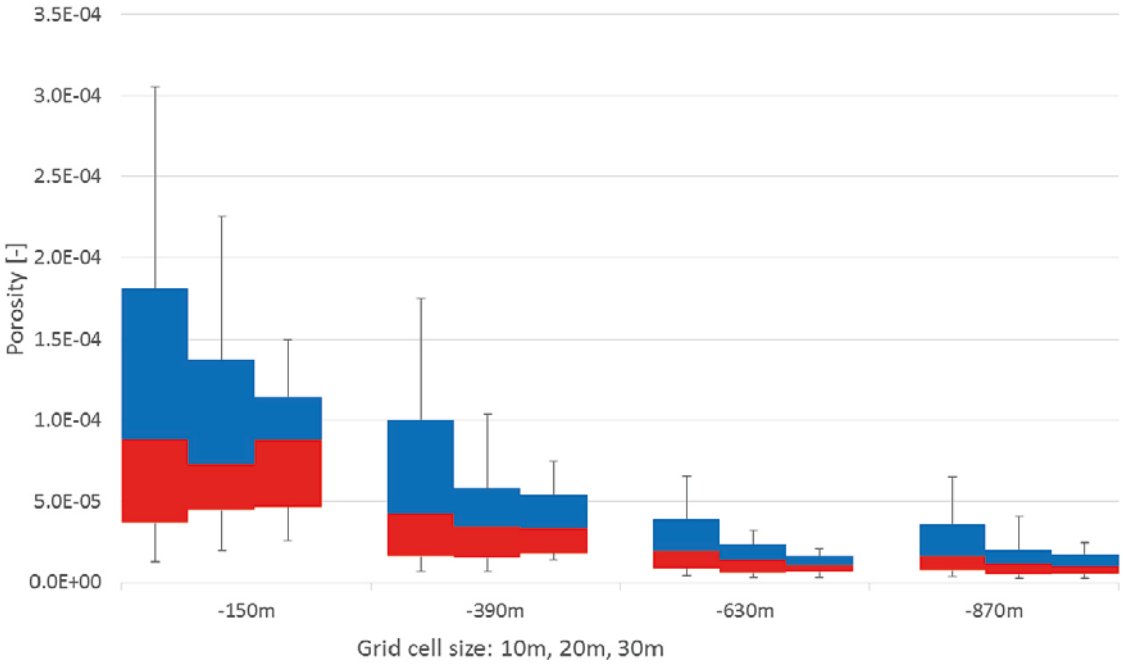

Figure 3-4. *Dependence of the flow-based porosity on depth and grid cell size. The boxes show the 25, 50 and 75 percentiles (red is 25 to 50; blue is 50 to 75). The whiskers show the 10 and 90 percentiles. For each depth, the plots are for 10 m, 20 m and 30 m grid cell size from left to right.*

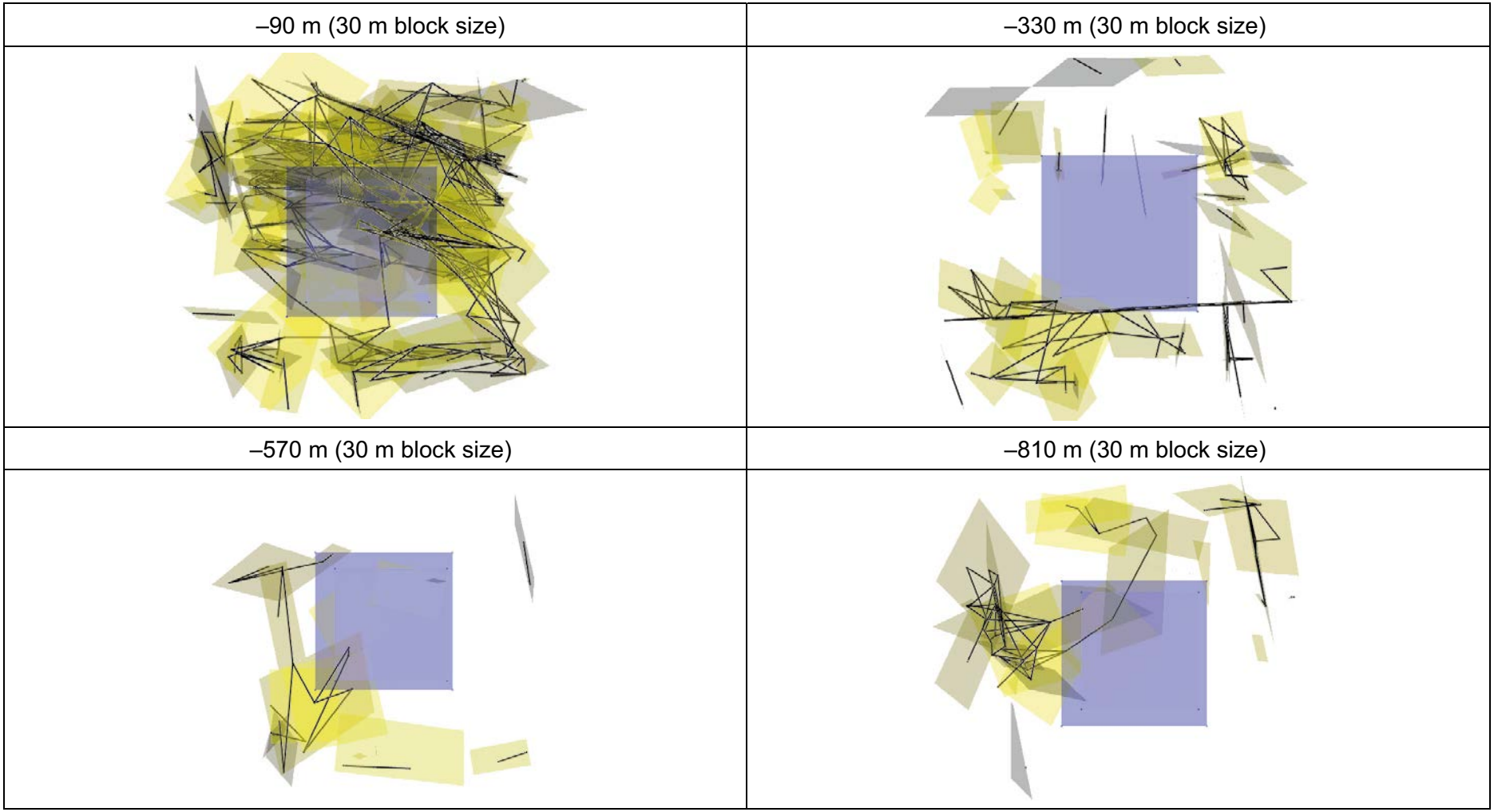

Figure 3-5. *Transport legs for cells near the centre of the various models for a block size of 30 m. The fracture intersecting the cell plus guard zone are coloured yellow and the cell itself blue.*

–90 m (30 m block size)	–90 m (10 m block size)
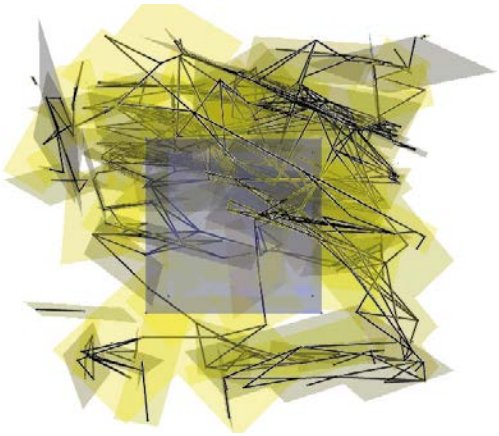	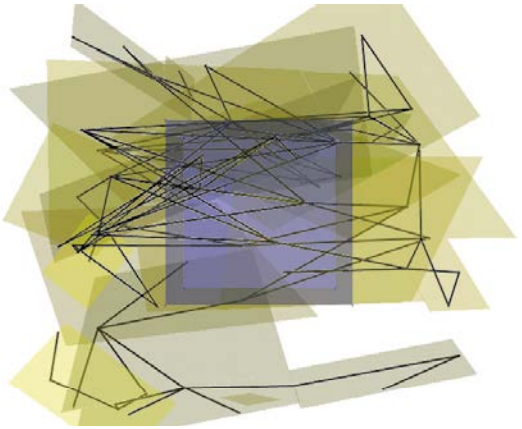
–330 m (30 m block size)	–330 m (10 m block size)
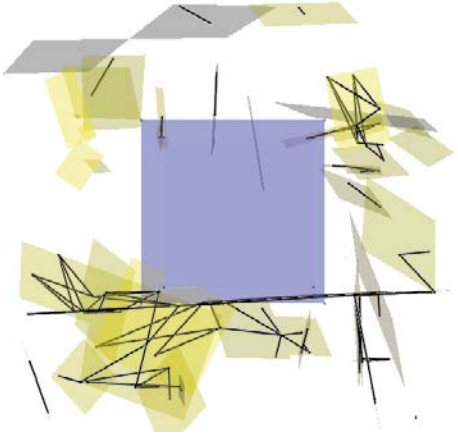	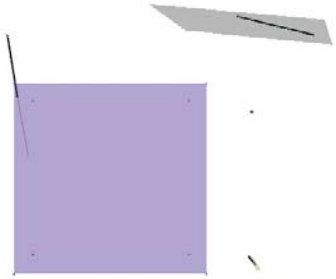

Figure 3-6. *Transport legs for cells near the centre of the various models for a block size of 10 m and 30 m. The fracture intersecting the cell plus guard zone are coloured yellow and the cell itself blue. Even at moderate depths for a smaller block size there will be blocks with very few, if any, pathways.*

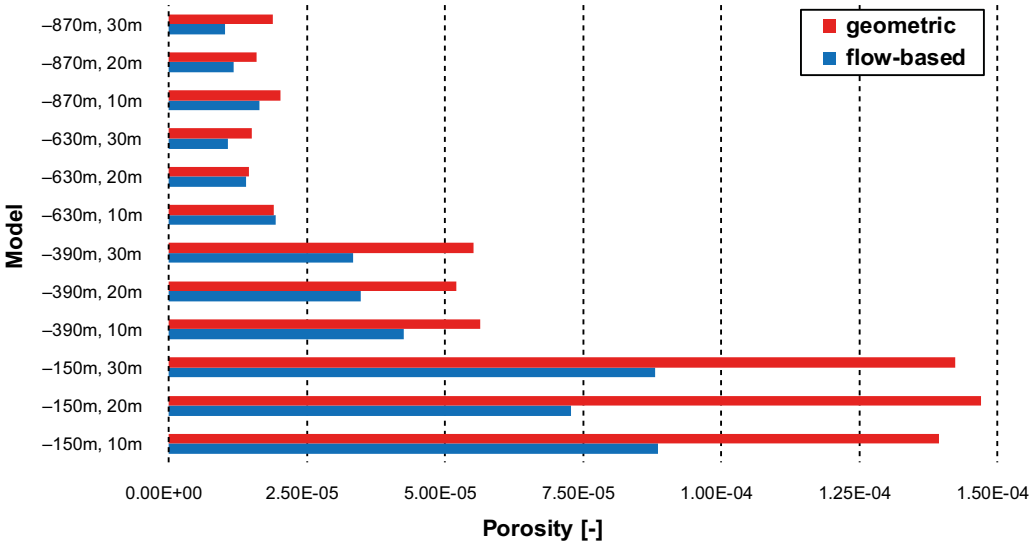

Figure 3-7. *Comparison of the median porosity between the geometric and flow-based method for upscaling DFN models as used in this section.*

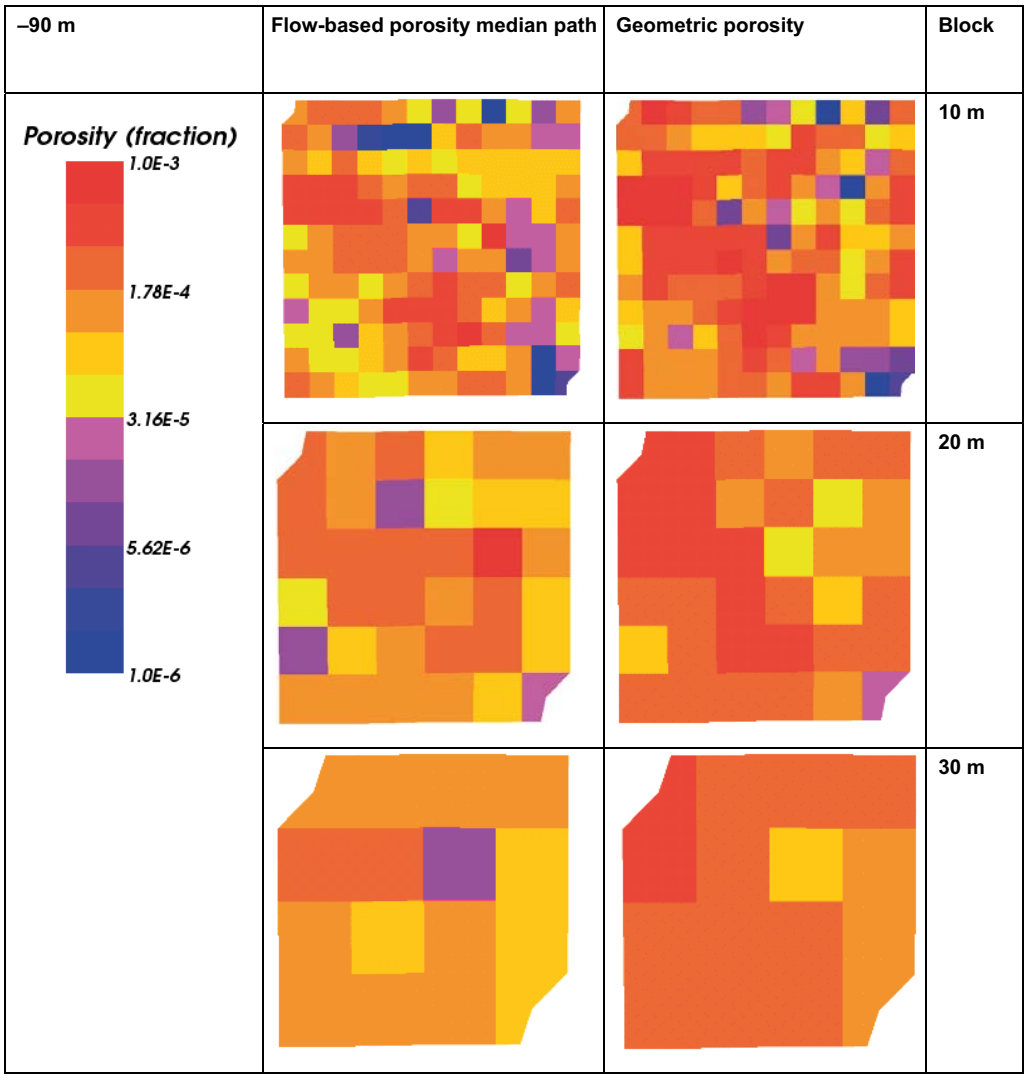

Figure 3-8. *Horizontal slices through the model with minimum elevation –150 m for porosity determined by the flow-based method and the geometric method for the three block sizes used. The slice is through the centre of the model at –90 m.*

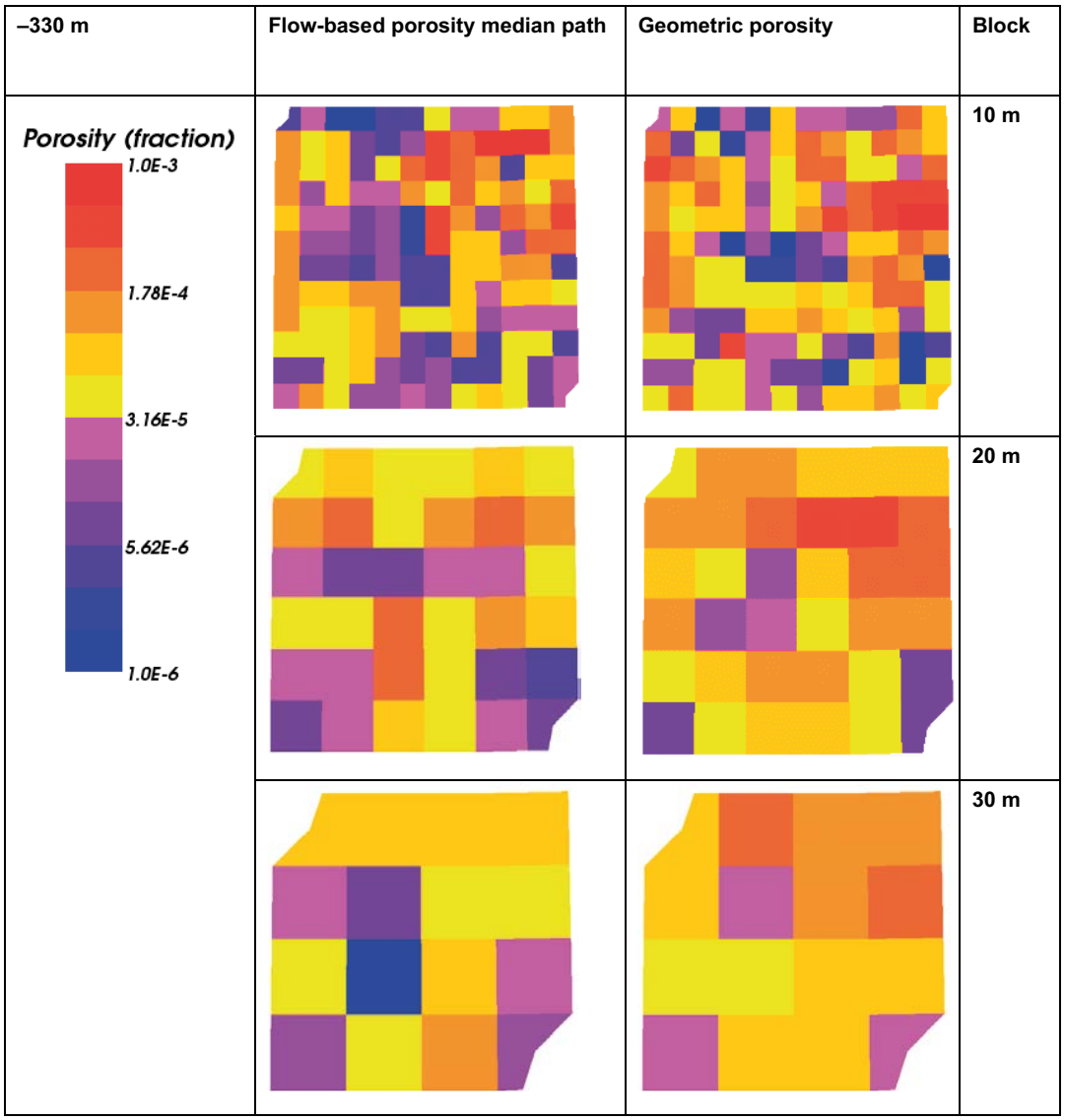

Figure 3-9. *Horizontal slices through the model with minimum elevation at –390 m for porosity determined by the flow-based method and the geometric method for the three block sizes used. The slice is through the centre of the model at –330 m.*

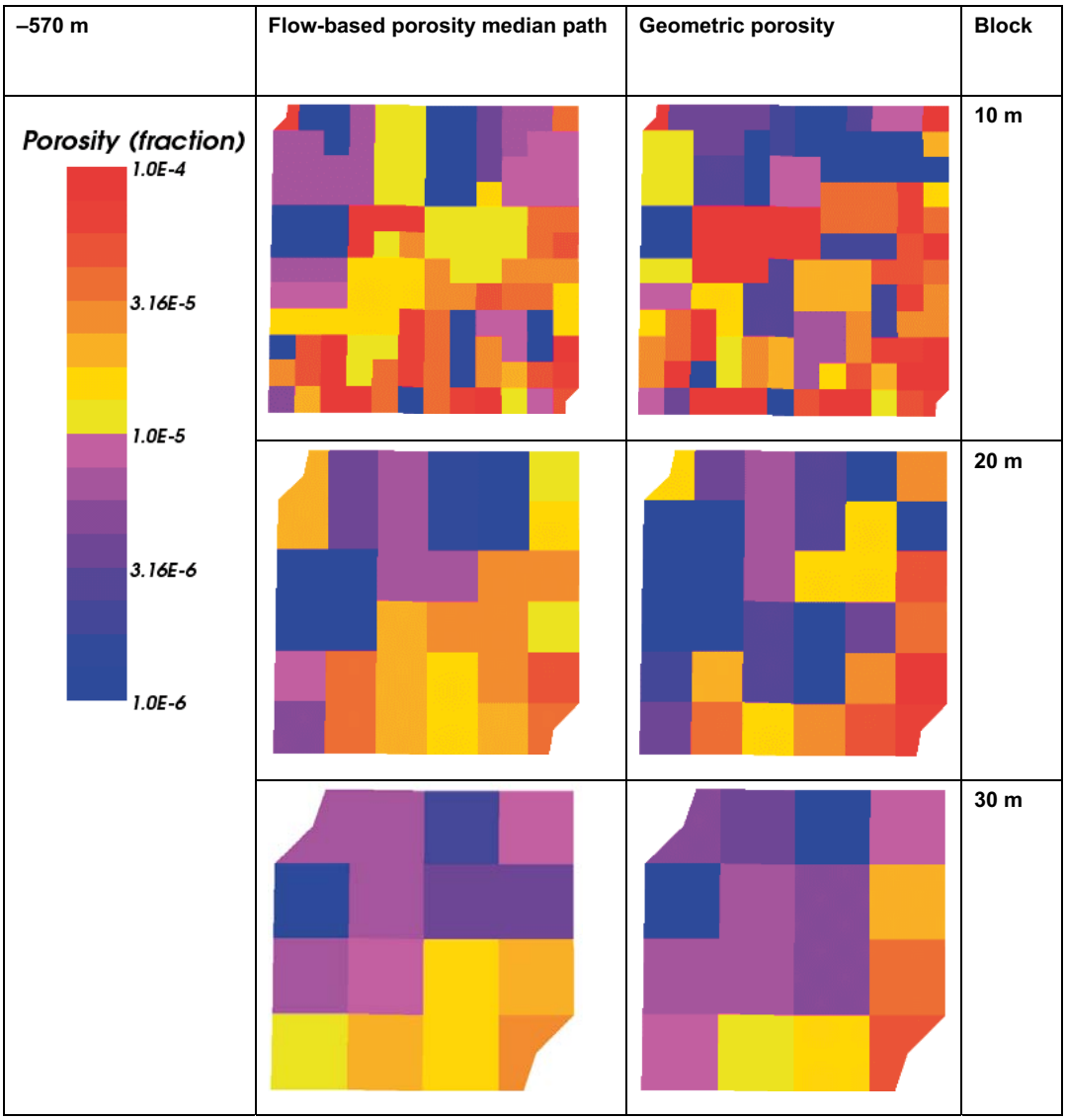

Figure 3-10. *Horizontal slices through the model with minimum elevation at –630 m for porosity determined by the flow-based method and the geometric method for the three block sizes used. The slice is through the centre of the model at –570 m.*

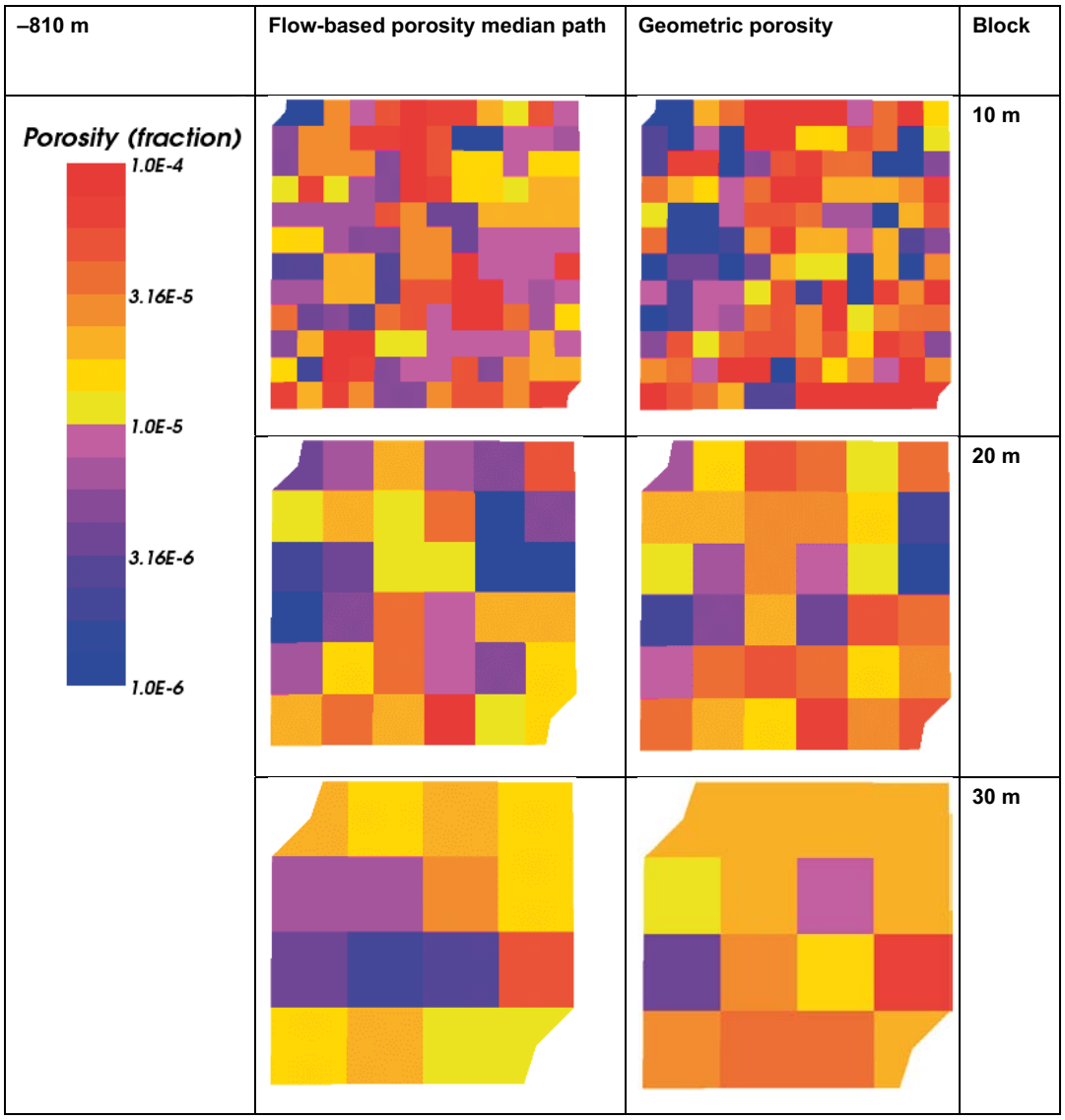

Figure 3-11. *Horizontal slices through the model with minimum elevation at –870 m for porosity determined by the flow-based method and the geometric method for the three block sizes used. The slice is through the centre of the model at –810 m.*

3.3.2 Dependence on depth and method

The model used in this section has an extent of 1 800 m × 1 800 m × 600 m, centred on the repository area. Only fractures within the rock mass of Olkiluoto (i.e. excluding fault zones and lineaments) are considered. The grid cell size is 30 m. The geometric upscaling method is compared to the flow-based method using both the median path (default) and "all flow paths", discarding 10 % of pathways (5 % at each end of the distribution of all flow paths) to avoid undue influence of outliers. There is not much difference between the two flow-based methods, although the one using the median path tends to give slightly lower porosity and total P_{32} (half the flow-wetted surface). Both give lower results on average than the geometric method. This is shown at a range of depths in Figure 3-12 for the porosity.

Figure 3-13 shows the distributions of porosity and total P_{32} over the whole model for the three upscaling methods considered. Again, there is little difference between the two flow-based methods, with the one using the median path giving slightly lower values. They both give lower values of porosity and total P_{32} than the geometric method.

Comparison on a grid cell by grid cell basis is made in Figure 3-14, showing two ratios for the porosity and total P_{32}. Most of the ratios of the flow-based method over the geometric method are below one (zero on the logarithmic scale), but there is a tail where the geometric method gives lower values for

a number of cells. This is true for both the porosity and total P_{32}. The ratio of properties for the two flow-based methods is very close to one, with the method using the median giving lower values for more cells than the one using all paths.

The same is shown graphically in Figure 3-15 with horizontal slices through the model showing the porosity at various depths. It is hard to spot any differences between the two flow-based methods (there are some near the centre at –50 m). Generally the flow-based methods have lower values at each depth, but the geometric method has more variability and has lower values for a number of cell.

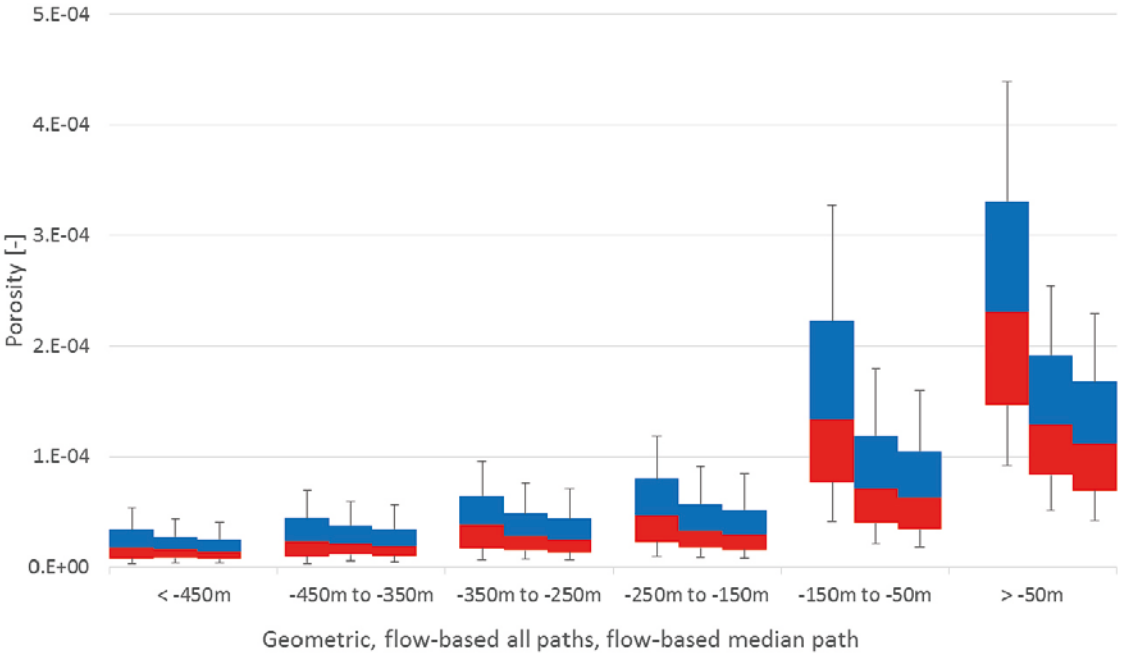

Figure 3-12. *Porosity by depth for the three methods. The boxes span the 25 to 75 percentiles (red is 25 to 50; blue is 50 to 75). The whiskers show the 10 and 90 percentiles. For each depth range, the plots from left to right are for the geometric, flow-based with all paths, and flow-based with median path upscaling methods.*

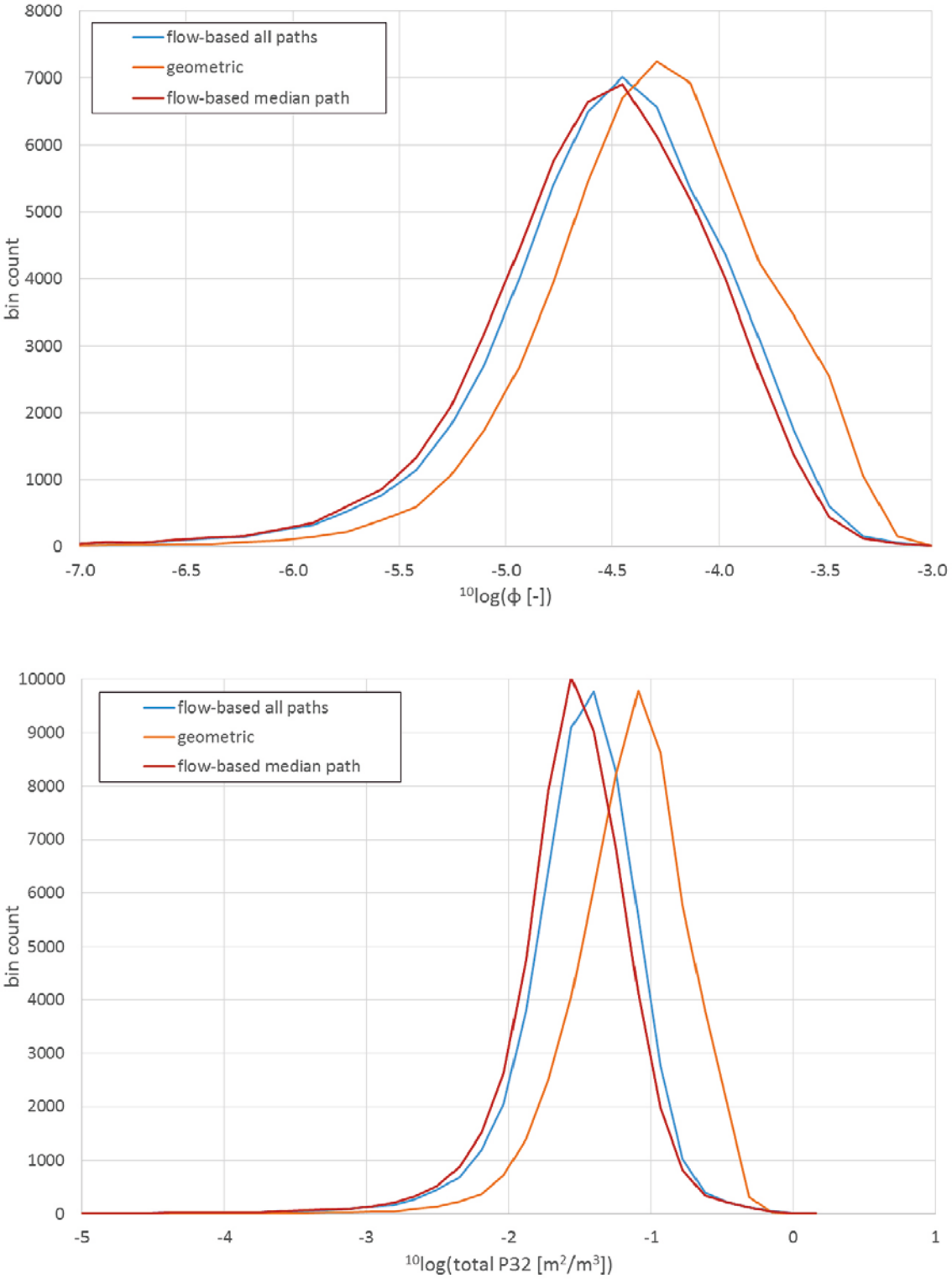

Figure 3-13. *Distribution of porosity (top) and total P32 (bottom) over the whole of the model for the three upscaling methods considered.*

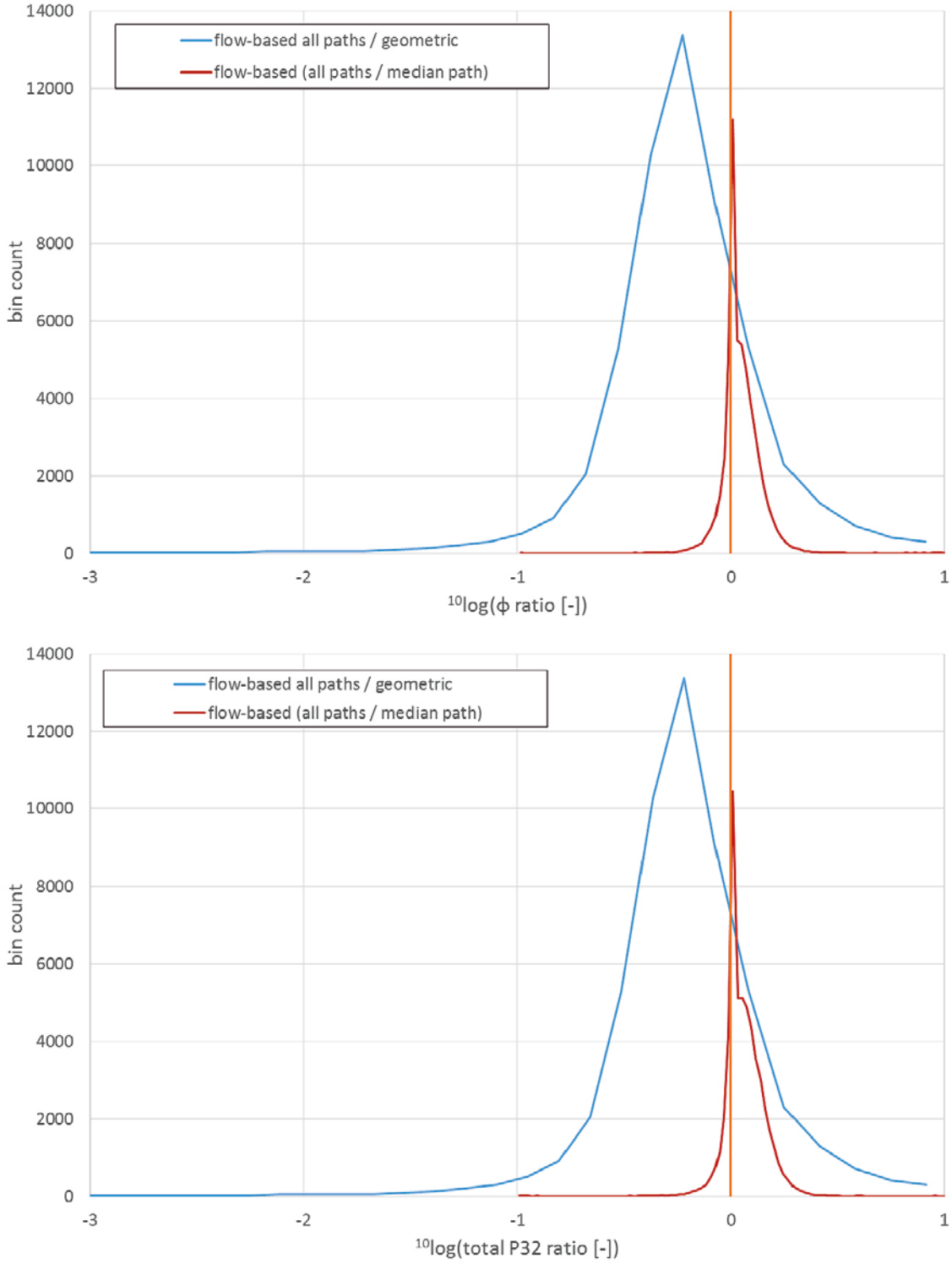

Figure 3-14. *Ratios of porosity (top) and total P32 (bottom) on a cell by cell basis for the three upscaling methods considered.*

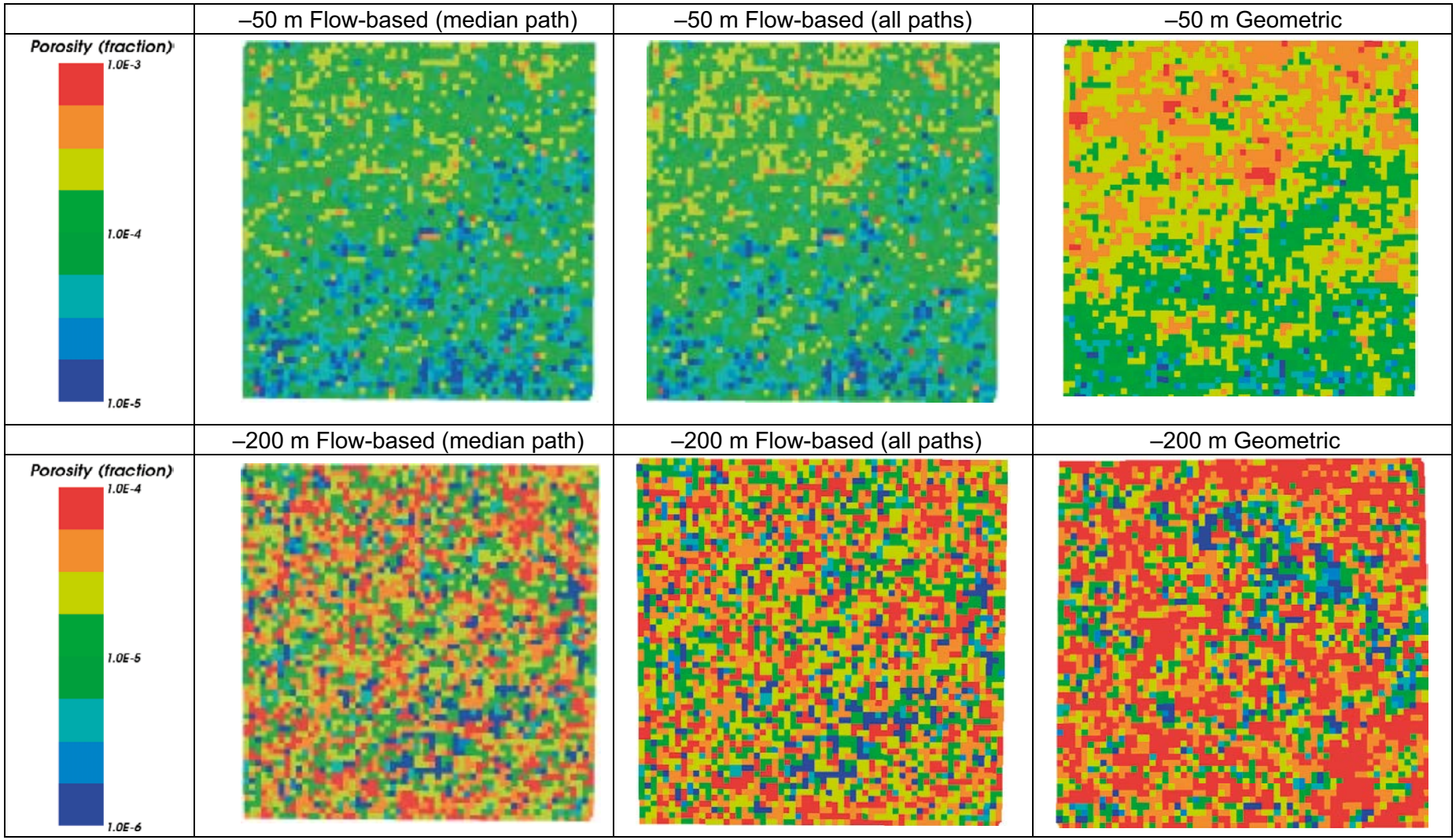

Figure 3-15. *Horizontal slices at various depths through the model showing the porosity determined by the three upscaling methods considered.*

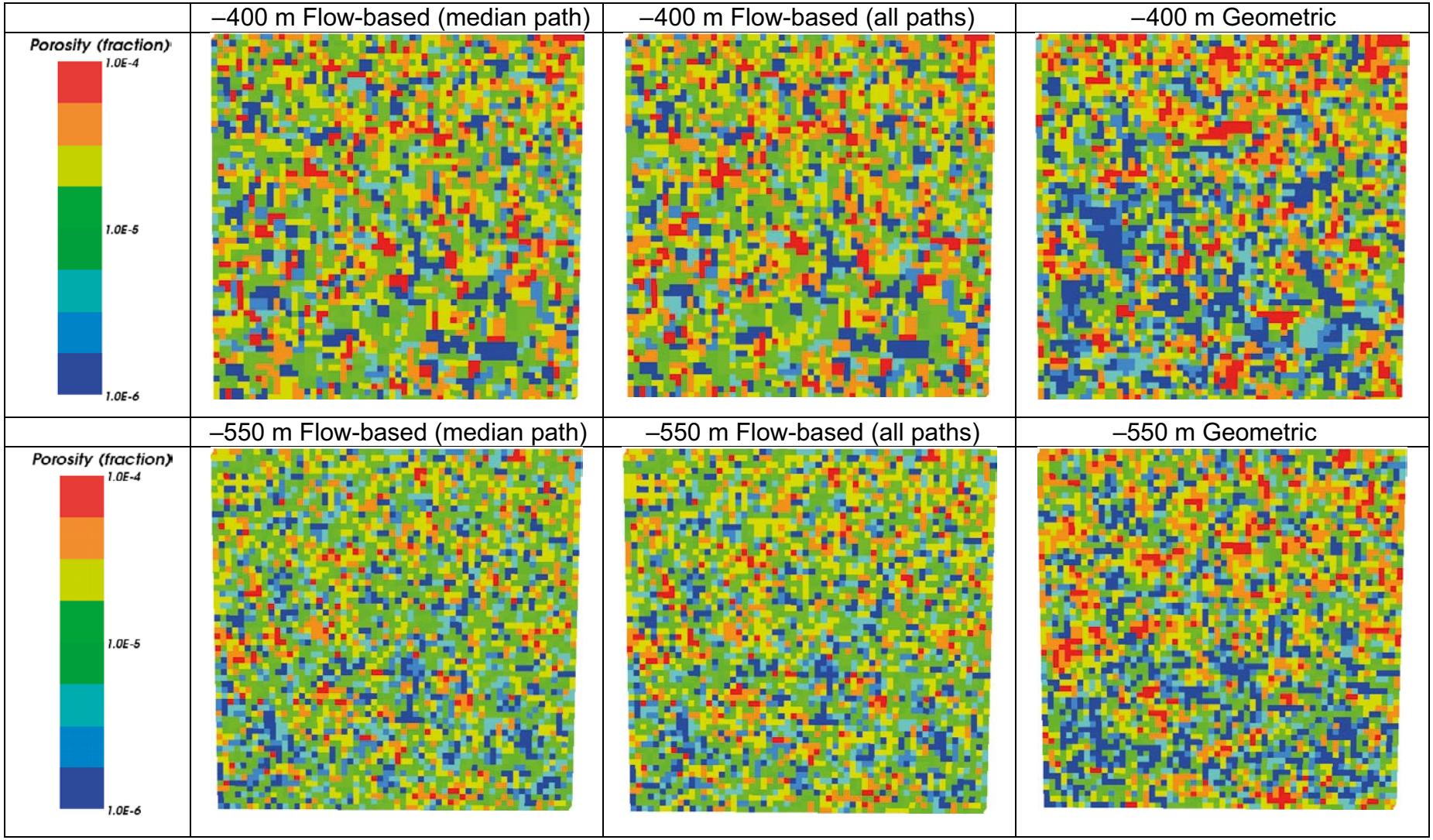

Figure 3-15 forts. *Horizontal slices at various depths through the model showing the porosity determined by the three upscaling methods considered.*

3.4 Example results for Olkiluoto

3.4.1 Comparison of kinematic porosities

Unlike the upscaled examples considered in Section 3.3, the DFN model used in this section is the complete ODFN 3.0 model, including fracturing in both the rock mass and fault zones of Olkiluoto (note that stochastic faults and lineaments are excluded).

Figure 3-16 and Figure 3-17 demonstrate the grid cell by grid cell ratios of the porosity and flow-wetted surface over the whole model. As for the results obtained for the test model used in Subsection 3.3.2, in most cases the flow-based method (using median path) gives lower porosities and P_{32} than the geometric method. However, for the full ODFN 3.0 model considered here, this effect is typically less pronounced than in the test cases performed in the previous section.

The central region around the repository uses a cell size of 10 m and the remainder a size of 30 m. This difference has a visual impact on the porosity distributions, as is clear from Figure 3-18, showing horizontal slices through the model at several depths. The other impact is that the variability is generally higher in the central region due to the smaller cells being better able to represent the inherent heterogeneity of the DFN. Nevertheless, the flow-based porosity appears more continuous around the edge of the central region where the grid cells change in size. Notably, at –250 m and –410 m the porosity determined by the geometric method is discontinuous around the edge of the central region. It would be worth investigating this further to determine the sensitivity of both upscaling methods to the cell size.

The conclusions are the same for the flow-wetted surface, which is shown at –410 m in Figure 3-19.

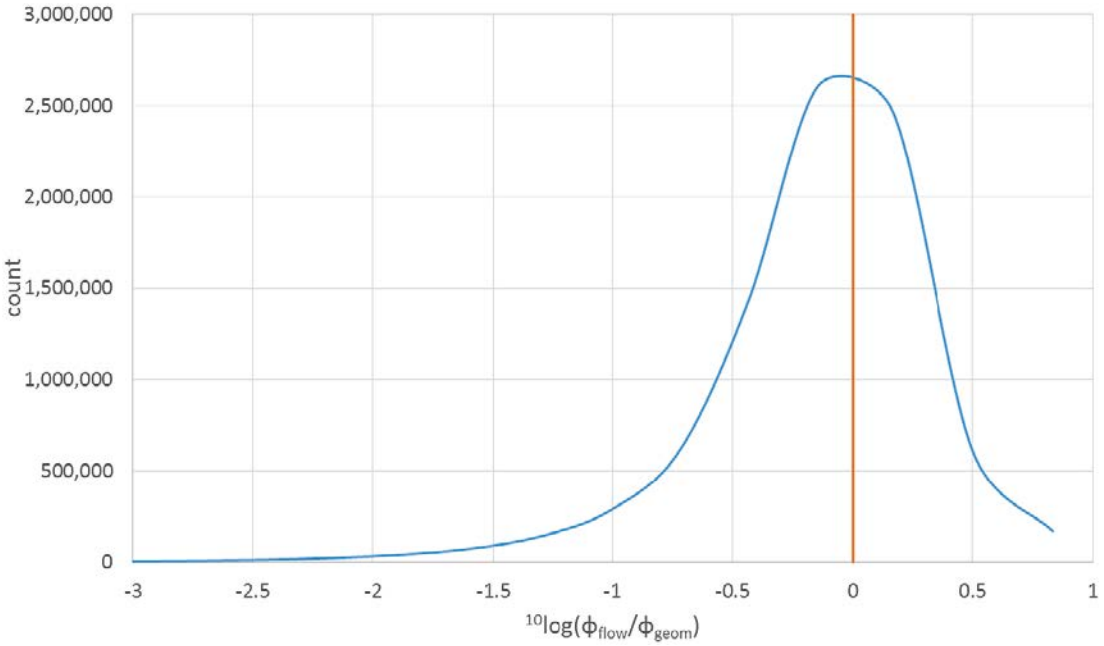

Figure 3-16. *Ratio of the porosity determined by the flow-based method (using median path) and that determined by the geometric method, over the entire ODFN 3.0 model.*

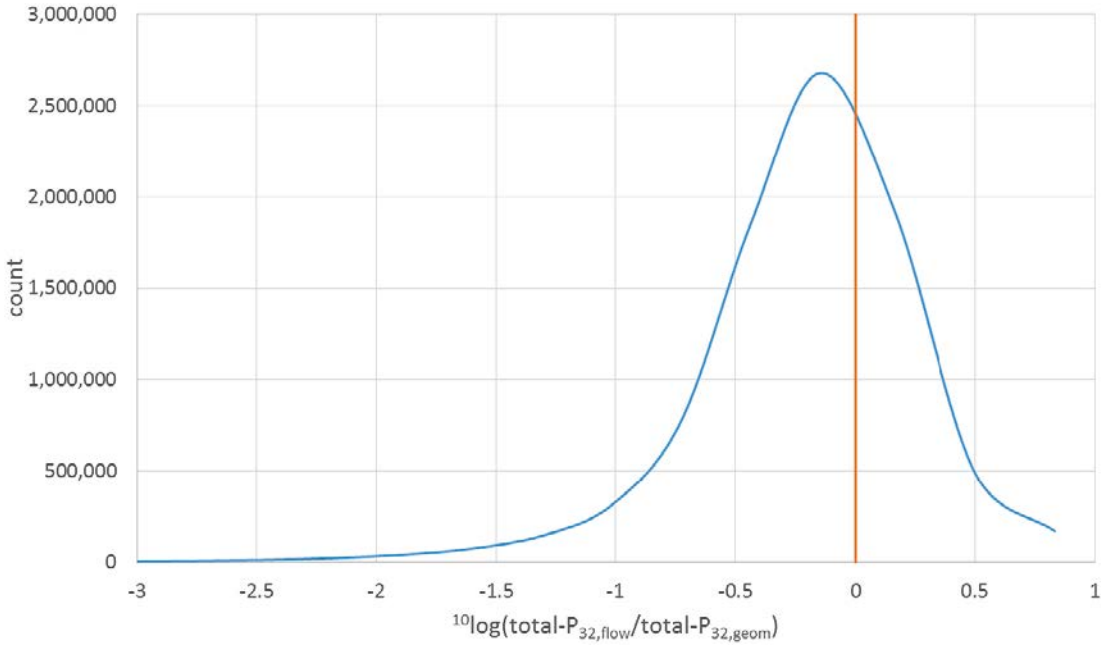

Figure 3-17. *Ratio of the total P32 determined by the flow-based method (using median path) and that determined by the geometric method, over the entire ODFN 3.0 model.*

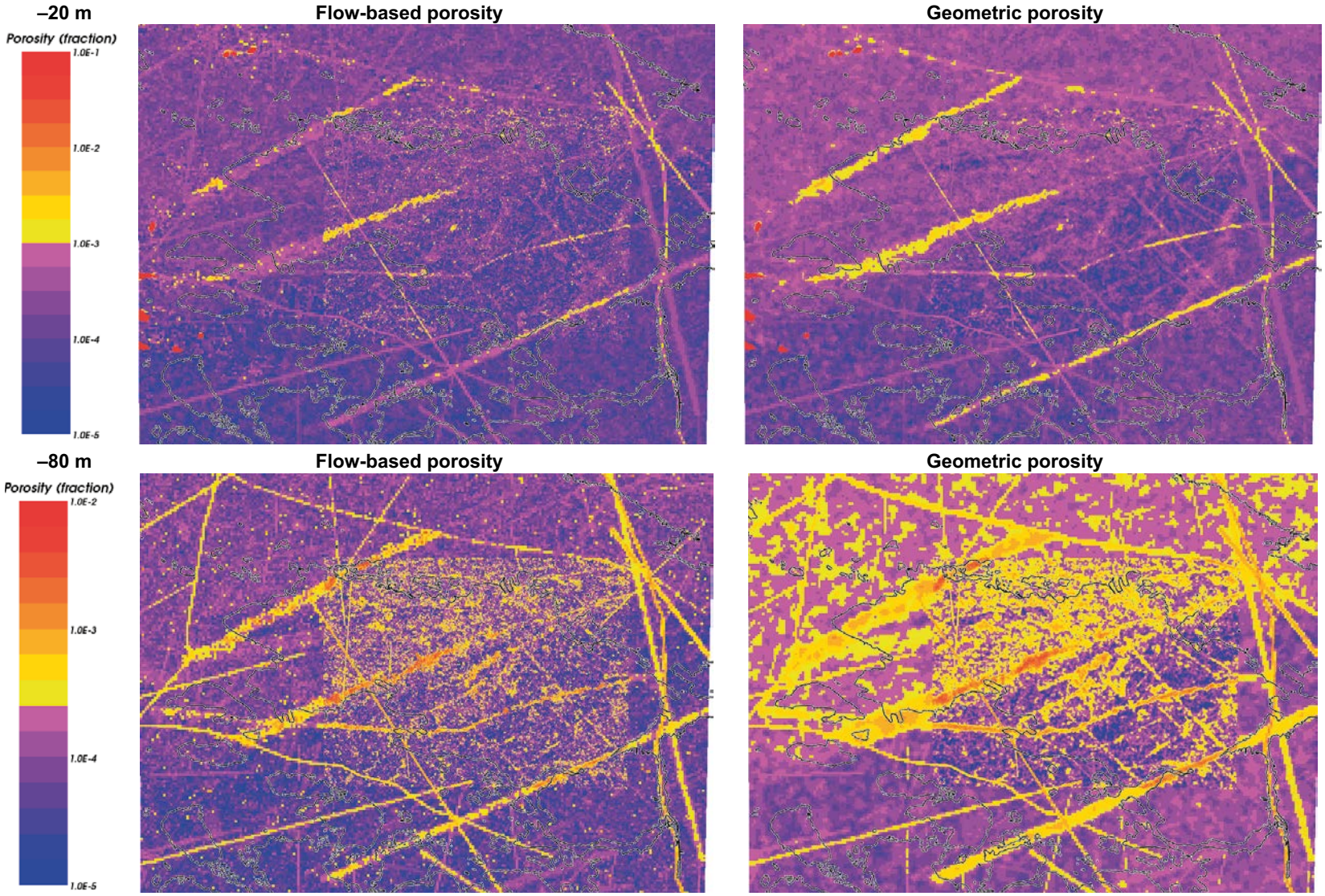

Figure 3-18. *Horizontal slices through the ODFN 3.0 model at various depths showing porosity. Note that the porosity range shown varies with depth to emphasize the differences between the two methods.*

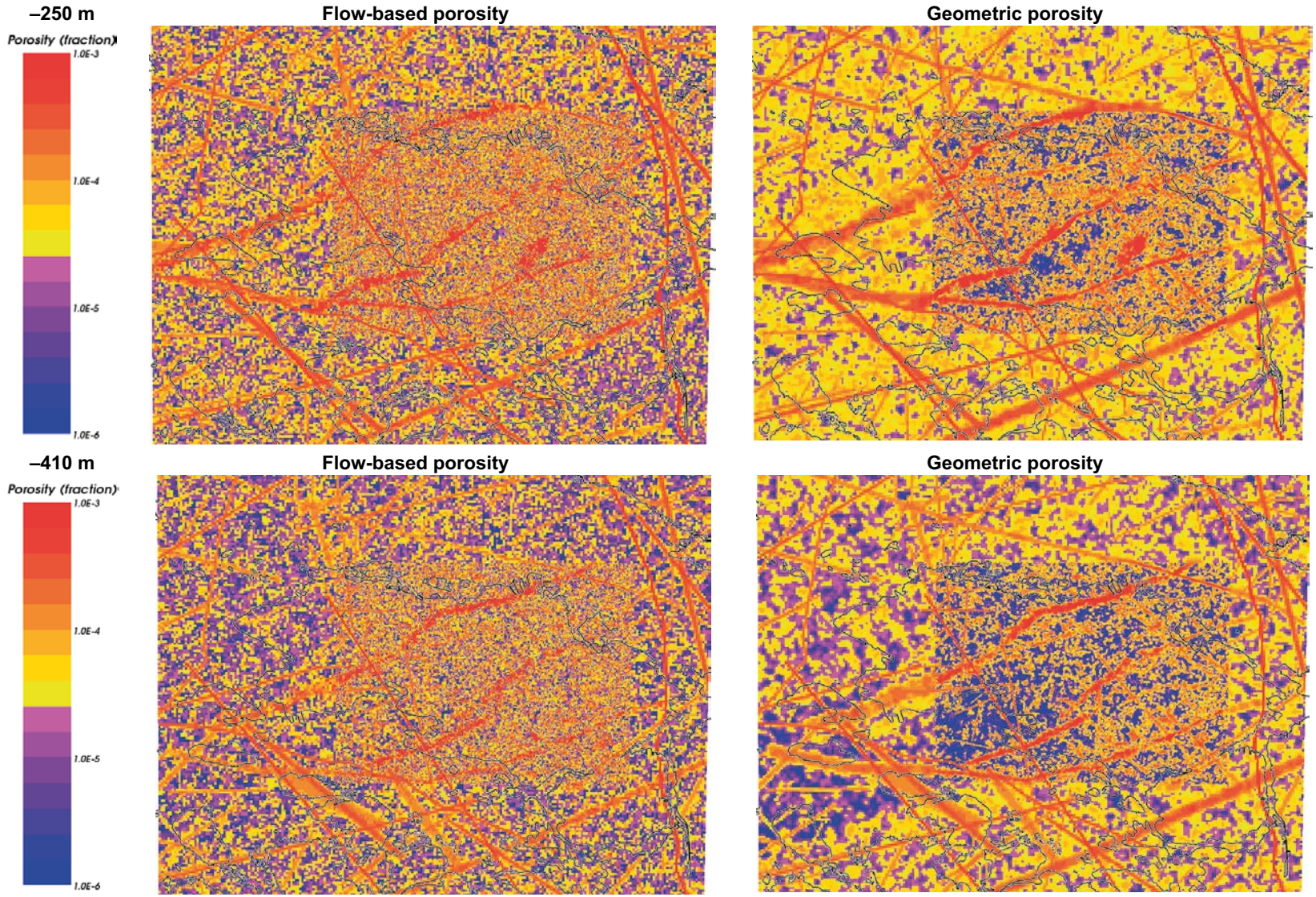

Figure 3-18 forts. *Horizontal slices through the ODFN 3.0 model at various depths showing porosity. Note that the porosity range shown varies with depth to emphasize the differences between the two methods.*

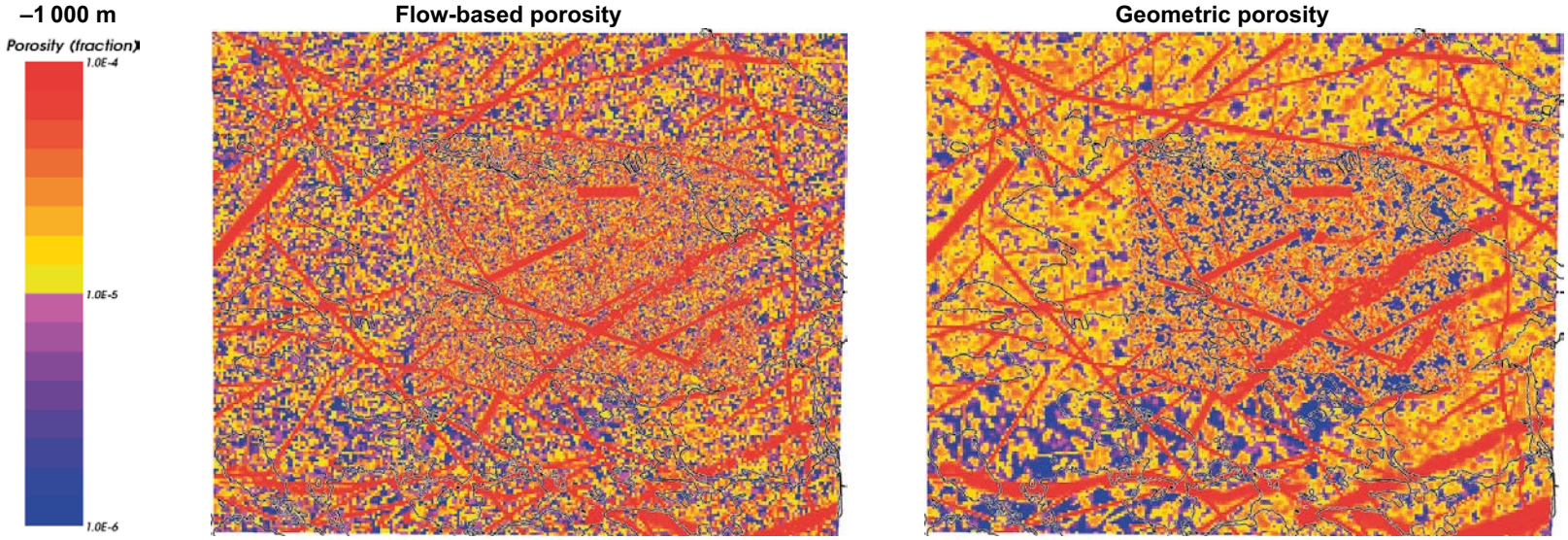

Figure 3-18 forts. *Horizontal slices through the ODFN 3.0 model at various depths showing porosity. Note that the porosity range shown varies with depth to emphasize the differences between the two methods.*

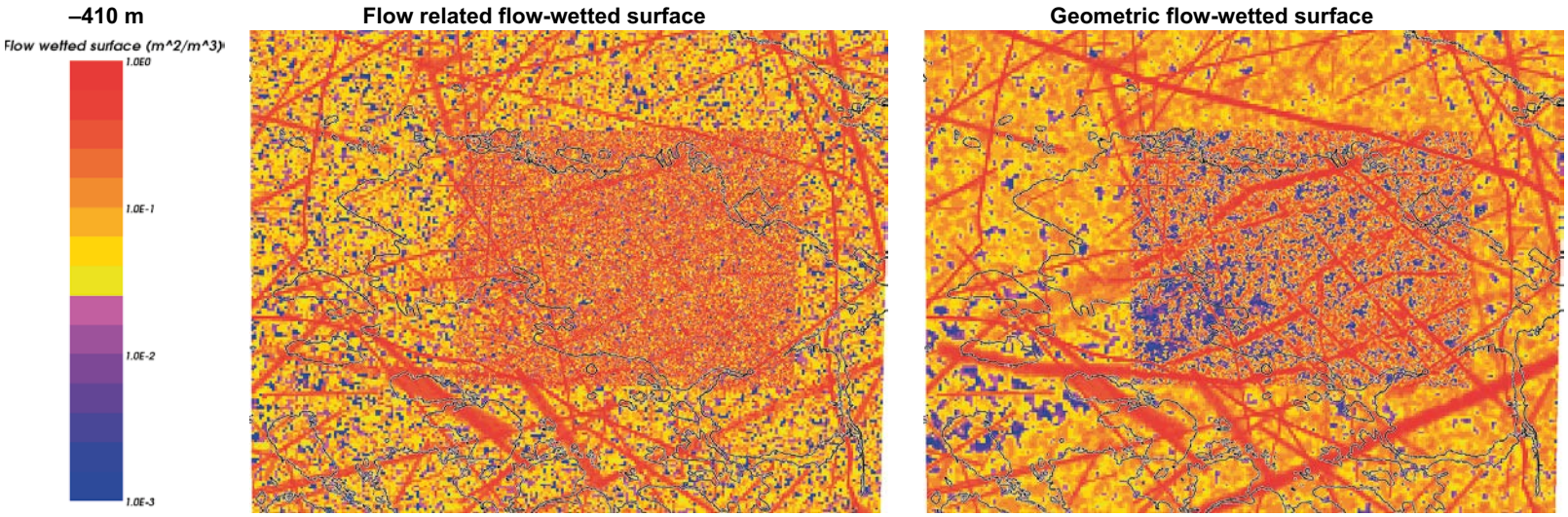

Figure 3-19. *Horizontal slices through the ODFN 3.0 model with minimum elevation at –410 m showing flow-wetted surface.*

3.4.2 Comparison of pathways

The model used in this section is the complete ODFN 3.0 model, including fracturing in both the rock mass and fault zones of Olkiluoto. However, the upscaling process does not include the stochastic faults and lineaments, with these added separately to the ECPM model to modify the properties through a process called down-scaling (see Subsection 4.1.1 for more details).

Here, pathways and their properties are compared between the underlying ODFN 3.0 model and two forms of ECPM models: one based on the geometric porosity; and the other one the flow-based porosity. Two sets of start points for the pathways are considered:

- **Repository start points:**
  The set consists of 4 376 points spread along the locations of the proposed deposition tunnels at roughly 10 m intervals. This type of investigation is relevant for future assessments of radionuclide release scenarios at Olkiluoto.
- **Selected fault zone start points:**
  In this investigation particles are released from 5 000 points spread evenly over the six faults zones listed in Table 4-2. One of the aims of this project is the direct comparison of DFN models in which the representation of fault zones is a swarm of almost parallel fractures, with DFN models where the faults are represented as equivalent properties specified on a mid-plane. This set of start points is directly applicable to such an investigation.

In this section, properties are generally compared between a single path in each of the ECPM and DFN models. However, some results are shown where 5 particles are released for each start point in the DFN model, and the properties geometrically averaged over the successful paths. For comparing the ECPM and DFN representations of the models, only release points which result in a successful DFN and ECPM pathway are considered.

The two ECPM models use identical conductivity tensors in each grid cell, so the pathway geometries simulated are identical. Only the transport properties differ due to the different approach for calculating kinematic porosity. The two transport properties reported in this subsection are travel time (T), and transport resistance (F) for pathways in the three models. The flow-related transport resistance, integrated along flow paths, quantifies the hydrodynamic aspects of the possible retention of solutes transported in a fractured medium. It can be defined in a number of ways which are interchangeable according to the basic definitions of hydraulic parameters characterising the system. In its most intuitive, although not necessarily most generalised form, the flow-related transport resistance is defined as the ratio of flow-wetted surface and flow-rate. The flow-related transport resistance governs nuclide migration, salt diffusion to and from the rock matrix, as well as oxygen ingress. An increase in flow-wetted surface for a given flow-rate, will yield a higher transport resistance; providing more retention of transported solutes.

Table 3-1 shows the median value for the ratios of travel times for the three models considered. The median for the repository start points is close to one. For the selected fault zone start points the DFN produces significantly shorter median times. In this case, the variation of depth where the particles are released varies from below 1 000 m to close to the surface. The ratio is similar for both ECPM models and independent of the number of particles per start point released in the DFN. The ratio of the two ECPM models for the repository release points is also interesting, reflecting the trend seen in Figure 3-18, where it can be observed that the porosity in the region of the repository is found to be smaller in most places when upscaling uses the geometric method. It is in this region where the pathways accumulate most of their travel time and transport resistance. This contrasts with the overall trend that the flow-based method yields smaller porosities than the geometric one; a likely explanation for this is the trend already observed in which the ratio of geometric to flow-based porosity tends to decrease with decreasing cell size and may fall below unity (Figure 3-7). The higher refinement in the repository region means that smaller cells are used, which may result in this behaviour. When considering the flow related transport resistance (Table 3-2), the main conclusions are the same as those determined for the median ratio of travel times.

In conclusion, both upscaling methods appear to adequately represent the DFN in the specific case of this model.

Table 3-1. Median of ratios of travel times (T) for pathways in the three models.

	$T_{DFN}/T_{ECPM\ (geom)}$	$T_{DFN}/T_{ECPM\ (flow\text{-}based)}$	$T_{ECPM\ (geom)}/T_{ECPM\ (flow\text{-}based)}$
Repository level start points	1.01	0.97	0.71
Repository level start points; 5 paths per start point in DFN	1.00	0.93	N/A
Selected BFZ start points	0.67	0.69	1.00
Selected BFZ start points; 5 paths per start point in DFN	0.69	0.71	N/A

Table 3-2. Median of ratios of transport resistance (F) for pathways in the three models.

	$F_{DFN}/F_{ECPM\ (geom)}$	$F_{DFN}/F_{ECPM\ (flow\text{-}based)}$	$F_{ECPM(geom)}/F_{ECPM\ (flow\text{-}based)}$
Repository level start points	1.24	1.47	0.70
Repository level start points; 5 paths per start point in DFN	1.26	1.50	N/A
Selected BFZ start points	0.89	1.18	1.19
Selected BFZ start points; 5 paths per start point in DFN	0.92	1.23	N/A

Pathway lengths are shown in Figure 3-20 and Figure 3-21. The first shows the cross plots for both sets of start points. There is reasonable correlation but a substantial spread. Despite this spread, the cumulative distributions shown in the second figure are close.

Travel time cross plots and distributions are shown in Figure 3-23. There is reasonable correlation, although for short pathways the DFN model produces shorter travel times. These are likely paths that travel most of their way through a fault zone or through a large stochastic fracture. This applies to both sets of start points. The cross plot for the two ECPM models shows good correlation for shorter paths but for longer paths the flow-based method produces longer travel times. The same information is shown in the cumulative distribution in Figure 3-22.

Transport resistance cross plots and distributions are shown in Figure 3-24 and Figure 3-25. Conclusions are much the same as for travel time, but the comparison between the two ECPM models shows a more pronounced reduction in resistance for low-resistance pathways using the geometric method, and this trend is still visible for the selected fault zone start points. Low resistance pathways are likely to be ones where after a short period near the repository the particles are entrenched in a significant flowing feature. The resistance calculated using the flow-based method provides a closer match to the DFN result for these pathways; for the longer, higher-resistance paths from repository start points, the opposite is true. These paths will likely travel through regions with larger block sizes and may go to greater depth, where the effects on porosity discussed for Figure 3-18 become relevant again; this may provide an explanation for this result.

Exit points of pathways starting at both the repository and in fault zones are shown in Figure 3-26. Exit points are shown for the ECPM models (both have the same pathways) and for the DFN for a single particle per start point and five particles per start point. In some areas there is good correlation, but the ECPM models cannot reproduce the pathways that travel substantial distances through channels formed by fractures. For example, in the case of repository start points, there are quite a few DFN exit points to the west of the repository, but hardly any ECPM ones.

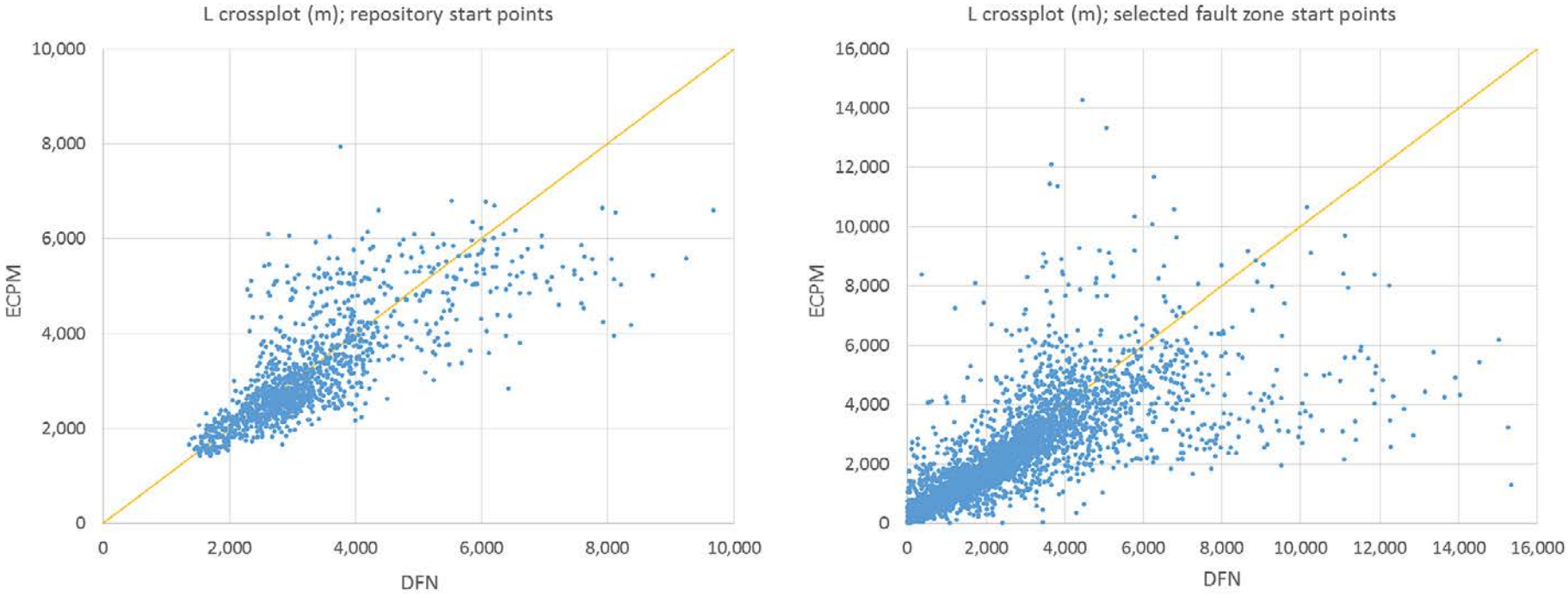

Figure 3-20. *Cross plot of the pathway length (L) for each start point in the two sets. Paths have identical geometries in the two ECPM models.*

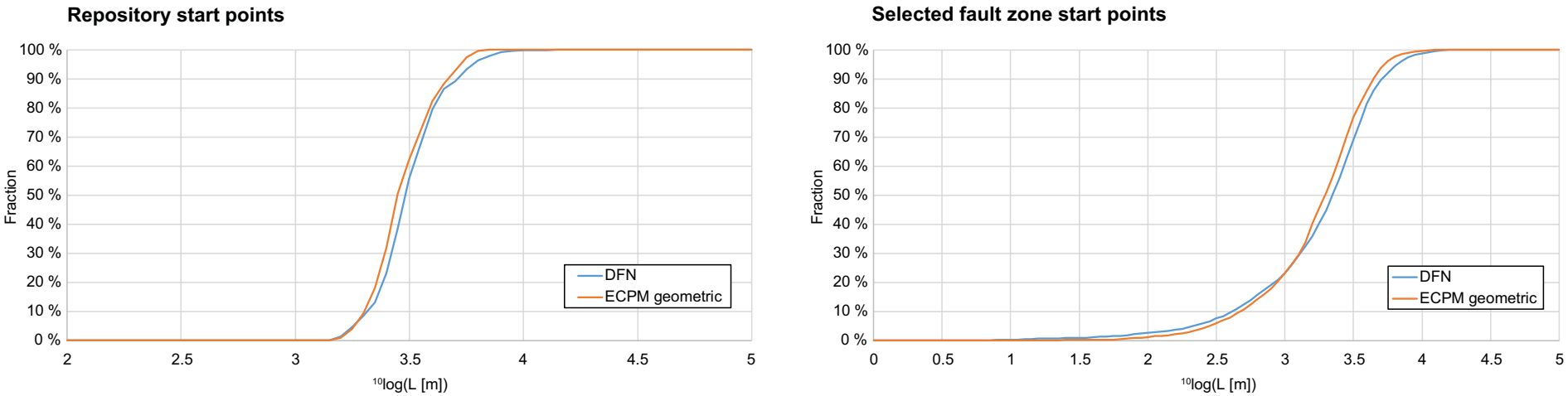

Figure 3-21. *Cumulative distribution function of pathway lengths (L) for the two sets of start points.*

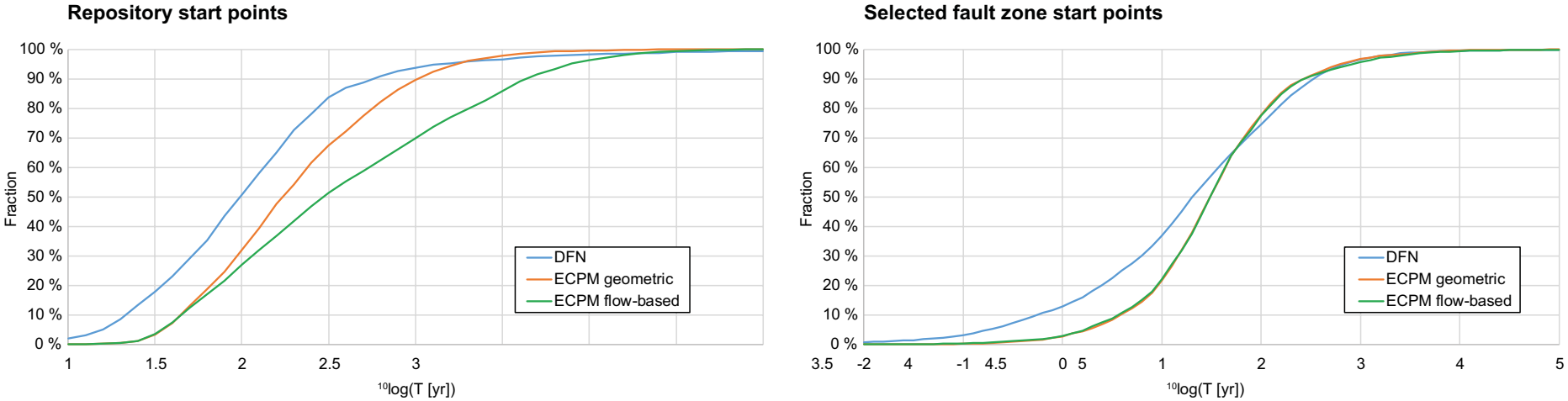

Figure 3-22. *Cumulative travel time (T) distributions for the two sets of start points.*

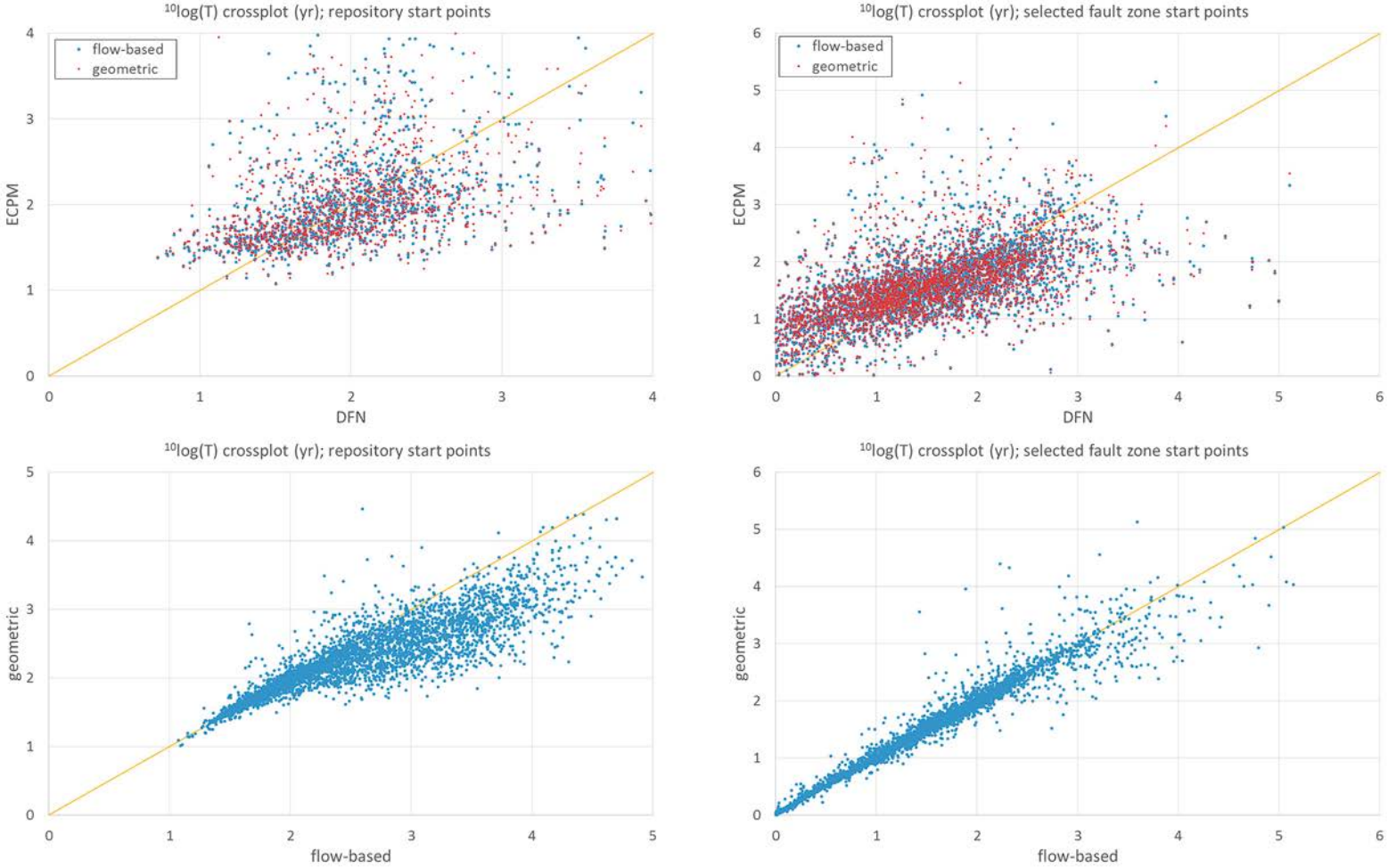

Figure 3-23. *Cross plots of travel time (T) for the two sets of start points. Comparison between the DFN and the two ECPM models at the top and between the two ECPM models at the bottom.*

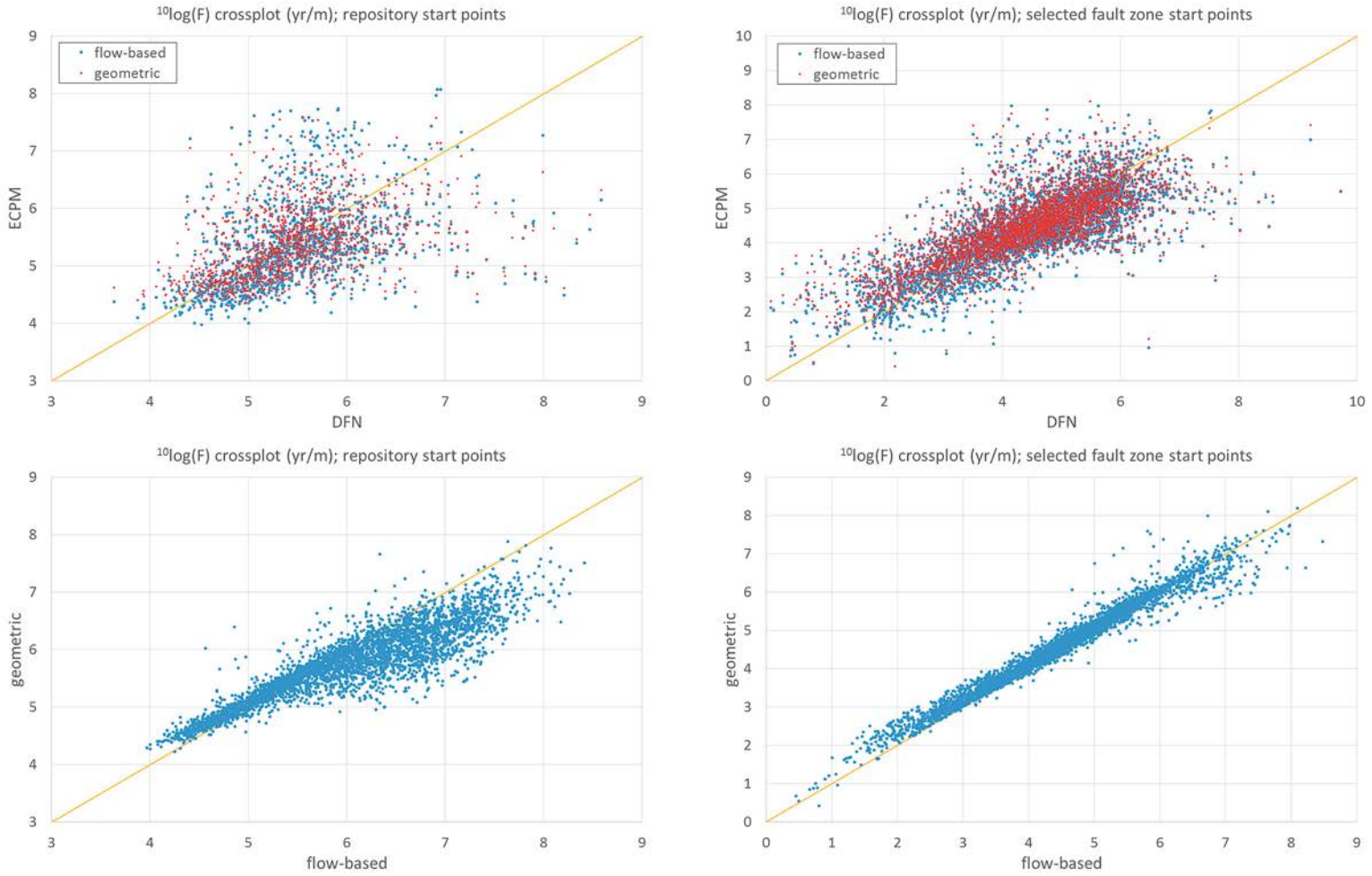

Figure 3-24. *Cross plot of transport resistance (F) for the two sets of start points. Comparison between the DFN and the two ECPM models at the top and between the two ECPM models at the bottom.*

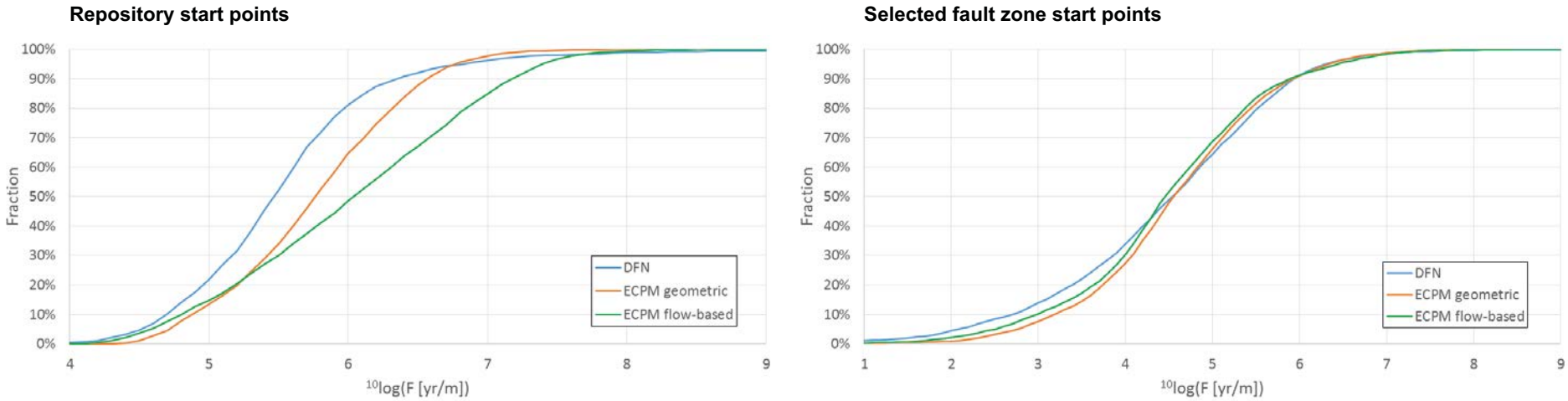

Figure 3-25. *Cumulative distribution of transport resistance (F) for the two sets of start points.*

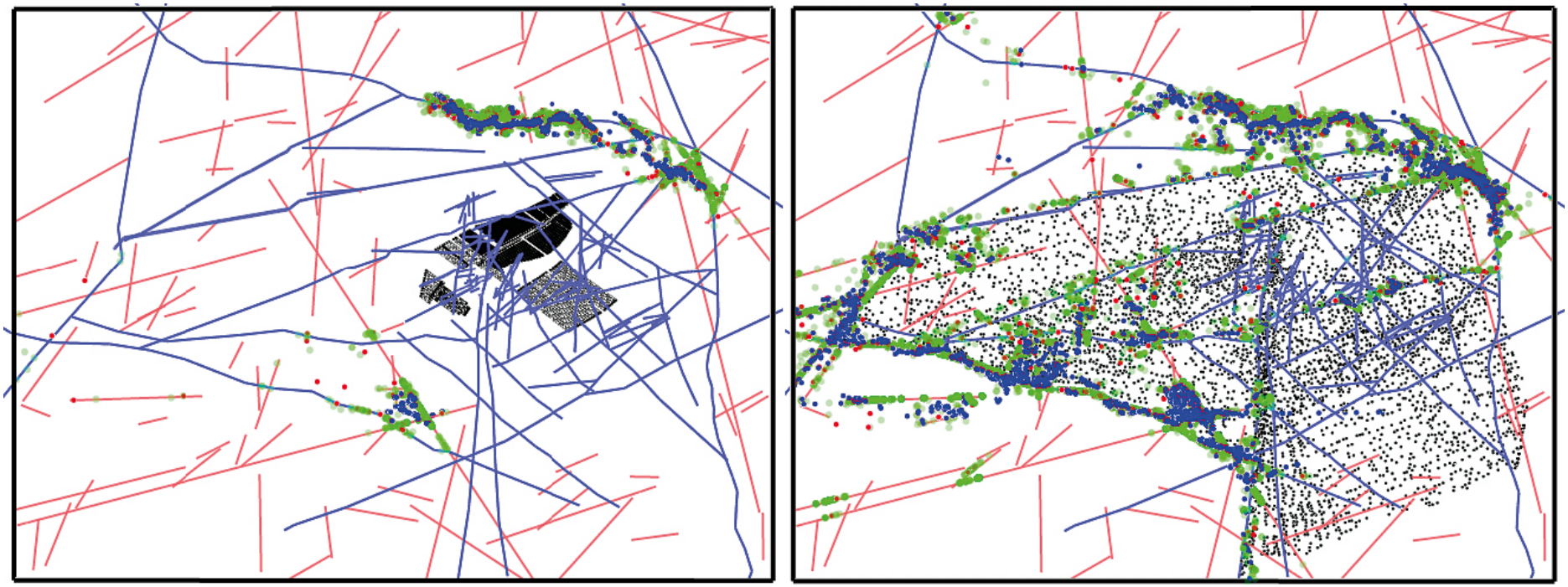

Figure 3-26. *Start and exit points. Repository start points on the left and selected fault zone start points on the right. Start points are in black. ECPM exit points are dark blue, DFN exit points in red and exit points in the DFN with 5 particles per start point in green.*

4 Upscaling and projection of BFZ flow and transport properties

4.1 Integrating BFZ with ECPM models of Olkiluoto site

In the traditional approach to developing an ECPM model (discussed in Section 3.1), only the stochastic "background" fractures are used in the upscaling process. The brittle fracture zones (BFZs) have historically been represented as complex single fractures with physical properties that can vary with location. These are planar structures and incorporated into the ECPM model using a process called downscaling, which is discussed in Subsection 4.1.1.

In the new approach, the BFZs are represented as a set of almost parallel, but intersecting, fractures. The fracture size is random using a power law distribution in some size range, typically 10 to 50 m, c.f. Chapter 2. With the BFZ represented as fracture swarms in this approach, the flow-based upscaling method can be applied directly to the DFN (comprising background fractures and BFZ fracture swarms) using the methodology described in Subsection 3.2.2. Although this methodology provides a well-founded approach to BFZ property description, it is difficult to communicate the properties it implies and the sensitivity of those properties to uncertain DFN parameters such as size distribution and intensity. Related to this is the issue of how to parameterise models of fault zones where the end-user requires a simplification of the zone to a plane with effective properties (transmissivity, porosity, and flow wetted surface). Therefore, in Subsection 4.1.2 a methodology is developed to post-process these upscaled models to derive the effective in-plane transmissivity, porosity and flow wetted surface of each BFZ.

4.1.1 Downscaling of brittle fracture zones

In the traditional approach to creating an ECPM model, fault zones are represented by modifying the hydraulic properties of any finite-elements intersected by one or more faults to incorporate the properties of the faults using the Implicit Fracture Zone (IFZ) method in ConnectFlow, as described in (Marsic et al. 2001); this is referred to as "downscaling" of the BFZ properties. If an element is intersected by a fault zone, then the hydraulic properties of that element would be expected to change. In the ECPM model, the methodology consists of first creating the realisation of the stochastic DFN (including the fault zones to provide connectivity) on the regional-scale and then, using the upscaling methods described in Subsections 3.1 and 3.2, convert this to a realisation of the ECPM model, with the faults removed. This is followed by a downscaling step in which the IFZ method is applied to modify the ECPM model properties such that they incorporate the effect of the fault zones.

In DFN models, the fault zones are modelled as surfaces which are composed of many rectangular or triangular planes that discretise the geometry and hydraulic properties. Transmissivity is typically depth-dependent and may also depend on the dip of the zone. Therefore, it is necessary to sub-divide the zones into relatively small sub-fractures to represent such property variations.

The IFZ method identifies which elements are crossed by a fault zone and combines a hydraulic conductivity tensor associated with the fault with a hydraulic conductivity tensor for the background stochastic network. For each element crossed by the fault zone the following steps are performed:

- The volume of intersection between the fault zone and the element is determined.
- The hydraulic conductivity tensor of the background rock is calculated in the coordinate system of the fault zone.
- The combined conductivity tensor of the background rock and the fault zone is calculated in the coordinate system of fault zone.
- The effective hydraulic conductivity tensor that includes the effect of the fault zone is determined in the original coordinate system.

The methodology is illustrated in Figure 4-1. In 3D, the resultant hydraulic conductivity is a 6-component symmetric tensor in the Cartesian coordinate system. The tensor can be diagonalised to give the principal components and directions.

Similarly, a combined grid cell porosity is calculated for the element, based on combining the fault zone porosity and the background grid cell porosity using a relative transmissibility (total channel flow capacity, which is transmissivity times flow length in the element [m^3/s]). This is suitable for transport since it weights the combined porosity toward the fault zone porosity if this is of a relatively high hydraulic conductivity. The result of this process is to produce a spatial distribution of ECPM element properties (hydraulic conductivity tensor, porosity and flow wetted surface) that represent the combined influence of both the fault zones and background stochastic fractures.

It may be noted the term "background conductivity" here means the equivalent conductivity of the stochastic fracture network. No extra component for matrix conductivity is added. However, the stochastic DFN is necessarily truncated in some way, e.g. based on fracture transmissivity which in consequence means that some elements may not include a connected network of fractures or may only be connected in some directions. To avoid this just being a result of the choice of truncation limit and chance, a minimum grid cell conductivity and porosity is set for any elements that have zero properties following the fracture upscaling and IFZ methods. Appropriate minimum properties can be derived by calculating the minimum values seen when the DFN is truncated only at very small fractures relative to the grid cell size, and so are essentially free from the truncation effect.

4.1.2 Upscaling BFZ to planar properties

The transport upscaling methodology demonstrated in Chapter 3 also provides hydrogeological properties for cells that span the damage zone of each fault zone (see for instance Figure 3-18 and Figure 3-19). Within this subsection, a methodology is developed to post-process these upscaled models to derive the effective in-plane transmissivity, mean porosity and flow wetted surface of each fault zone. Such a methodology provides a more conventional hydraulic description for the underlying fault related fracture swarms used to represent each zone. The implementation of the developed methodology is integrated with DFNdb v1.1 (Hartley et al. 2018, Baxter et al. 2016) to allow for seamless interpretation of the data used for fracture conceptualisation and modelling in support of Posiva's latest SDM. As such, the software packages used to implement the techniques were Python 2.7.6 and PostgreSQL 9.5. This approach has the additional benefit of being able to draw on the powerful geometric functionality of postGIS which forms a key component of the database.

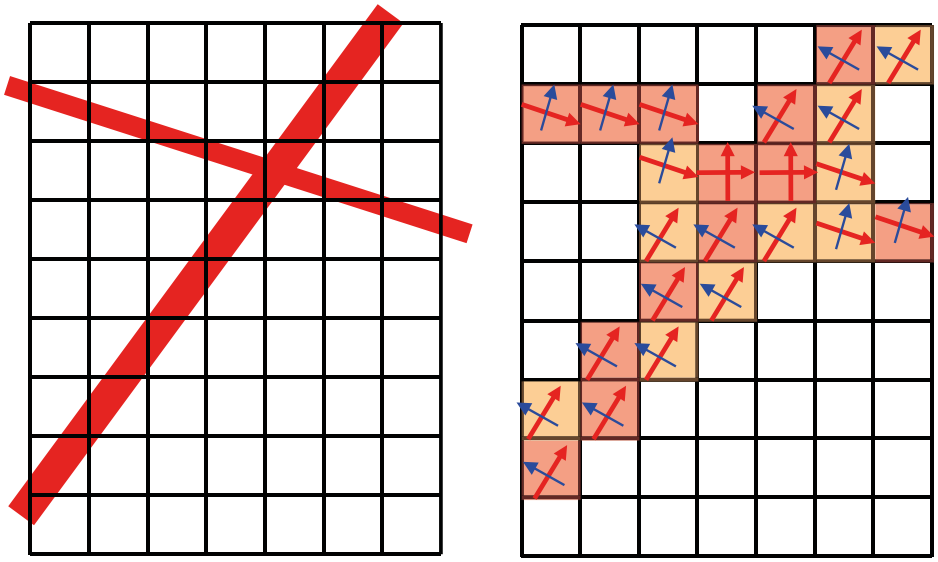

Figure 4-1. *Schematic illustration of the modification of the hydraulic conductivity tensor by the presence of brittle fracture zones using the IFZ method. A finite-element grid crossed obliquely by two BFZs of different thickness (left). The additional contributions to the hydraulic conductivity tensor due to these BFZs; positive (red) in the direction parallel to the plane and negative (blue) in the direction normal to it, with cells crossed by multiple BFZs having positive contributions in multiple directions (right).*

The transport upscaled DFN models for the Olkiluoto site are detailed in Section 3.4 and consist of nearly 12 million elements at two levels of discretisation (an outer region consisting of elements with side length of 30 m and inner region elements with side length of 10 m). When upscaling fault zone properties, care should be taken in choosing the size of elements used. The thickness of faults at Olkiluoto varies from less than 1 m up to about 30 m, and therefore the typical element should be scaled similarly, to ensure the fault zone fracture swarm dominates the upscaled properties. While 10 m is an acceptable choice for the six large and thick zones upscaled in this study (see Section 4.2), a smaller element size would be necessary for upscaling thinner zones.

Overall the adopted procedure can be split into three phases. The first phase (Step 1 below) handles the extraction of the equivalent properties from the ConnectFlow transport upscaling, identifying those grid cells associated with each BFZ. The upscaling properties exported are the porosity φ, flow wetted surface α_r and six component permeability tensor k_{ij}. The second phase (Steps 2 and 3 below) represents the projection and aggregation of cell based properties of the upscaled DFN onto the framework of the planar BFZ. Finally, the last phase (Step 4 below) details the aggregation of the computed effective properties calculated at the resolution of the upscaled grid to calculate equivalent properties for individual tessellates of the BFZ. These phases are expanded below detailing the steps of the calculation, with a schematic illustration of the methodology for calculating effective BFZ properties from the upscaled DFN model illustrated in Figure 4-2.

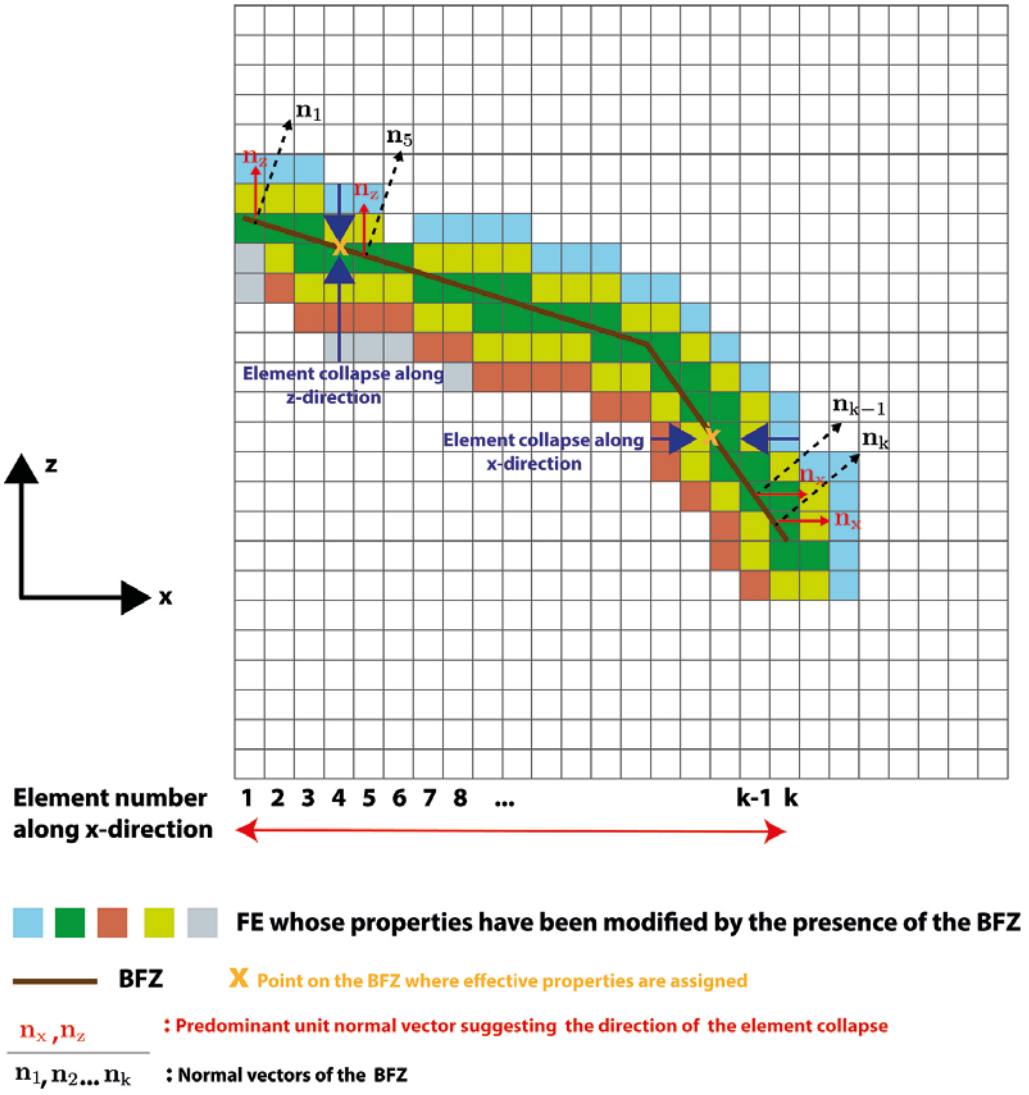

Figure 4-2. *Schematic illustration of how BFZ related upscaled cell properties are identified, averaged and collapsed down to an in-plane transmissivity, fracture aperture and flow wetted surface. Two collapse directions are depicted (x and z); these are equal to the largest Cartesian component of the local BFZ normal, and can thus vary over the BFZ surface if it consists of more than one plane.*

Step 1. Identify all cells associated with each fault zone where either the fault mid-plane crosses a cell, or the cell has some part within the damage zone of the fault.

The transport upscaled ConnectFlow simulations, including grid, are first imported into the geospatial database DFNdb v1.1. For each grid cell the following is stored:

- Element number from the underlying site-scale grid.
- A polygon representation of the grid cell geometry.
- Extraction of kinematic porosity, φ and flow wetted surface α_r.
- Extraction of the six components of the symmetric permeability tensor, k_{ij}.

Within the database the triangulated mid-planes of the fault zones are also stored, including a polygonal representation of the geometry as well as associated properties such as orientation and damage zone thickness (H). The process to identify all grid cells within the modelling domain that correspond to the fault zone is performed in the following stages:

1. The geospatial database is first queried (using the postGIS functionality) to identify those grid cells intersected by the fault. Figure 4-3 illustrates such an identification for BFZ020a (orange) and BFZ146 (blue).
2. With the upscaled grid oriented to the Cartesian axis; for each fault, the unit normal based on the largest component of the fault normal is calculated (based on the overall orientation of the fault structure). This unit normal is denoted the "*collapse direction*" and defines which of the ordinate directions the upscaled grid properties will be aggregated.
3. For each grid cell intersecting the fault zone (see stage 1) a line geometry is defined based on the centroid of the grid cell, and the *collapse direction* unit vector. The length of this line string is such that it extends to the damage zone thickness (accounting for the difference in orientation of the fault normal and *collapse direction*). The line string is defined to reflect the different thickness of the damage zone in the hanging wall and footwall of the fault.

Step 2. Gather the properties of each cell along the axial line closest to normal to the fault plane.

Based on the line geometries calculated in Step 1:

- Calculate the intersection between each line geometry and the grid cells in the upscaled model. Note that as the grid cells are represented as a polygon of their external surface, this will have the effect of extending the damage zone thickness to an integer number of grid cells. These cells define the upscaled properties to be aggregated and collapsed on to the BFZ mid-plane.
- When repeated for all line geometries, this will form a regular distribution of collapse points on the fault zone mid-plane (at the resolution of the upscaled grid); and for each collapse point a list of cells and properties for aggregating based on the damage zone thickness will be stored.

Step 3. For transmissivity, porosity and permeability, calculate the equivalent properties in the plane of the fault over each cell along the axial line, to calculate property values at a series of points on the fault mid-plane at the density of the ECPM grid.

The first stage of calculating equivalent properties on the fault zone mid-plane requires the permeability tensor $\boldsymbol{k}$, to be rotated into the frame of reference of the fault. A rotation matrix $\boldsymbol{Q}$ is defined based on the rotation between the fault zone's unit normal and the *collapse direction*, identified in Step 2 and used to calculate the rotated permeability tensor as $[\dot{\boldsymbol{k}}] = [\boldsymbol{Q}]\,[\boldsymbol{k}]\,[\boldsymbol{Q}^T]$.

It remains to calculate effective properties on the fault mid-plane for porosity, flow wetter surface and transmissivity at the resolution of collapsed grid cells.

- For the assignment of porosity and flow wetted surface, a simple arithmetic mean approach is used. That is, across the n grid cells used to represent the damage zone thickness, the effective porosity on the fault mid-plane corresponding to the collapsed grid cells is given as $\overline{\varphi}=\frac{1}{n}\sum_{i=1}^{i=n}\varphi_i$, whilst the effective flow wetted surface is obtained as $\overline{a_r}=\frac{1}{n}\sum_{i=1}^{i=n}a_{r_i}$.

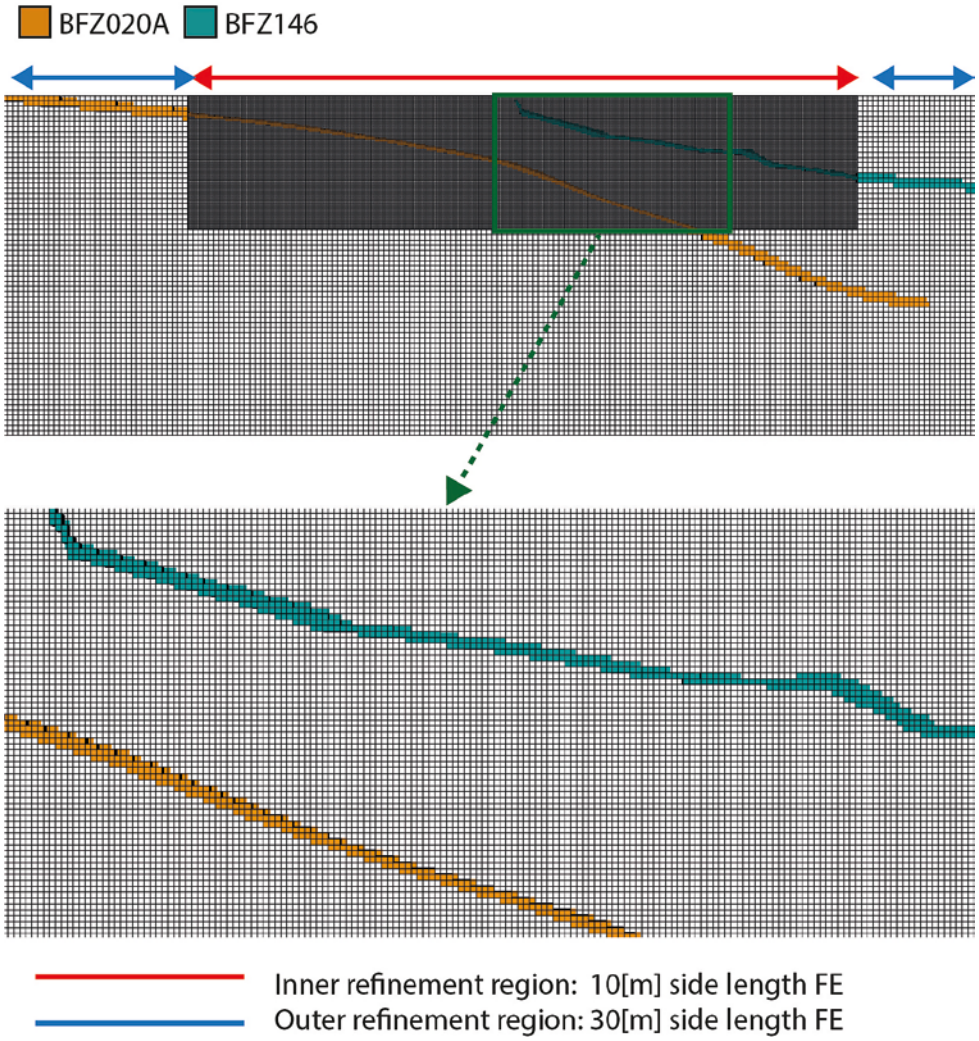

Figure 4-3. *A slice of the computational domain showing the grid cells intersected by the BFZ020a (orange elements) BFZ146 (blue elements).*

- The calculation of the effective transmissivity at the fault mid-plane is slightly more complicated. First, the in-plane component of the rotated permeability tensor in each grid cell is identified based on the direction of collapse:
  - When the *collapse direction* = (0,0,1), the in-plane permeability is: $\widehat{k_i} = \sqrt[2]{|\dot{k}^i_{11}\dot{k}^i_{22} - \dot{k}^{i\,2}_{12}|}$
  - When the *collapse direction* = (0,1,0), the in-plane permeability is: $\widehat{k_i} = \sqrt[2]{|\dot{k}^i_{11}\dot{k}^i_{33} - \dot{k}^{i\,2}_{13}|}$
  - When the *collapse direction* = (1,0,0), the in-plane permeability is: $\widehat{k_i} = \sqrt[2]{|\dot{k}^i_{22}\dot{k}^i_{33} - \dot{k}^{i\,2}_{23}|}$

  The arithmetic mean of these in-plane permeabilities is subsequently calculated across the grid cells, weighted by the size of the individual grid cell as larger cells provide more accurate estimates of effective permeability (recall cells in the inner region of the grid are 10 m, whereas those outside this region are 30 m). The effective transmissivity at the mid-plane of the fault zone is then calculated as:

$$T = H\,\frac{\rho g}{\mu}.\frac{\sum_{i=1}^{i=n} h_{cell}\widehat{k_i}}{\sum_{i=1}^{i=n} h_{cell}}$$

  Where H is the damage zone thickness, h_{cell} is the length scale of cell i in the *collapse direction*, and ρ and μ are fluid properties for density and viscosity.

Step 4. Aggregate the properties identified from the upscaled grid to define values for porosity, flow wetted surface and transmissivity for each tessellate on the fault zone mid-plane.

The final step of the methodology is the aggregation of the properties collapsed onto the fault zone mid-plane (at the scale of the upscaled grid) to provide values for porosity, flow wetted surface and transmissivity at the scale of the triangulation of the fault mid-planes[1]. For each tessellate of the fault:

- Values for porosity and flow wetted surface are calculated from the arithmetic average of the upscaled properties collapsed on each tessellate of the fault mid-plane.
- Values for the transmissivity are calculated as the geometric mean of the upscaled properties collapsed on each tessellate of the fault mid-plane. This geometric mean value is further scaled by the proportion of collapsed grid cells which are active for flow (i.e. the proportion of collapsed grid cells in Step 3 where $\sum_{i=1}^{i=n} h_{cell}\widehat{k_i}$ is non-zero). This scaling is used to account for the proportion of each tessellate of the fault zone mid-plane which is open to flow.

[1] The relative scale of the BFZ triangulation to the resolution of the upscaled grid should be considered. In this case, a maximum triangle surface area of 5 000 m^2 for the BFZ tessellates was enforced in order to ensure each triangle included more than one property point collapsed from the upscaled grid.

4.2 Example results for Olkiluoto

The methodology presented in Section 4.1.2 provides a generic approach for reducing the detailed description of fault damage zones, individual fault related fractures and their hydromechanical properties as adopted in ODFN 3.0 to a more conventional hydrogeological property model of transmissivity, porosity and flow wetted surface for the purposes of communication and downstream modellers requiring a simplified representation of the fault. Specifically, although this methodology could be applied to all fault zones included in ODFN 3.0, from herein the results from applying the above approach are shown solely for six of the most significant fault zones at Olkiluoto for flow and transport, namely BFZ020a, BFZ045, BFZ084, BFZ099, BFZ100, and BFZ146. These vary in major side length from ~1 km (BFZ045 and 084) to 6 km (BFZ099) – see Table 4-1.

Table 4-1. Side lengths in the strike and dip directions of the six fault zones considered.

Fault zone	Strike length (m)	Dip length (m)
BFZ020a	5 000	2 500
BFZ045	1 048	518
BFZ084	950	720
BFZ099	6 000	3 500
BFZ100	3 730	650
BFZ146	3 500	3 100

An example of the effective in-plane transmissivity and kinematic porosity as represented on a triangulated grid over these six fault zones are shown in Figure 4-4 through Figure 4-7. The triangulations were obtained by iteratively applying a triangle tessellation function until the surface area of each resulting triangle was less than a user-supplied tolerance, which in all cases was 5 000 m^2. Apparent variations in the size of triangles are therefore due to the difference in length scales between fault zones, as discussed above; these figures do not use the same scale for each fault zone.

A general depth trend is seen due to the effects of *in situ* stress, as is heterogeneity due to the zone being made up of individual stochastically generated fractures. For BFZ020a, the increased transmissivity in the western half of the zone is a function of the interpreted thicknesses and their interpolation.

Statistics for transmissivity, porosity and flow wetted surface are shown in Table 4-2 through Table 4-4. For all but BFZ146, the 5th percentile of aggregated properties from the grid cells collapsed to the fault zone mid-plane is 0, an indication of the frequency of grid cells within the upscaled DFN that do not percolate. For BFZ084 and BFZ100, the values remain 0 at the 25th percentile, suggesting a large proportion of the DFN swarms representing these faults are disconnected at the scale of the upscaled grid. This is likely caused by regions of these fault zones having a damage zone of limited extent and/or relatively low intensity.

In addition to the above, a simple summary of the resulting upscaled properties of each of the six fault zones are presented; indicating distributions of transmissivity (Figure 4-8) and porosity (Figure 4-9) geometrically averaged over 50 m depth bands within each fault, and then fitted by linear regression. For flow wetted surface (Figure 4-10), arithmetic averaging is used. The variability at each depth provides an indication of the heterogeneity due to the zone being made up of individual stochastically generated fractures. The depth trends are due to the effects of *in situ* stress.

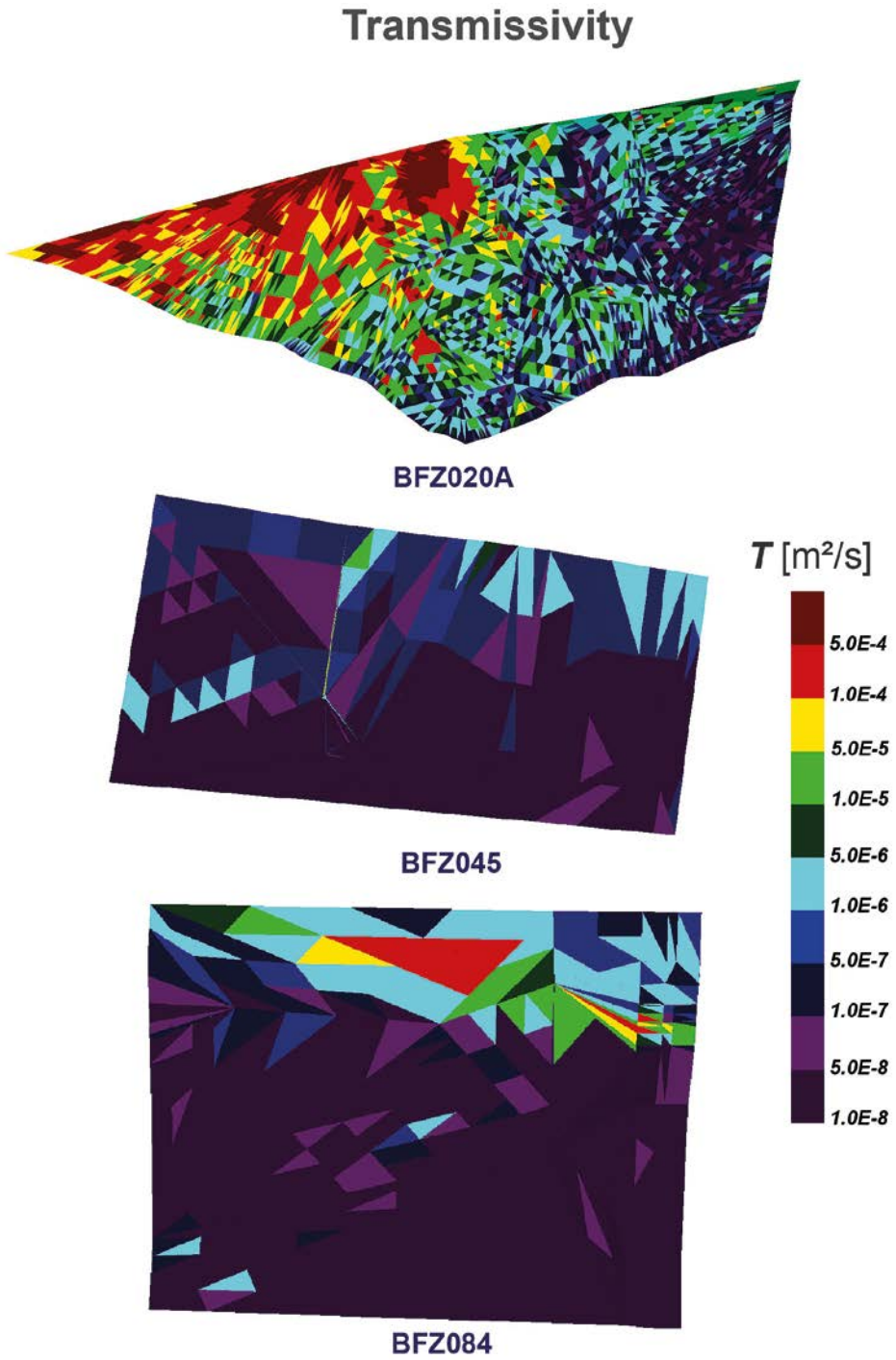

Figure 4-4. *Transmissivity T* [m^2/s] *for BFZ020a, BFZ045 and BFZ084 as obtained at the fault zone mid-plane.*

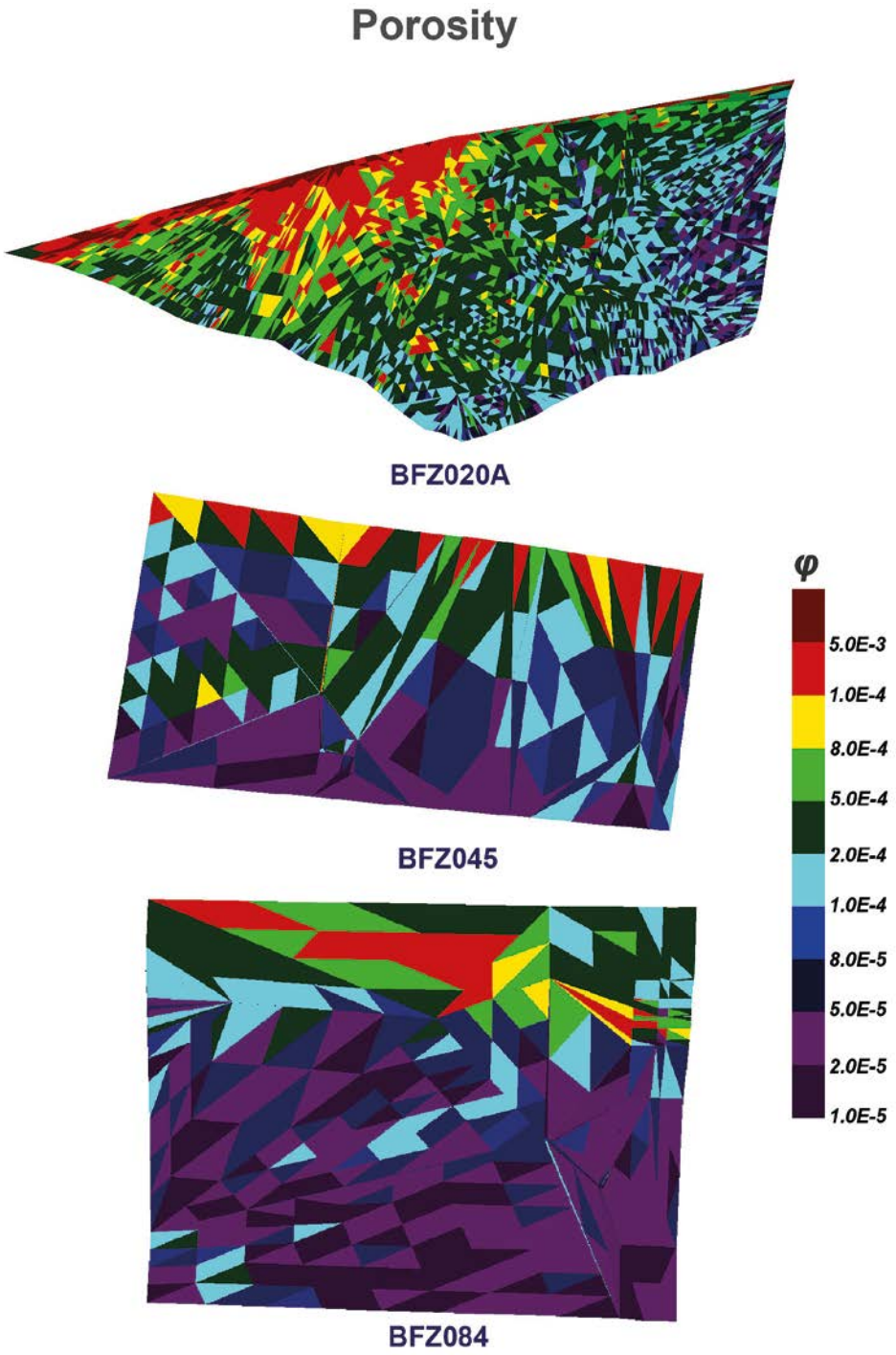

Figure 4-5. *Porosity* φ *for BFZ020a, BFZ045 and BFZ084 as obtained at the fault zone mid-plane.*

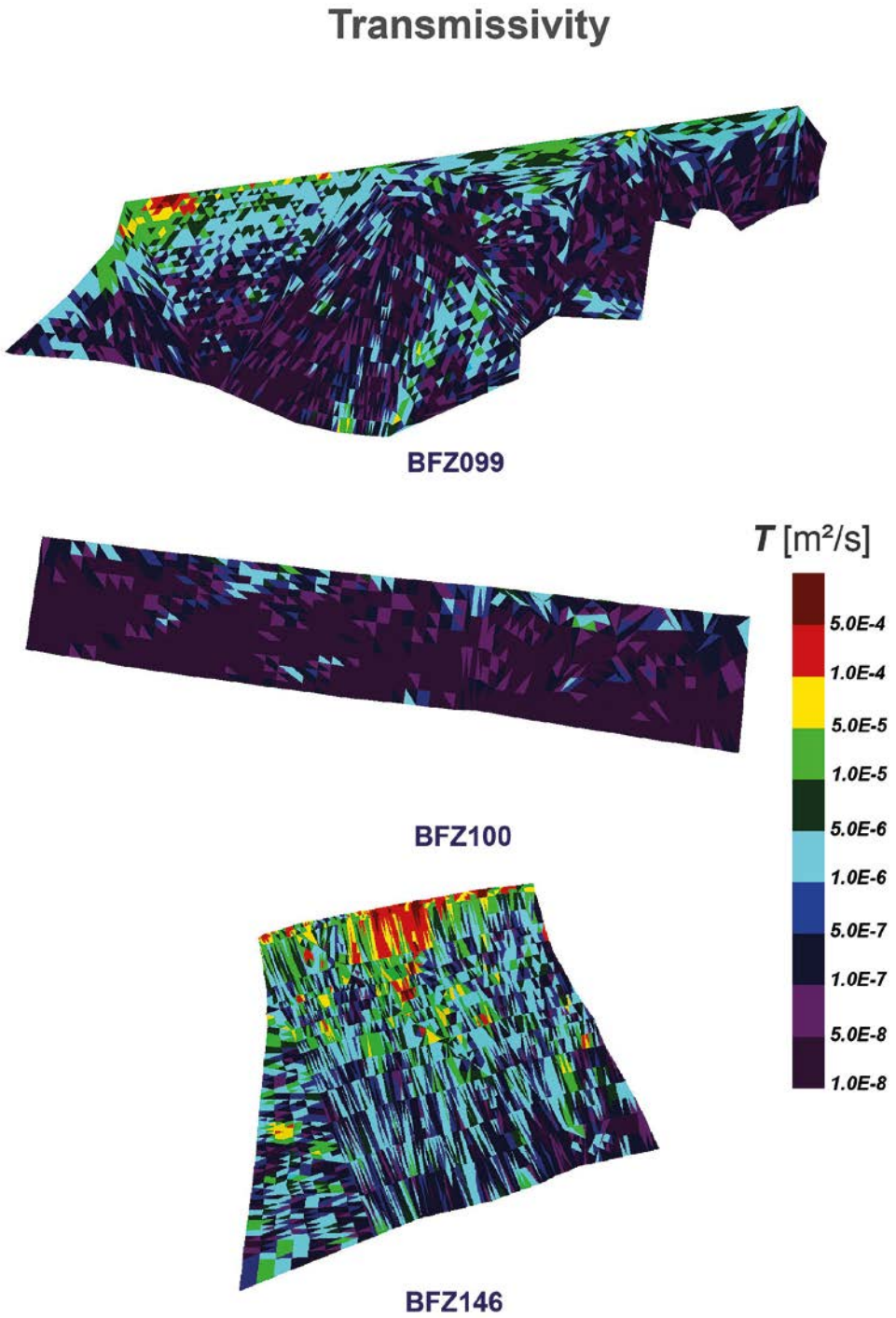

Figure 4-6. *Transmissivity T* [m^2/s] *for BFZ099, BFZ100 and BFZ146 as obtained at the fault zone mid-plane.*

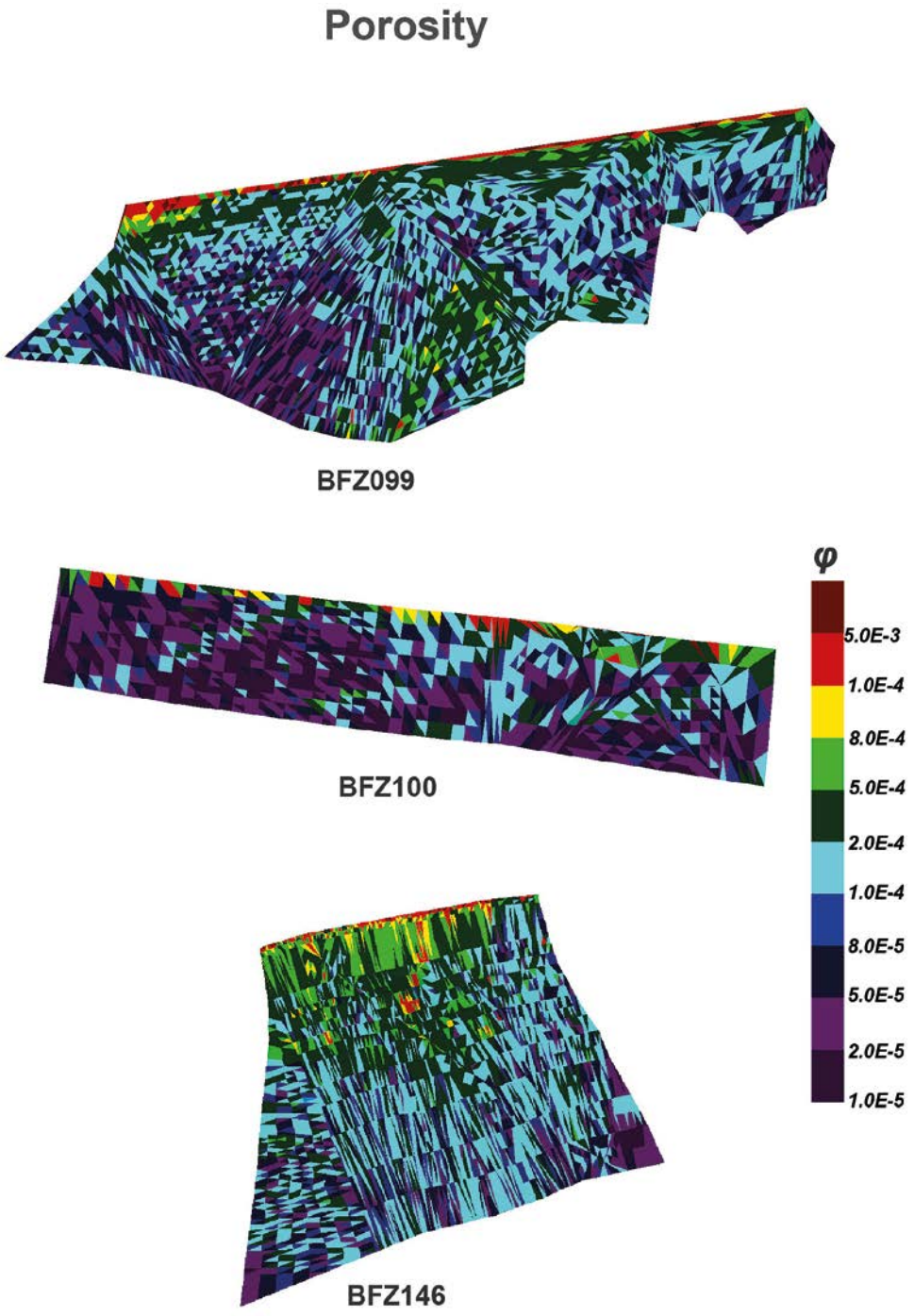

Figure 4-7. *Porosity* φ *for BFZ099, BFZ100 and BFZ146 as obtained at the fault zone mid-plane.*

Table 4-2. Median values and the 5th, 25th, 50th, 75th and 95th percentiles of the Transmissivity T [m^2/s], for the six fault zones considered.

Fault zone	$\overline{T}$	T_{p5}	T_{p25}	T_{p50}	T_{p75}	T_{p95}
BFZ020a	1.25×10^{-4}	0.00	4.65×10^{-7}	6.55×10^{-6}	5.40×10^{-5}	6.26×10^{-4}
BFZ045	3.41×10^{-6}	0.00	3.65×10^{-9}	4.88×10^{-8}	5.35×10^{-7}	1.00×10^{-5}
BFZ084	3.08×10^{-5}	0.00	0.00	3.06×10^{-8}	7.85×10^{-7}	9.64×10^{-5}
BFZ099	3.66×10^{-6}	0.00	4.56×10^{-8}	3.36×10^{-7}	2.05×10^{-6}	1.71×10^{-5}
BFZ100	2.70×10^{-6}	0.00	0.00	2.01×10^{-8}	3.29×10^{-7}	8.48×10^{-6}
BFZ146	5.92×10^{-5}	4.27×10^{-9}	8.08×10^{-7}	7.13×10^{-6}	4.01×10^{-5}	3.28×10^{-4}

Table 4-3. Median values and the 5th, 25th, 50th, 75th and 95th percentiles of the porosity φ, for the six fault zones considered.

Fault zone	$\overline{\varphi}$	φ_{p5}	φ_{p25}	φ_{p50}	φ_{p75}	φ_{p95}
BFZ020a	5.28×10^{-4}	0.00	1.08×10^{-4}	2.91×10^{-4}	6.28×10^{-4}	1.61×10^{-3}
BFZ045	5.28×10^{-4}	0.00	1.08×10^{-4}	2.91×10^{-4}	6.28×10^{-4}	1.61×10^{-3}
BFZ084	2.98×10^{-4}	0.00	0.00	5.51×10^{-5}	2.30×10^{-4}	1.56×10^{-3}
BFZ099	2.31×10^{-4}	0.00	5.37×10^{-5}	1.27×10^{-4}	2.60×10^{-4}	6.37×10^{-4}
BFZ100	3.26×10^{-4}	0.00	0.00	4.76×10^{-5}	1.93×10^{-4}	1.21×10^{-3}
BFZ146	3.97×10^{-4}	1.01×10^{-5}	1.06×10^{-4}	2.53×10^{-4}	5.12×10^{-4}	1.13×10^{-3}

Table 4-4. Median values and the 5th, 25th, 50th, 75th and 95th percentiles of the flow wetted surface α_r $[1/m]$ for the six fault zones considered.

Fault zone	$\overline{\alpha_r}$	α_{rp5}	α_{rp25}	α_{rp50}	α_{rp75}	α_{rp95}
BFZ020A	2.02×10^{-1}	0.00	7.60×10^{-2}	1.40×10^{-1}	2.30×10^{-1}	5.41×10^{-1}
BFZ045	4.69×10^{-1}	0.00	4.43×10^{-2}	1.20×10^{-1}	2.43×10^{-1}	1.66
BFZ084	1.53×10^{-1}	0.00	0.00	8.84×10^{-2}	1.87×10^{-1}	5.14×10^{-1}
BFZ099	2.13×10^{-1}	0.00	7.41×10^{-2}	1.44×10^{-1}	2.37×10^{-1}	5.22×10^{-1}
BFZ100	2.96×10^{-1}	0.00	0.00	7.55×10^{-2}	1.83×10^{-1}	1.07
BFZ146	1.78×10^{-1}	1.16×10^{-2}	6.65×10^{-2}	1.27×10^{-1}	2.11×10^{-1}	4.89×10^{-1}

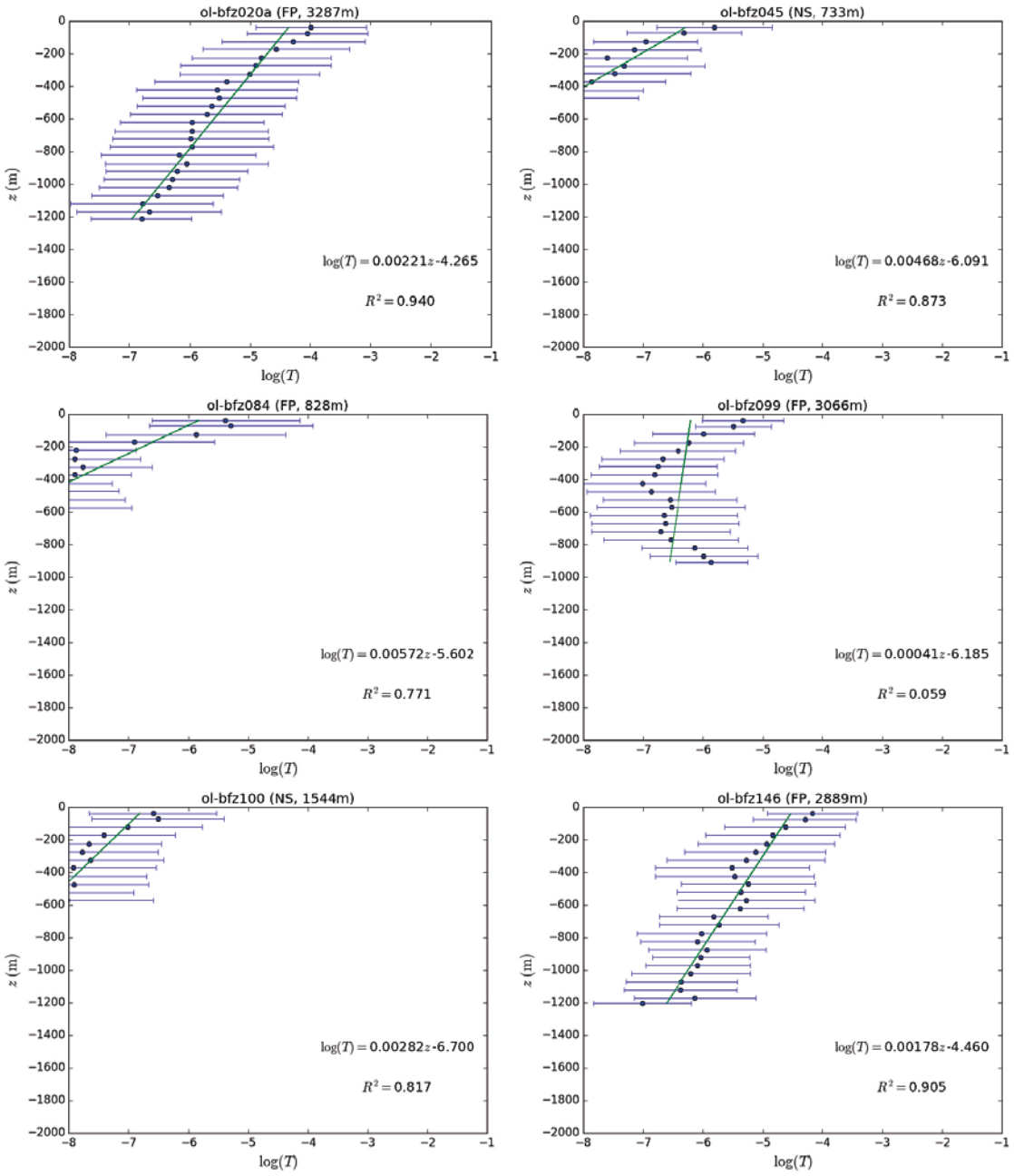

Figure 4-8. *Examples of fits (line) to depth trend in the logarithm of upscaled transmissivity of six fault zones, calculated as the geometric mean transmissivity for grid points within a set of 50 m depth bands. BFZ name, assigned set and strike length is shown in the title of each graph. The horizontal bars show the standard deviation within each depth.*

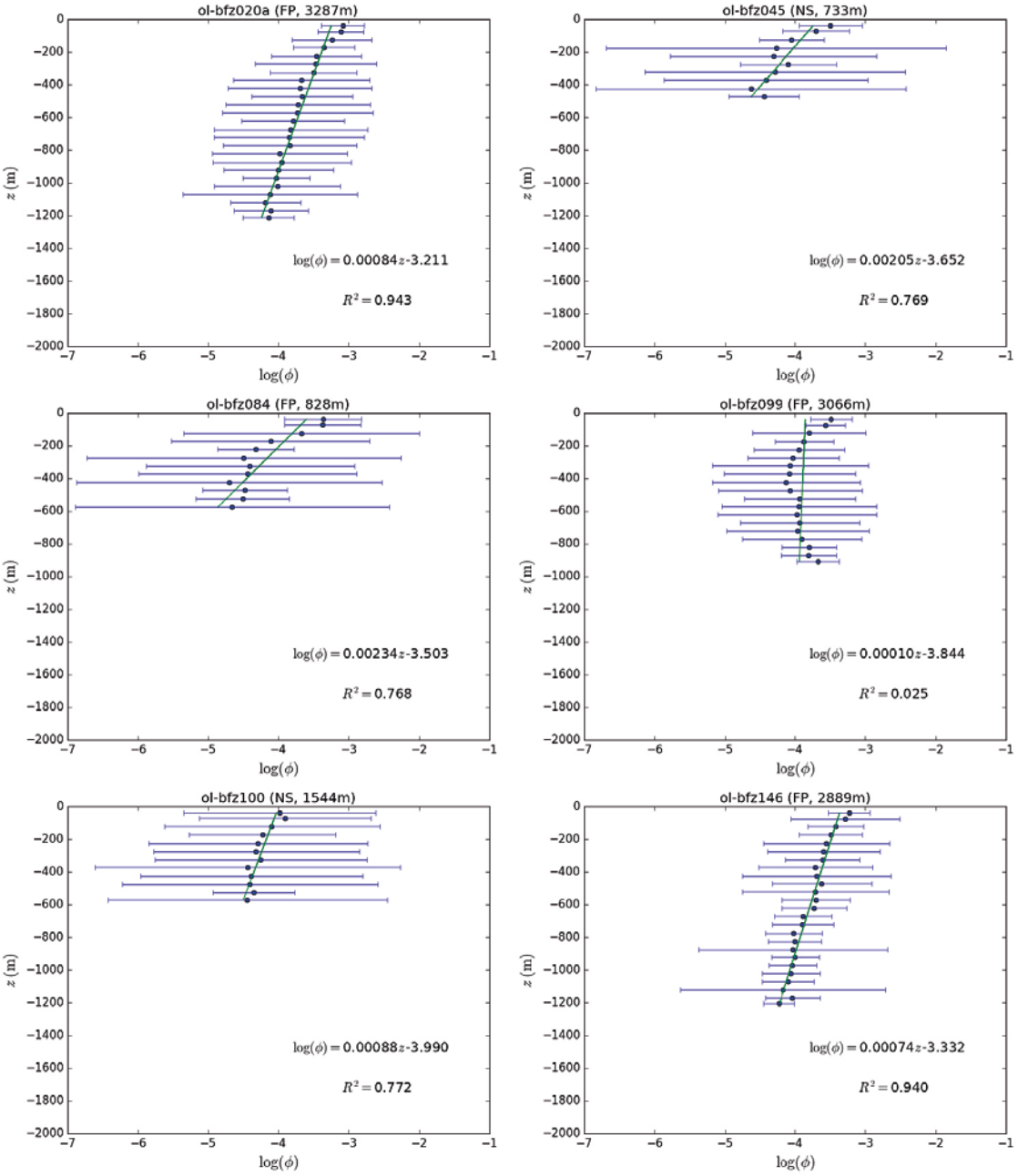

Figure 4-9. *Examples of fits (line) to depth trend in the logarithm of upscaled porosity of six fault zones, calculated as the geometric mean porosity for grid points within a set of 50 m depth bands. BFZ name, assigned set and strike length is shown in the title of each graph. The horizontal bars show the standard deviation within each depth.*

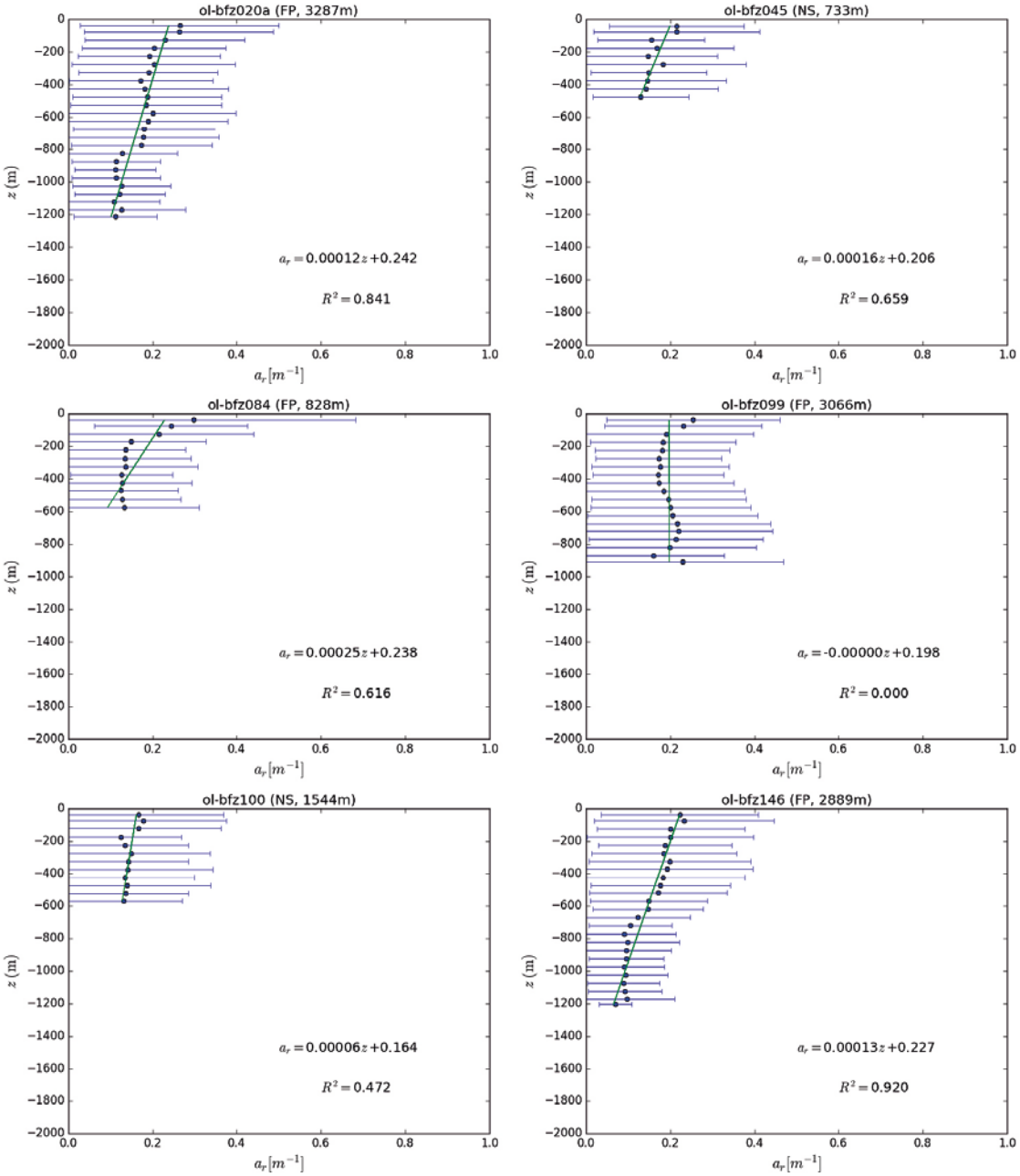

Figure 4-10. *Examples of fits (line) to depth trend in upscaled flow wetted surface of six fault zones, calculated as the arithmetic mean flow wetted surface for grid points within a set of 50 m depth bands. BFZ name, assigned set and strike length is shown in the title of each graph. The horizontal bars show the standard deviation within each depth.*

4.2.1 Island scale flows

This subsection quantifies the fluxes that circulate through the site-scale DFN model, providing a confirmatory analysis of the upscaling methodology for fault zones by comparing simulations using the DFN swarms with those performed using the equivalent mid-plane representations. Consistent with ODFN 2 (Hartley et al. 2012), flows through the island scale are calculated on a series of horizontal planes (spaced every 100 m, but with an extra one at bedrock surface and one at –10 m) with a particular focus on the characterisation area, known here as the island scale. This covers most of the onshore area of Olkiluoto where site drillholes and monitoring are focussed, see Figure 4-11. Total flow rates are then calculated over these planes. The following calculations are performed:

1. Simulation of flows through the Baseline ODFN 3.0 site-scale model including background fractures, **BFZ modelled as fracture swarms**, and stochastic BFZ modelled as planes in ConnectFlow.
2. Simulation of flows through the Baseline ODFN 3.0 site-scale model including background fractures, **BFZ modelled as planes**, and stochastic BFZ modelled as planes in ConnectFlow.
3. Simulations of flows through the upscaled ECPM model equivalent to 1 (above) based on the flow-based transport upscaling underpinning the projection of BFZ properties to the mid-planes. ECPM simulations are also performed in ConnectFlow for the mixed refinement grid.

All simulations are performed as steady-state with the same fixed head boundary conditions appropriate to present-day conditions and neglecting variable density groundwater flow (i.e. only freshwater is included – however, salinity is a factor in the head boundary condition on the sea due to its effect on the seawater density and the resulting difference in pressure). The derivation of the head distribution is derived by calibration process described in Chapter 8 of Hartley et al. (2018).

Figure 4-12 and Figure 4-13 quantify the circulation of groundwater flow in the DFN model and the flow contribution from BFZ for downward and upward flows, respectively. Over this area, the downward and upward flows balance with downward flow at the centre of the island and upward around the shore. Over half the flow is located within the fault zones although the faults only make up a fraction of the fracture area open to flow. The reduction in flow with depth is due partially to decreasing transmissivity due to *in situ* stress and partially to geometric (more gently dipping fractures near surface) and hydraulic (sub-horizontal fractures have higher aperture) anisotropy diverting flow laterally.

When comparing the fault zones modelled as swarms versus an equivalent upscaled mid-plane representation with effective properties, the use of effective property mid-planes sometimes over predict flow by about a factor two at mid-depths. This is assumed to be because of the increased connectivity of simplifying the geometry to continuous planes.

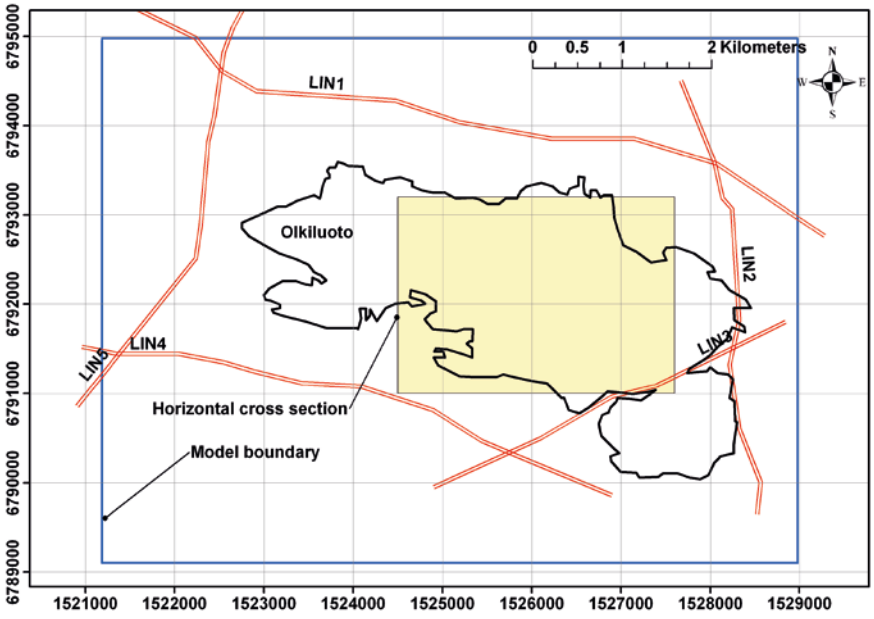

Figure 4-11. *The island scale region used to make flow rate comparison (shaded yellow) and the site-scale boundary shown as a blue box.*

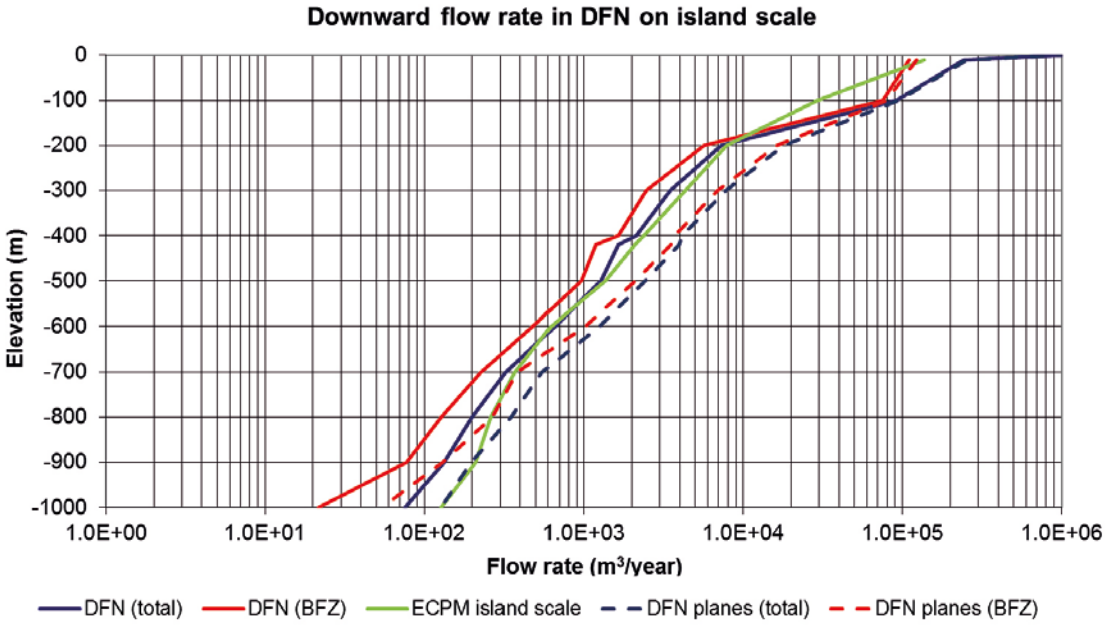

Figure 4-12. *Comparison of downward flow rate in the ODFN 3.0 DFN models over the island scale area when fault zones are modelled as swarms (solid) or planes (dashed). Total flow rates (blue) and those associated with faults (red) are shown. Total flows for an ECPM model (green) implemented in ConnectFlow are also compared.*

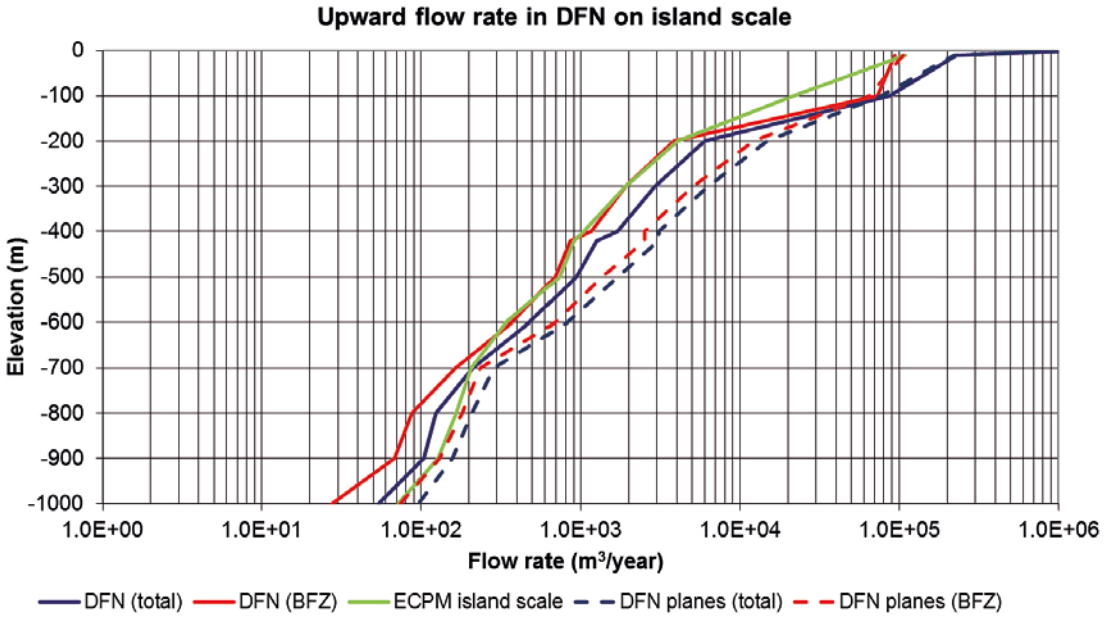

Figure 4-13. *Comparison of upward flow rate in the ODFN 3.0 DFN models over the island scale area when fault zones are modelled as swarms (solid) or planes (dashed). Total flow rates (blue) and those associated with faults (red) are shown. Total flows for an ECPM model (green) implemented in ConnectFlow are also compared.*

In this subsection pathline calculations are performed for the six significant fault zones at Olkiluoto upscaled previously in this chapter, namely BFZ020a, BFZ045, BFZ084, BFZ099, BFZ100, and BFZ146. The site-scale flow solutions (see Subsection 4.2.2) are used to consider the release of 5 000 particles distributed randomly across these six faults with transport properties of path length, travel time and flow related transport resistance compared. Particle tracks based on the full ODFN 3.0 model with faults represented as fracture swarms are compared to those represented as mid-planes with equivalent properties, to assess consistency between representations.

Figure 4-14 and Figure 4-15 illustrate the particle tracks and end points for particles released within BFZ020a for both models considered. The pathlines and exit locations are consistent between the two models, and the random distribution of start points across the fault zones is clearly observed. In addition, the more tortuous pathlines when representing the faults as swarms of individual fractures as opposed to mid-planes is apparent. Corresponding particle tracking results for release in BFZ099 are shown in Figure 4-16 and Figure 4-17 respectively.

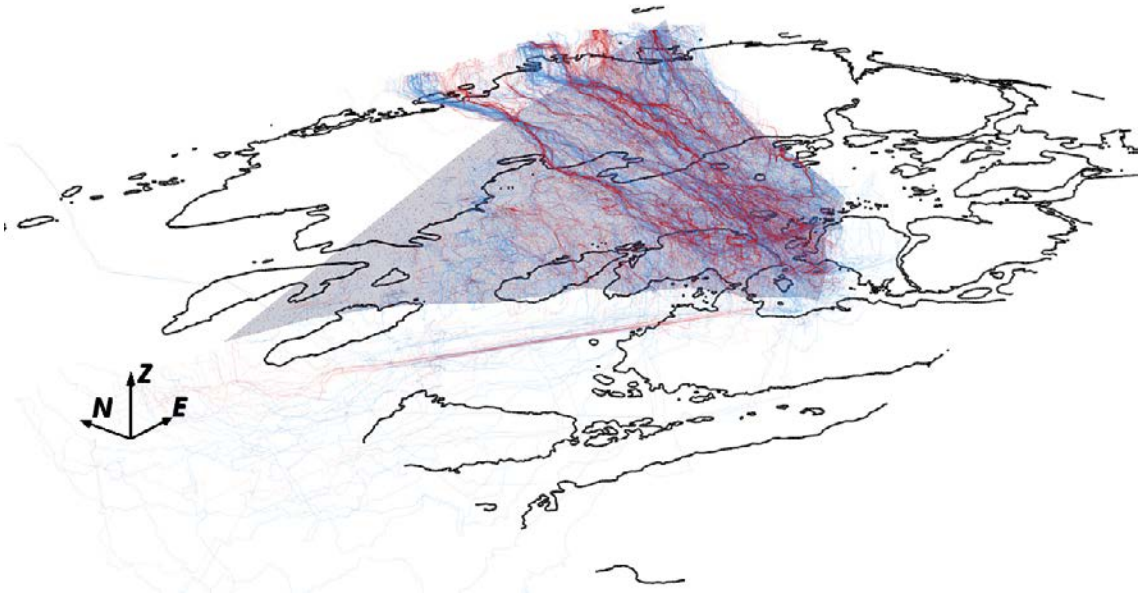

Figure 4-14. *Particle tracks released from BFZ020A within the ODFN 3.0 model for (i) fault zones represented as fracture swarms (red); and (ii) faults represented as equivalent mid-planes (blue). The fault mid-plane is also shown semi-transparent.*

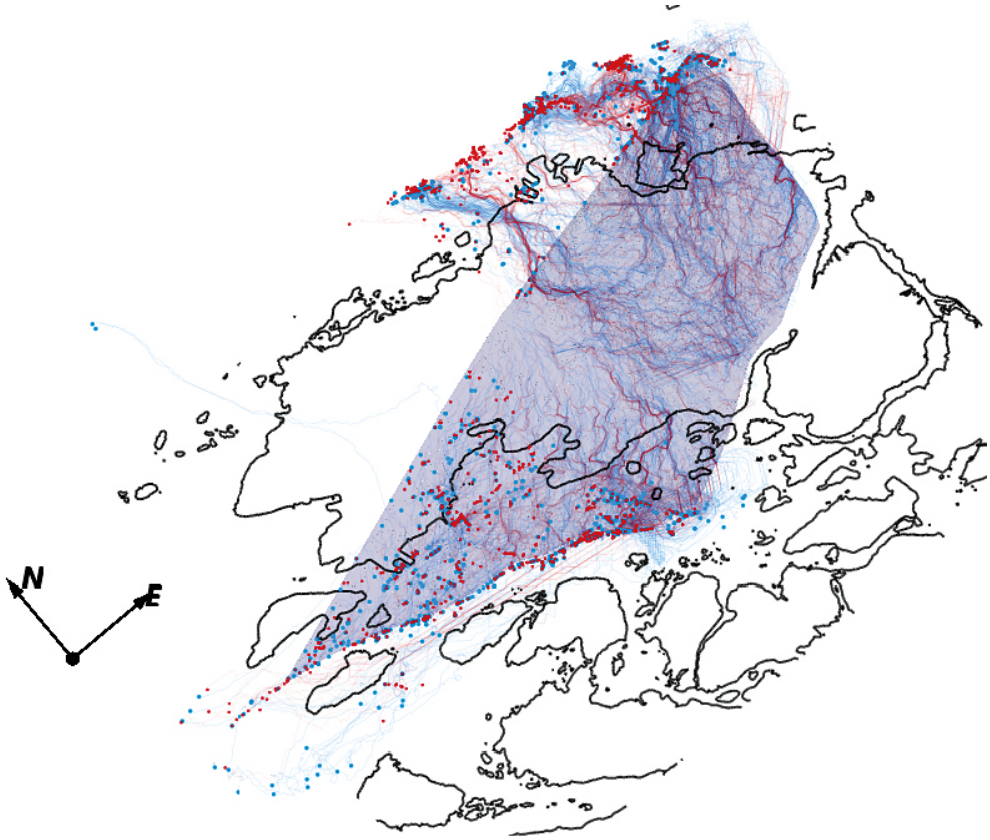

Figure 4-15. *Particle end points released from BFZ020A within the ODFN 3.0 model for (i) fault zones represented as fracture swarms (red); and (ii) faults represented as equivalent mid-planes (blue). The fault mid-plane is also shown semi-transparent.*

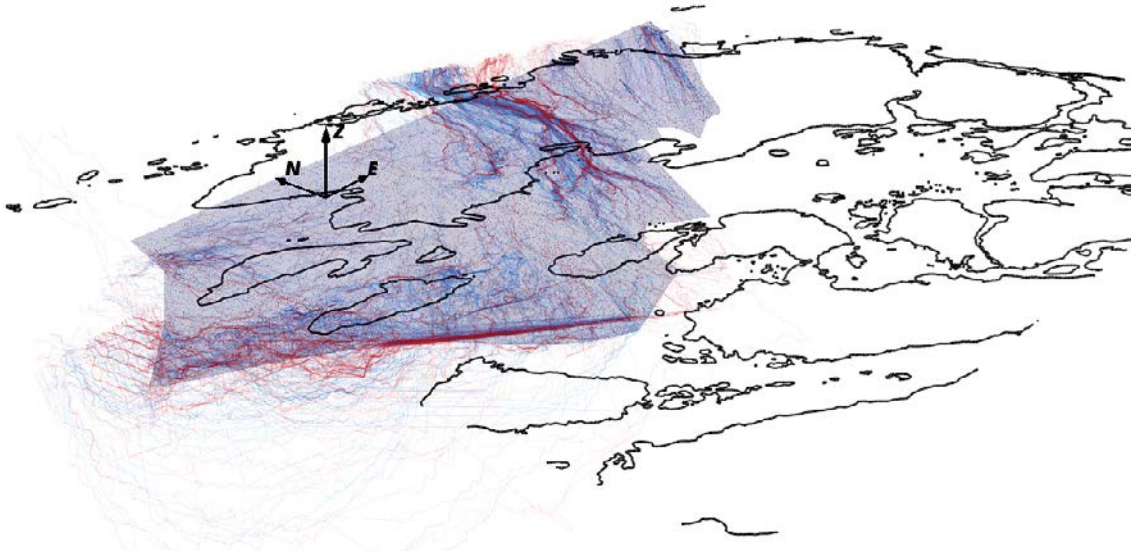

Figure 4-16. *Particle tracks released from BFZ099 within the ODFN 3.0 model for (i) fault zones represented as fracture swarms (red); and (ii) faults represented as equivalent mid-planes (blue). The fault mid-plane is also shown semi-transparent.*

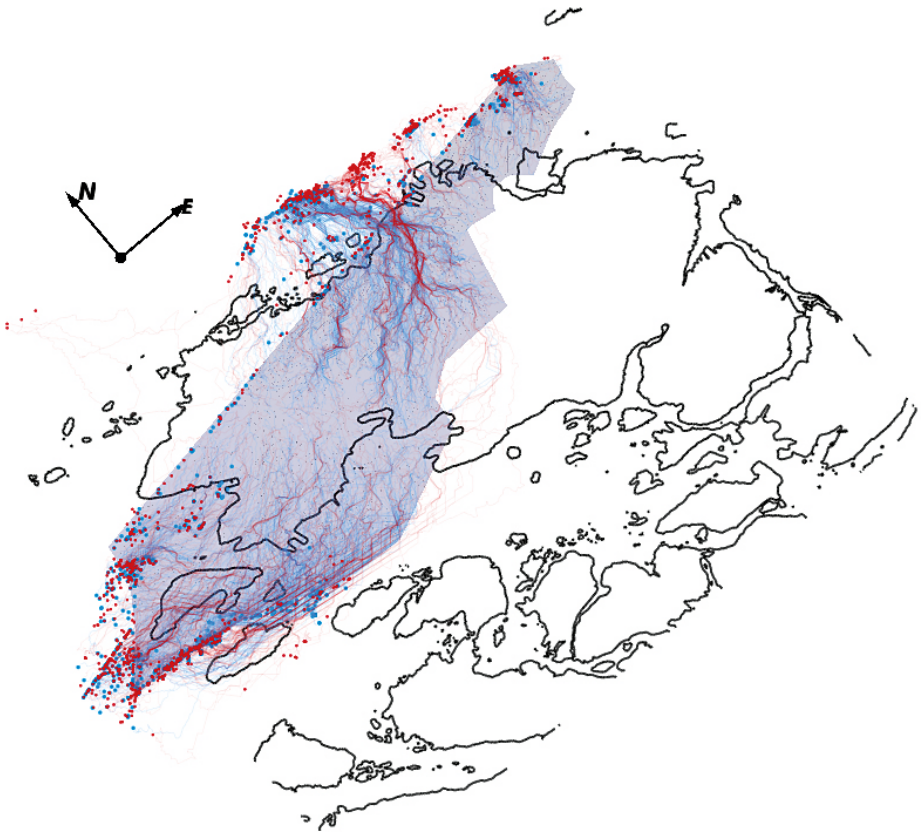

Figure 4-17. *Particle end points released from BFZ0099 within the ODFN 3.0 model for (i) fault zones represented as fracture swarms (red); and (ii) faults represented as equivalent mid-planes (blue). The fault mid-plane is also shown semi-transparent.*

Based on the 5 000 particle tracks simulated across the two models, cumulative distribution functions are generated for transport properties such as travel time, path length and flow related transport resistance as shown in Figure 4-18, Figure 4-19 and Figure 4-20 respectively. It is noteworthy that a number of particle start points within the fault zones (which are randomly sampled) are located close to the subsequent exist locations within the model and as such the corresponding path lengths are short. Consistent with the findings in Subsection 4.2.1, when comparing the fault zones modelled as fracture swarms versus an upscaled mid-plane with effective properties, the use of effective properties on the fault mid-planes results in an under-prediction of travel times and flow related transport resistance by about a factor two. This is likely due to the increased connectivity and reduced tortuosity of the flow paths when simplifying the geometry to continuous planes.

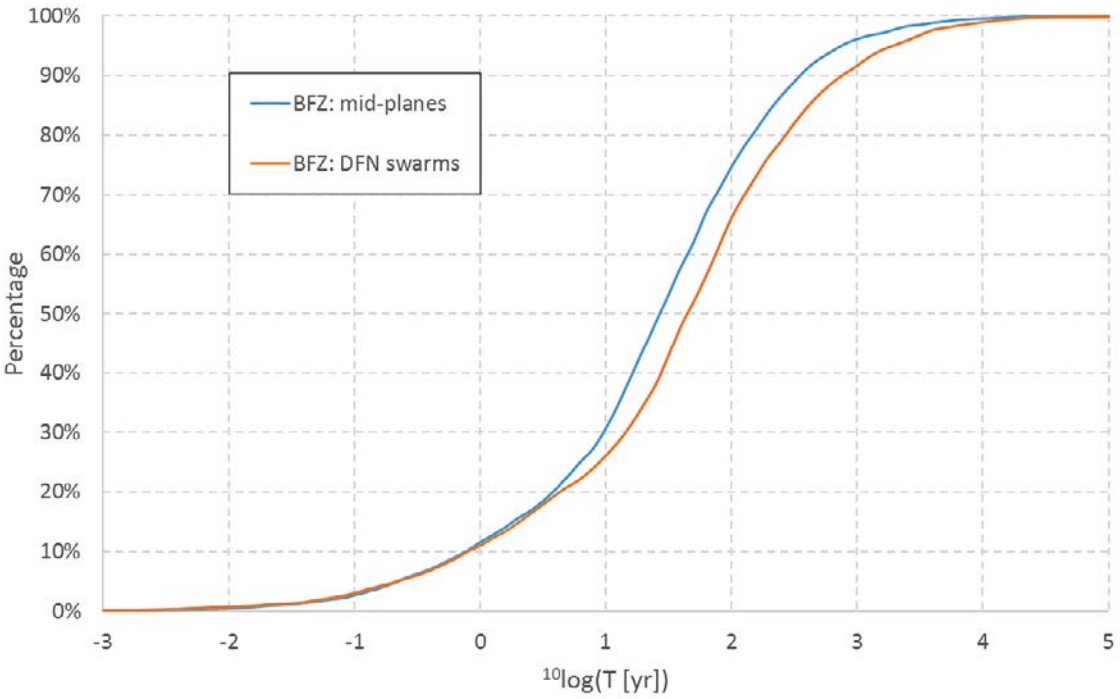

Figure 4-18. *CDF of travel time, T, for 5 000 particle tracks with start points distributed randomly across BFZ020a, BFZ045, BFZ084, BFZ099, BFZ100 and BFZ146. Results are shown for the fault zones modelled as DFN swarms (red) as well as the upscaled equivalent plane properties derived in Section 4.1.2 (blue).*

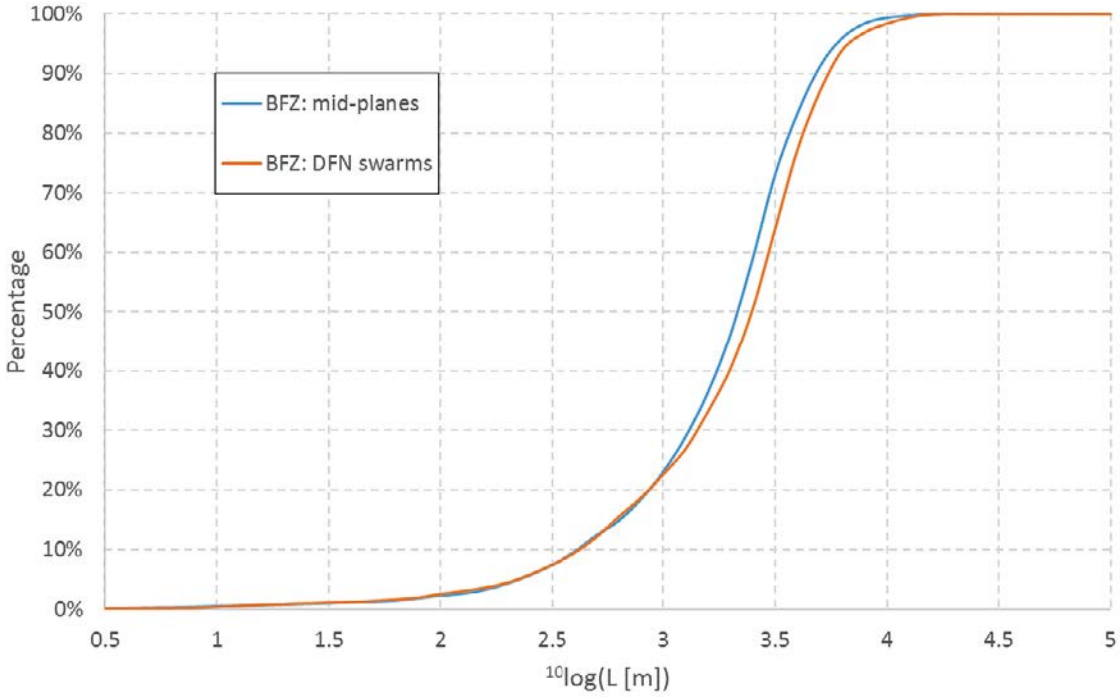

Figure 4-19. *CDF of path length, L, for 5 000 particle tracks with start points distributed randomly across BFZ020a, BFZ045, BFZ084, BFZ099, BFZ100 and BFZ146. Results are shown for the fault zones modelled as DFN swarms (red) as well as the upscaled equivalent plane properties derived in Section 4.1.2 (blue).*

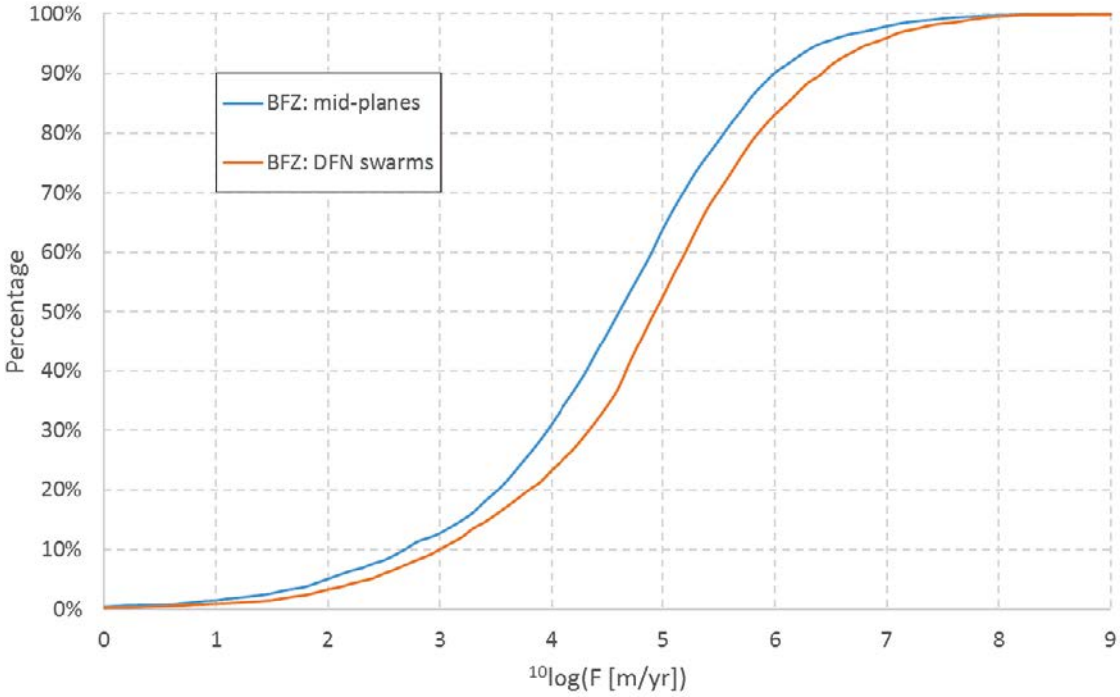

Figure 4-20. *CDF of flow-related transport resistance, F, for 5 000 particle tracks with start points distributed randomly across BFZ020a, BFZ045, BFZ084, BFZ099, BFZ100 and BFZ146. Results are shown for the fault zones modelled as DFN swarms (red) as well as the upscaled equivalent plane properties derived in Section 4.1.2 (blue).*

5 Geostatistical models of planar BFZ

The upscaling and projection of fault zone properties as outlined in Chapters 3 and 4 can be a time-consuming process, and the resulting structures require characterisation using hard data. To understand the statistical uncertainty associated with the upscaled faults, a number of different stochastic realisations are required, and therefore a less demanding method for generating and attributing associated properties to the fault zone mid-planes would be beneficial. In this section a methodology for efficiently generating a series of stochastic realisations of the fault zones is described.

Using the upscaled and projected results as a basis, statistical models describing the spatial variation and correlation of transport and flow properties on a fault zone can be generated. The statistical models take the form of variograms, which describe the extent to which the values that a property takes at any two points in space are expected to differ. These variograms can then be used to generate an expected result through Kriging, or a range of stochastic realisations using Gaussian simulation.

Section 5.1 provides an introduction to geostatistical analysis, focusing on the selected modelling tool for analysis and generation of multiple realisations of the fault zones. Attention is then directed towards the application of the geostatistical method and the performance of Gaussian simulations. In Section 5.2, two different approaches are presented:

- The geostatistical method is conditioned by the available measured data. This approach is general and utilises only the measured data for the generation of the variograms. Through this procedure variograms from well characterised fault zones can be used, by analogy, to generate estimates on fault zones where measured data is sparse.
- The geostatistical method is conditioned by the projected upscaled properties obtained through the methodology described in Section 4. In this approach, variograms are generated for each fault zone based on all of the upscaled data points. The geostatistical method is then conditioned on a randomly selected subset (typical c. 50) data points from the upscaled fault zone. This Gaussian simulation provides a very efficient methodology for generating stochastic realisations for all of the upscaled faults.

For the demonstration of both approaches, fault zone BFZ020a is considered.

5.1 The geostatistical approach for simulating BFZ

In this study, the geostatistical analysis is performed using the Stanford Geostatistical Modelling Software (SGeMS) (Remy et al. 2011). SGeMS is an open-source software package for solving problems involving spatially related variables, providing algorithms for multiple point statistics. It is a user friendly suite widely used in industry and academia for the statistical analysis of any real data, the generation of appropriate variograms, and the utilisation of any of the available simulation kits.

The implementation of a sequential Gaussian simulation is provided through the (SGSIM) algorithm. SGSIM generates a stochastic realisation of potential values that a property may take, using a process which takes the following steps:

- Define a random sequence of grid points onto which the estimate is to be generated.
- At each point in this sequence, generate a point value as follows:
  - Use the provided real data and all previously calculated point values to generate a kriging estimate at the point, with a normally distributed error.
  - Take a random sample from the normal distribution about the kriging estimate as the point value at the current point.

As the algorithm completes the grid, each subsequent point becomes more and more constrained. The stochasticity arises in the definition of the random path and sampling from the Kriging distribution. Many stochastic realisations can be made with the same inputs by beginning with a different random seed for each realisation.

A range of inputs are required by SGeMS to specify how it will generate a stochastic realisation of a fault zone using SGSIM. The inputs include:

- **A grid** or region of points onto which the estimate will be generated.
- A **real data** set – either measured experimentally or randomly sampled from a well-defined model, and whether to match the simulated distribution to a target histogram (usually based on the real data).
- A **variogram**, based either on measured data or a well-defined model, specifying the extent to which property values are correlated in each spatial direction. The generation of a variogram is explained under Subsection 5.1.1.
- A choice of the **Kriging type**:
  - Simple Kriging, assumes stationarity in the mean of the variable.
  - Ordinary Kriging, allows for the mean to vary locally.
- For each point in the grid, how to conduct the **conditioning point search**:
  - A limit on the maximum number to use.
  - The size and orientation of a 3D search ellipsoid, which may be anisotropic or spherical, within which to search for points.

The hard data used to condition the Gaussian simulation may be either real measured data, or a random sample of points from the upscaled properties. Both options have benefits and drawbacks: Measured data may be scarce and clustered, but will directly represent the data underpinning the description of the fault zone. A random sample from the upscaling will guarantee an abundance of data distributed across the spatial extents of the zone, allowing both long- and short-scale trends to be captured, but does not directly honour the measured data (other than through calibration of the underlying DFN model).

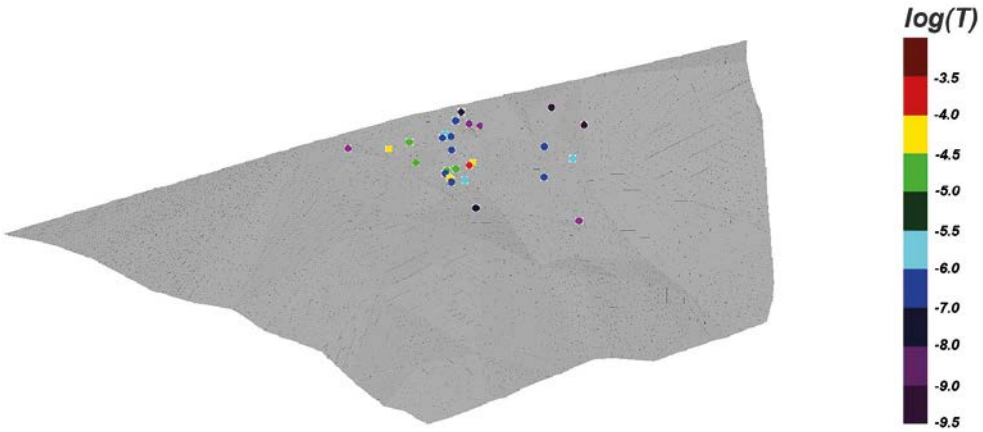

Figure 5-1. *The measured locations for transmissivity (from drillhole intercepts) for fault zone BFZ020a.*

5.1.1 Generation of variograms

Given a set of data points, an experimental variogram is defined by specifying:

- The size of the spatial step between distances at which data values will be compared, termed the lag distance (as well as the lag tolerance, which is effectively the width of the spatial bin).
- The maximum range of the variogram, defined as the product of lag distance and number of lags. It should be set to the maximum distance over which a spatial correlation might be expected, typically around half the size of the spatial spread of the data. This is a distinct quantity from the "variogram range" discussed below, which is a property of the variogram fit.
- The direction of the variogram, and the angular tolerance.

The definition of multiple variograms with different directions can be helpful to distinguish between horizontal and vertical, east-west and north-south, or major and minor axis variations, for example, and to highlight instances where a property may vary anisotropically.

An experimental variogram analysis then requires a functional fit to guarantee a correct and tractable form for the Gaussian simulation routine. SGeMS allows the user to fit standard variogram forms (exponential, spherical and Gaussian) to the experimental variogram. The complete definition of the variogram fit requires the definition of the:

- **Sill:** The size of the maximum variance between two correlated points, as measured by the experimental variogram.
- **Nugget:** The size of the essentially random noise or measurement error that causes the appearance of a non-zero variance at zero or very small distance.
- **Form:** of the variogram (exponential, spherical or Gaussian).
- **Variogram range**: The distance over which the variogram first reaches the sill in each of its major, medium and minor directions, as inferred from the experimental variogram. These can be different in the case of an anisotropic experimental variogram (example in Figure 5-3). Pairs of points that are separated by more than the range are then assumed not to be spatially correlated.
- **Fit direction:** The orientation of the major, medium and minor axes of the fit.

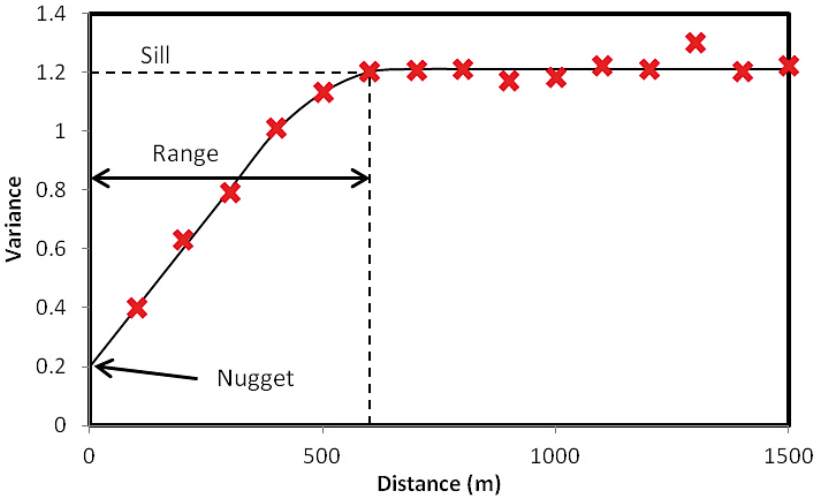

Figure 5-2. *Schematic variogram illustrating the Sill, Nugget and Range. In this example the sill is 1.2 with a nugget of 0.2, and a range of 600 m.*

To inform the selection of the variogram, two factors should be considered. Firstly it is advised to fit more closely to the shorter range data as property correlations between data points are expected to be stronger at shorter length scales. Secondly, SGeMS provides the number of data pairs which lie within each lag and thus define the value of the variance; a higher number also indicates a better defined point.

The example shown in Figure 5-3 illustrates a series of experimental variograms based on the measured data points in Figure 5-1. The figures show one omnidirectional variogram (where the angular tolerance is set to include all directions), one North-South oriented, and one East-West oriented. The North-South variogram has a shorter range than the East-West (that is, it reaches the sill value earlier), possibly due to the spatial spread of data being smaller in the North-South direction compared to the East-West. The functional fit to the variogram data uses the Gaussian form, and has the following parameters:

- **Sill**: 5
- **Nugget**: 0
- **NS range**: 800 m
- **EW range**: 1 000 m
- **Major axis:** 90°

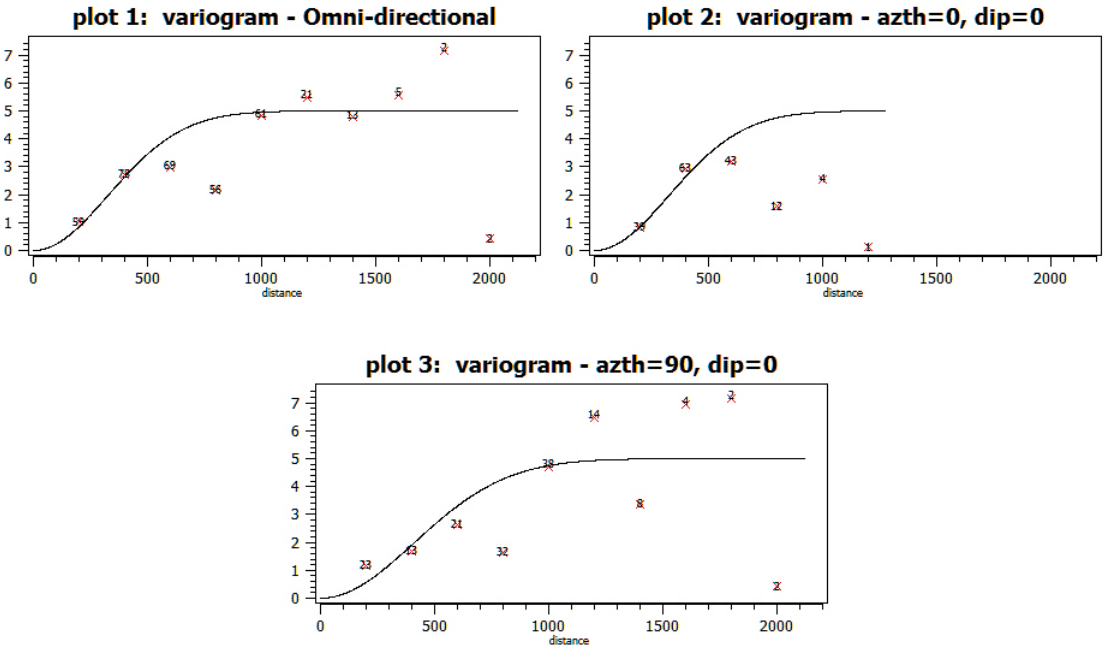

Figure 5-3. *Output from SGeMS: Experimental variograms of the measured transmissivity data for fault zone BFZ020a. The top left chart is an omnidirectional variogram, the top right chart is oriented on the minor axis of the fault, and the bottom chart is oriented on the major axis of the fault. The resulting variogram is quite noisy due to the high variability in the measured data.*

5.2 Example results for Olkiluoto

In this section the geostatistical analysis and Gaussian simulation of fault zone BFZ020a is considered with the aid of SGeMS. Restriction to BFZ020a for prototyping this methodology is based on the fault being a significant, large zone with a substantial amount of characterisation data available. A more detailed analysis could further proceed and consider BFZ045, BFZ084, BFZ099, BFZ100 and BFZ146, for which borehole intersects/measured data are available, and cover a range of fault zone characteristics such as size, shape and orientation.

In order to simplify the geostatistical approach, the fault zone is first reduced to a two-dimensional plane by rotating it such that the surface normal is in the vertical direction, and then equating the vertical coordinate of each point to the same constant. This ensures that the simulation need only search for conditioning points in two-dimensional space.

The analysis aims to be general and demonstrate the applicability of the method for the cases where:

- Sufficient experimental data are available for the generation of stochastic realisations (see Subsection 5.2.1).
- In the absence of sufficient experimental data, the projected upscaled properties (see Section 4) are used to generate stochastic realisations based on a randomly selected subset of the data.

5.2.1 Geostatistics based on the measured data

Using the measured data and the variograms presented in Figure 5-3, the Gaussian simulation routine in SGeMS produces the spatial distribution for log(transmissivity) shown in Figure 5-4 for four realisations of the Gaussian simulation. The simulation used input data described by the following:

- **Grid:** Consisting of 4 898 points corresponding to the centroids of the triangulated elements of BFZ020a.
- **Real data:** as shown in Figure 5-1, matching histogram of the resulting distribution to the real data histogram, with no extrapolation outside the range of the real data.
- **Variogram:** as illustrated by Figure 5-3.
- **Kriging type:** Simple Kriging.
- **Conditioning point search:** 4 000 m radius isotropic search.

The drillhole intercepts with fault zone BFZ020a are relatively clustered (see Figure 5-1) providing a high-density of measurements toward the centre of the fault, which are honoured in each realisation. As such, the Gaussian simulation of transmissivity in this area and the surrounding region is well constrained, with little variation between realisations. In locations further from this data, the simulated transmissivities are more variable due to the lack of data to constrain the Gaussian simulation.

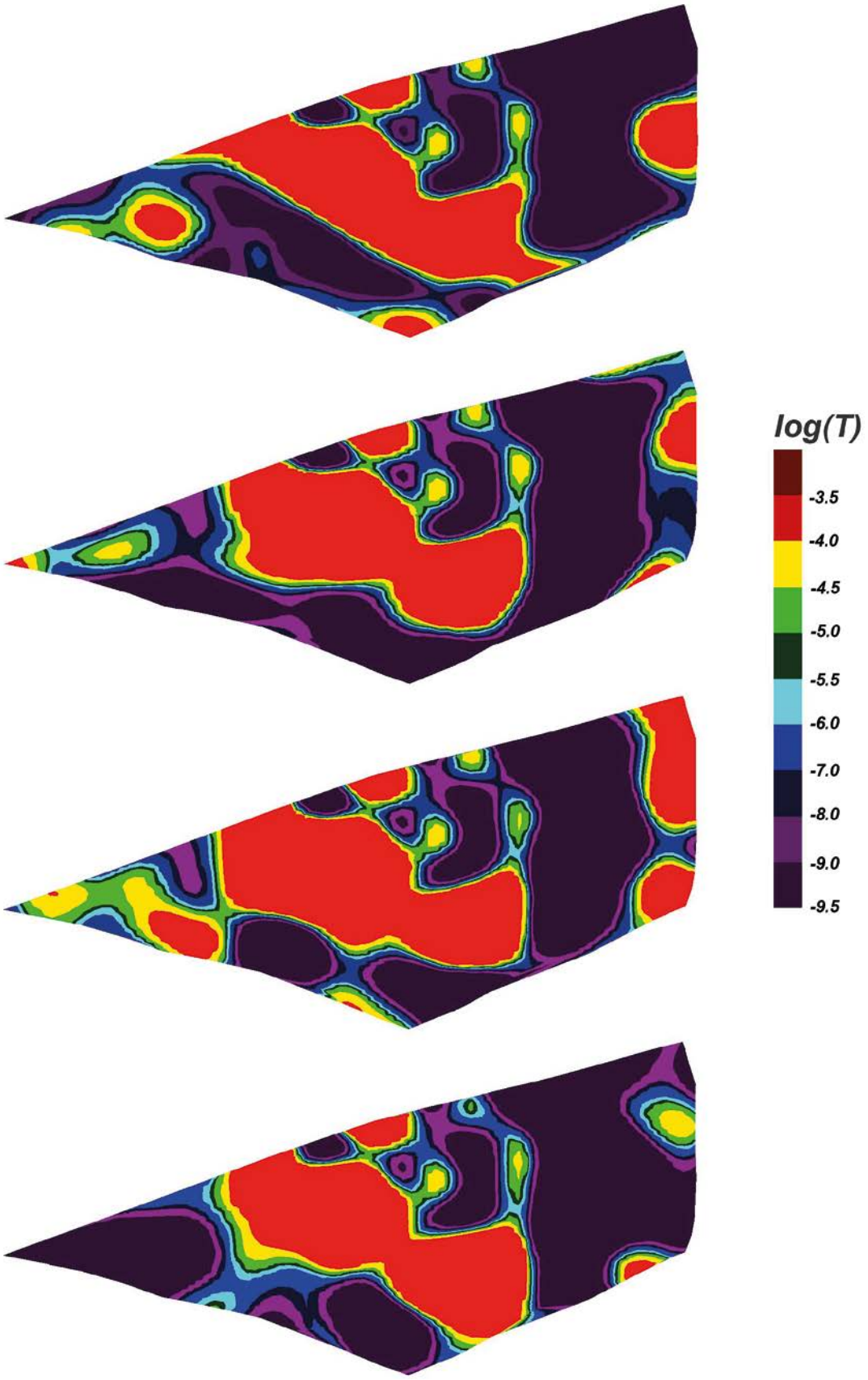

Figure 5-4. *Four realisations of log(transmissivity) from Gaussian simulation using the measured data points located towards the centre of the BFZ (see Figure 5-1).*

5.2.2 Geostatistics based on the upscaled fault zones

For fault zones with a scarcity of measured data, or with data not adequately distributed across the fault, a geostatistical approach can be based on the upscaled mid-plane properties of the fault zone (as calculated in Section 4). Here, a random sample from the complete suite of points in the upscaled fault zone are used as a set of conditioning points for generation of multiple Gaussian simulation realisations from a single underlying DFN realisation. If the number of random points is chosen appropriately this should, in addition, reproduce general trends in the underlying data (if the number of points is too high then the model will be over constrained). For the purposes of our investigation 50 points are used, as shown in Figure 5-5, and randomly selected out of the underlying 4 898 points taken as the centroids of the BFZ020a triangulated elements. Histograms of the logarithms of transmissivity and porosity, for the full set of points, as well as for the 50 randomly selected points, are shown in Figure 5-6 though Figure 5-9 respectively.

Geostatistical methods for continuous variables are optimal when the data are normally distributed. The histogram for transmissivity data is approximately normal for the bulk of the upscaled points, although some distortion is seen at high transmissivities due to the truncation applied in the upscaling methodology (10^{-3} m^2/s). The normal distribution is a suitable distribution for describing the upscaled values for porosity.

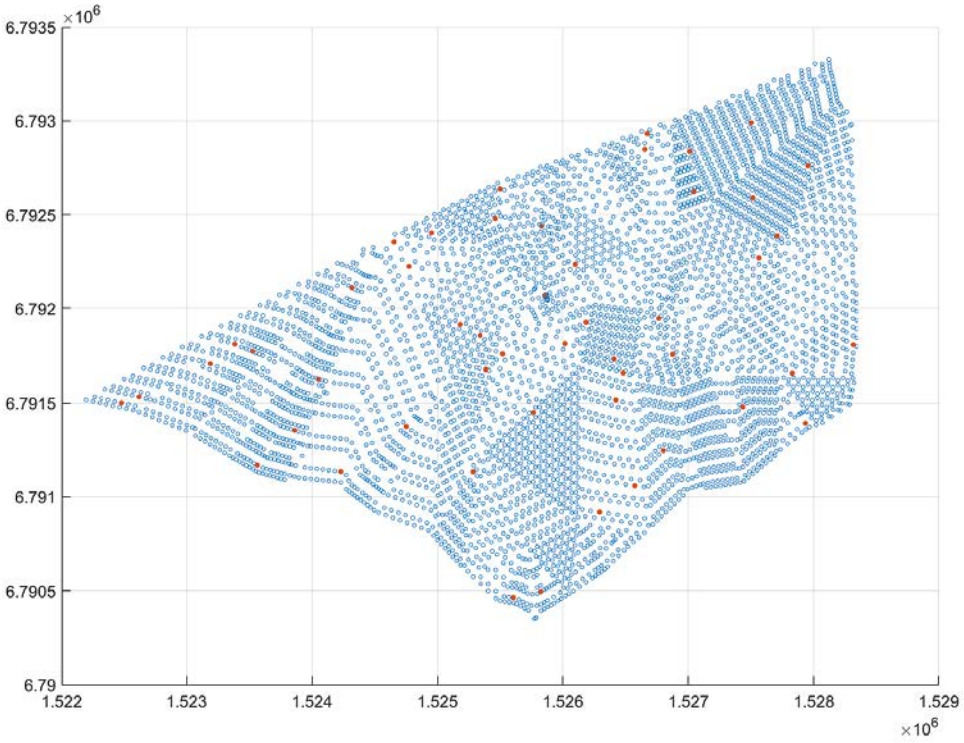

Figure 5-5. *The locations of the 50 randomly sampled points (red) from the upscaling projection as used in the geostatistical methodology, and the remaining 4 848 points which are not sampled (blue).*

Variograms for transmissivity and porosity are generated from all of the upscaled fault zone property data (i.e. all 4 898 points are utilised for BFZ020a), as shown in Figure 5-10 and Figure 5-11 respectively. For both cases an omnidirectional variogram (with an angular tolerance of 90 degrees and a very large bandwidth) and four directional variograms at 0, 45, 90 and 135 degrees, each with an angular tolerance of 22.5 degrees and a bandwidth of 100 m have been generated. The number and spacing of the computed lags (i.e. spatial bins) are chosen in order to capture the range over which data is expected to be correlated. In this case, the lag number has been set to 15, whilst a nominal lag spacing of 40 m and a lag tolerance of 20 m is being used for both sets of data. This choice of lag number and spacing gives a range of 600 m (i.e. 15×40 m).

The variogram fit used for the transmissivity is exponential with the following properties:

- **Sill**: 0.75
- **Nugget**: 0.1
- **Major range**: 600 m
- **Minor range**: 600 m
- **Major axis:** 0°

For the porosity data, an exponential fit is again used for the variogram based on the following properties:

- **Sill**: 0.1
- **Nugget**: 0.03
- **Major range**: 600 m
- **Minor range**: 600 m
- **Major axis:** 0°.

The major and minor range represent the maximum distance in each direction over which two data points can be considered to be correlated. The porosity and the transmissivity are likely to be correlated to each other, so it is a reasonable assumption that if (as shown in the porosity variograms at 0° and 135°) the porosity variogram has some correlation out to 600 m in both major and minor directions then this range will be shared by the transmissivity.

The specification of directionality (including omnidirectional) gives more information to the geostatistician about the variation along the different axes. These variograms show that the correlation is almost independent of direction, with showing slightly lower variance in the 45° and 90° directions. A strong anisotropy would indicate that correlation is perhaps guided by a physical feature in the geosphere, but this is not the case here.

Stochastic realisations obtained for transmissivity and porosity through Gaussian simulations using Ordinary Kriging are shown in Figure 5-12 and Figure 5-13 respectively. Simulations are based on conditioning to the upscaled transmissivity and porosity values at the randomly selected 50 upscaled points, with each realisation honouring these point values, and based on the variograms described above and shown in Figure 5-10 and Figure 5-11. The realisations obtained for both sets of data are in a very good agreement with the upscaled properties with simulations reflecting the underlying global trends whilst providing adequate local-scale variability.

It is noted that the stochastic realisations calculated for the porosity do not fully capture the thin layer of high porosity located towards the top of BFZ020a. It is anticipated that this could be easily resolved with the inclusion of a few additional conditioning points in this region.

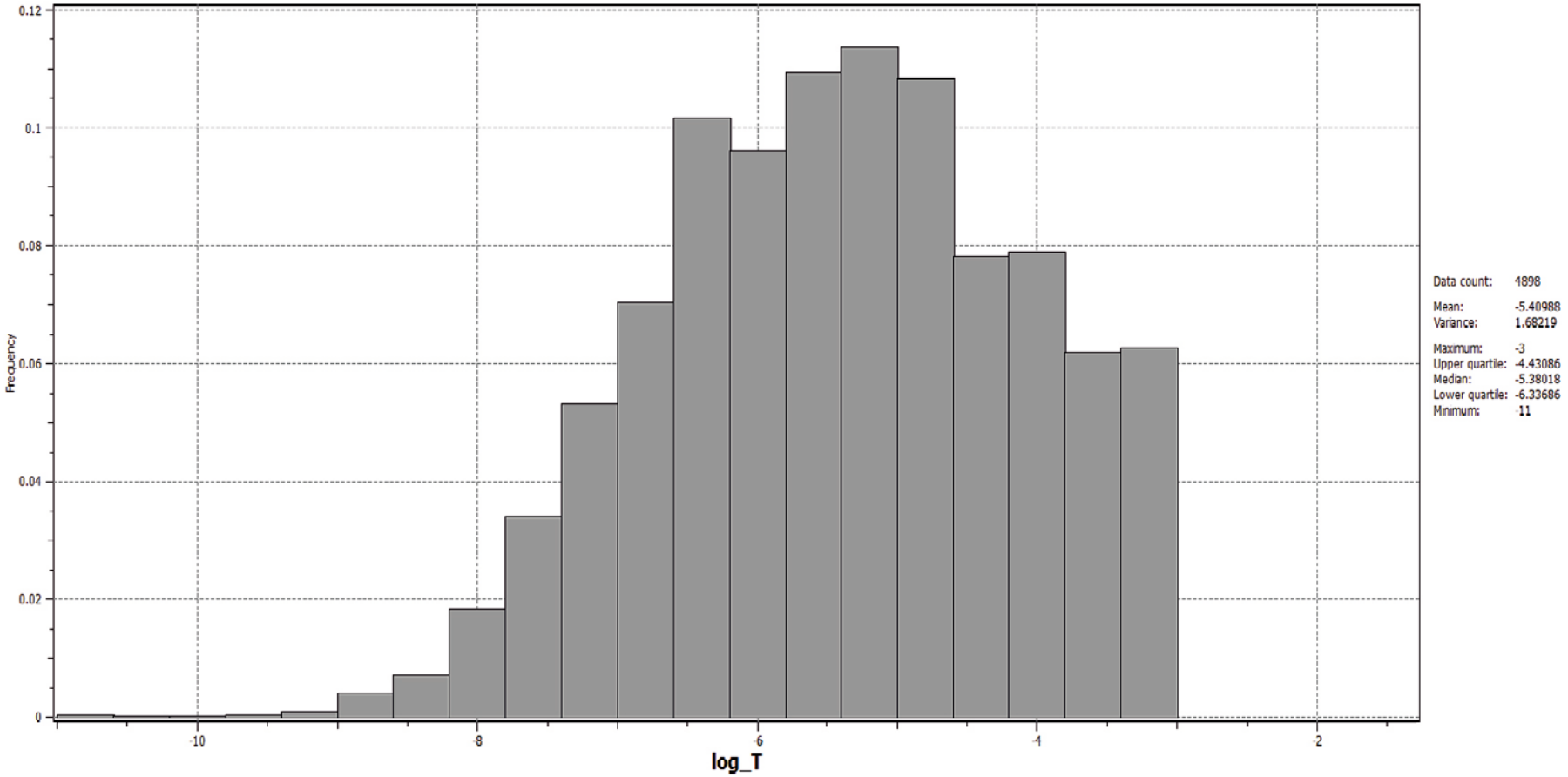

Figure 5-6. *Histogram obtained* from SGeMS, *portraying the distribution of the upscaled transmissivity values obtained from all the nodes of BFZ020A.*

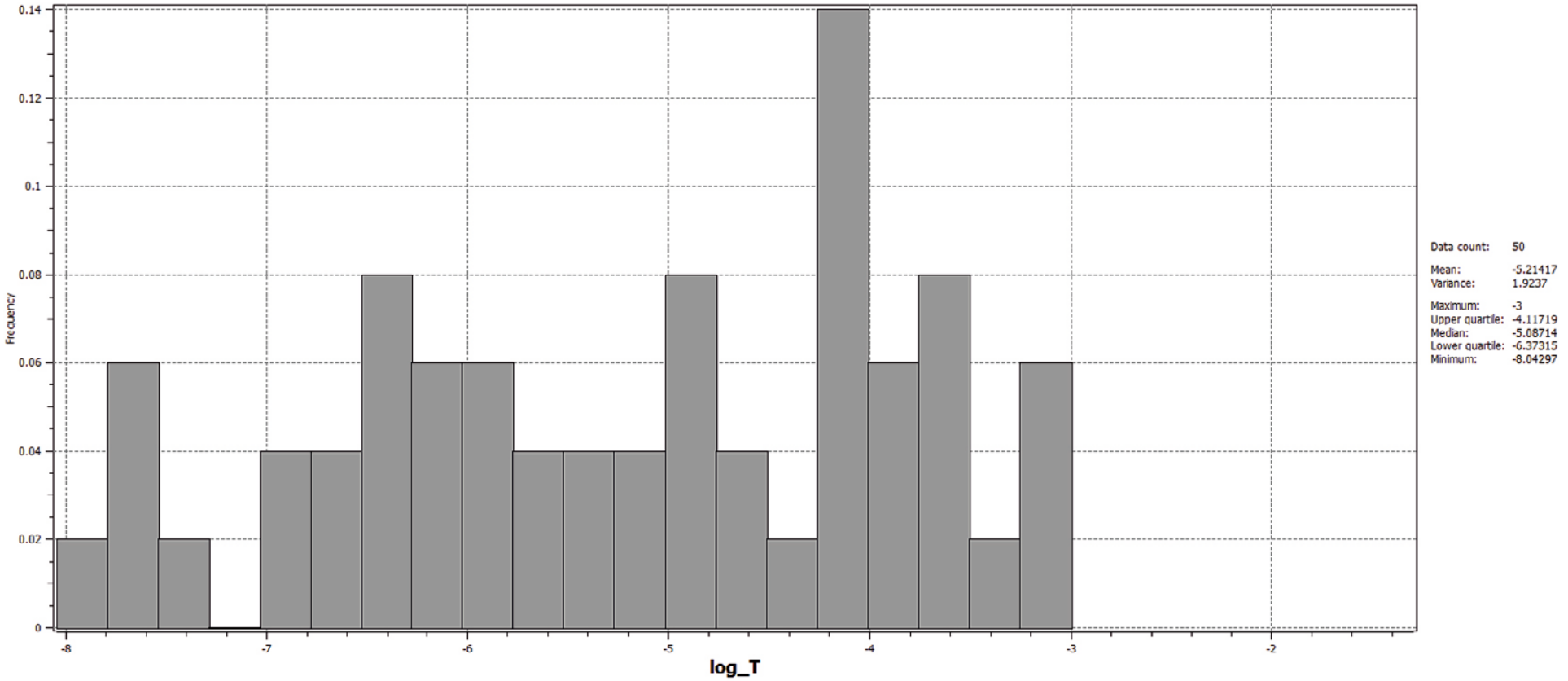

Figure 5-7. *Histogram obtained* from SGeMS, *portraying the distribution of the upscaled transmissivity values of 50 randomly selected points of BFZ020A.*

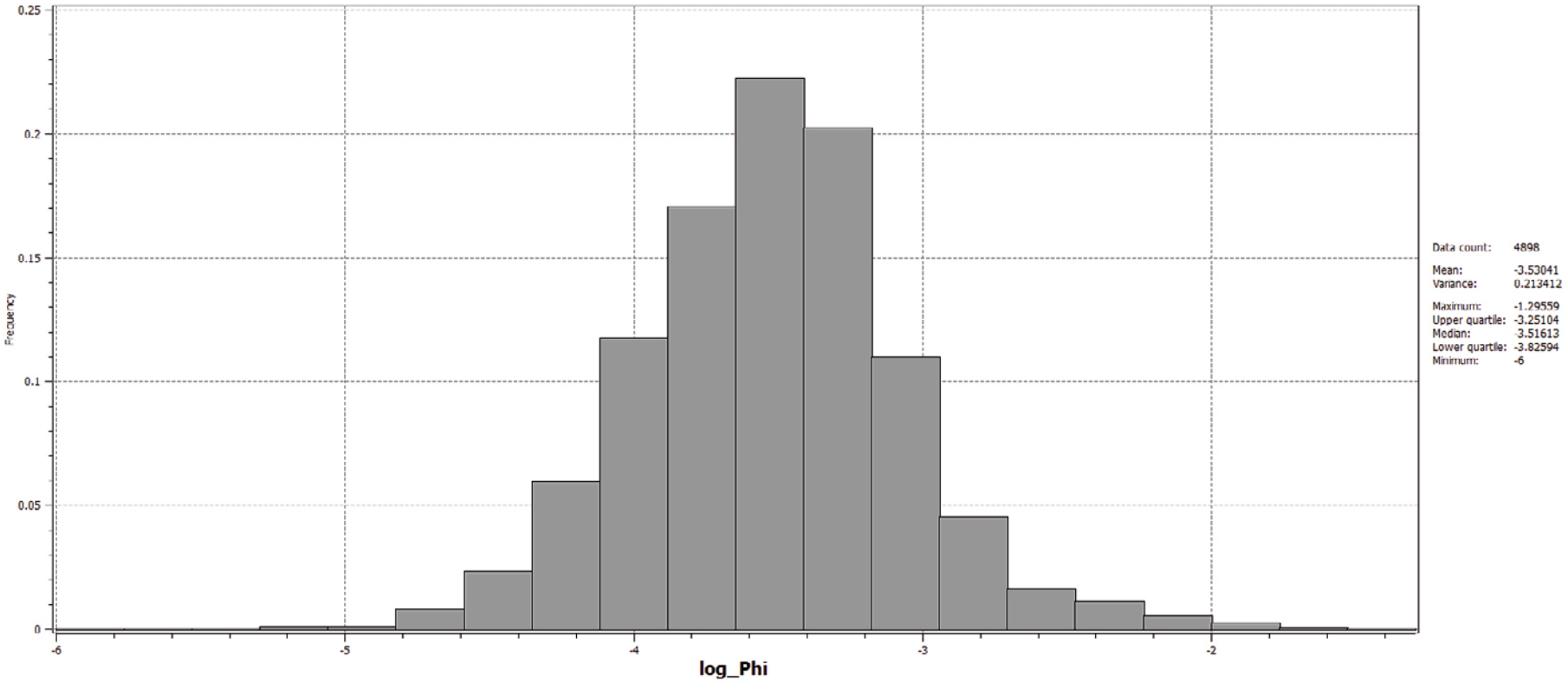

Figure 5-8. *Histogram obtained* from SGeMS, *portraying the distribution of the upscaled porosity values obtained from all the nodes of BFZ020A.*

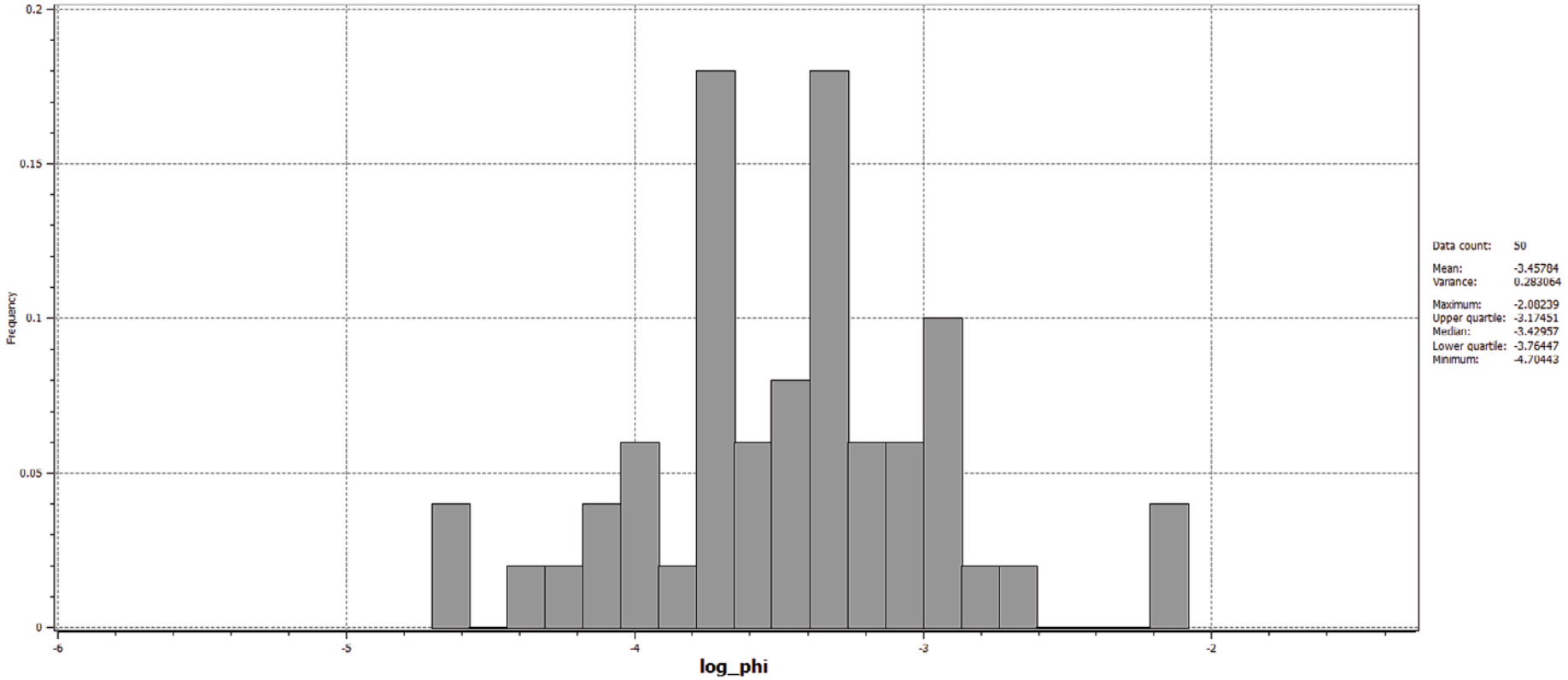

Figure 5-9. *Histogram as obtained* from SGeMS, *portraying the distribution of the upscaled porosity values of 50 randomly selected points of BFZ020A.*

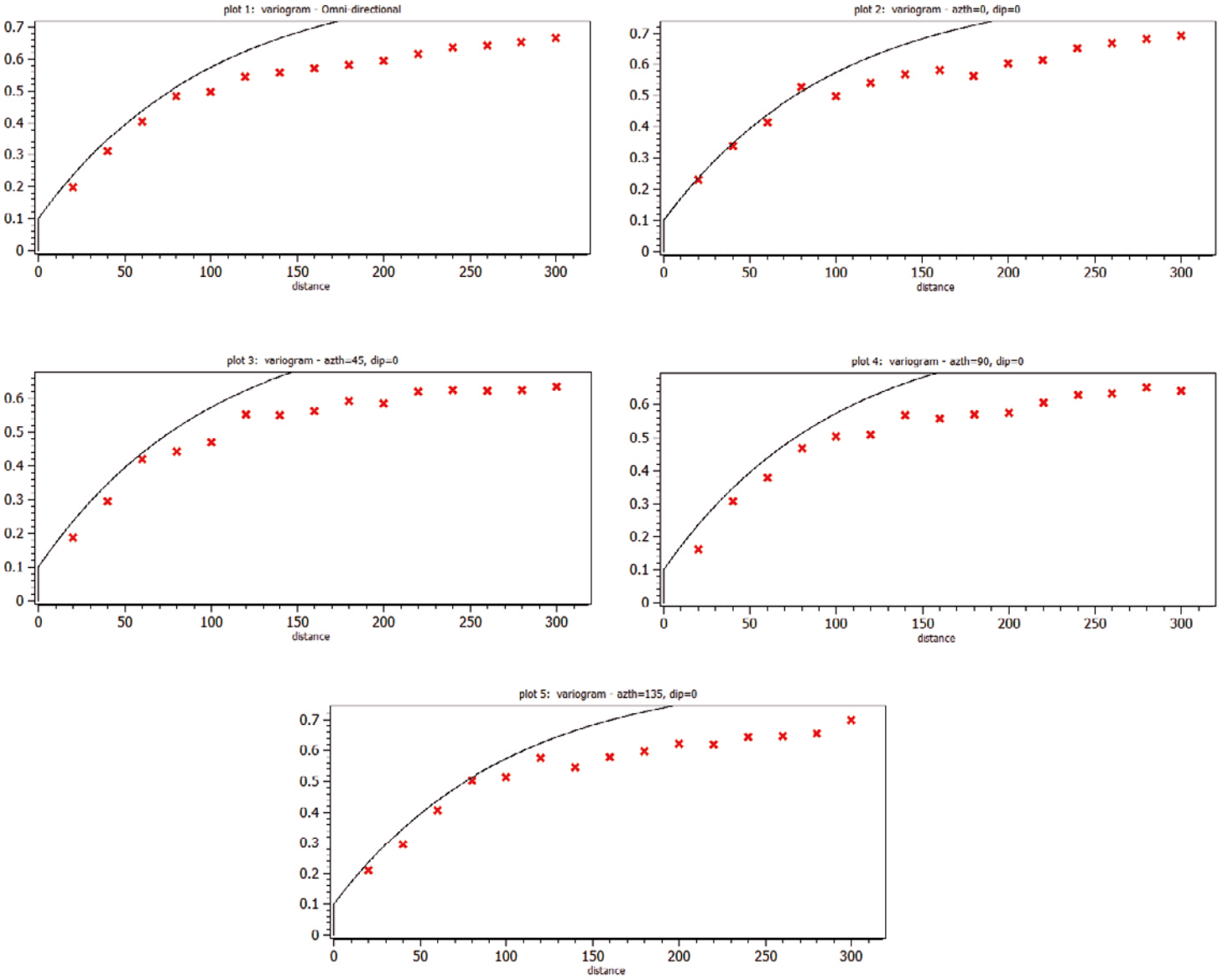

Figure 5-10. *Omnidirectional variogram and the four directional variograms (at 0, 45, 90 and 135 degrees) as obtained by SGeMS after utilising the 4898 points of the upscaled transmissivity.*

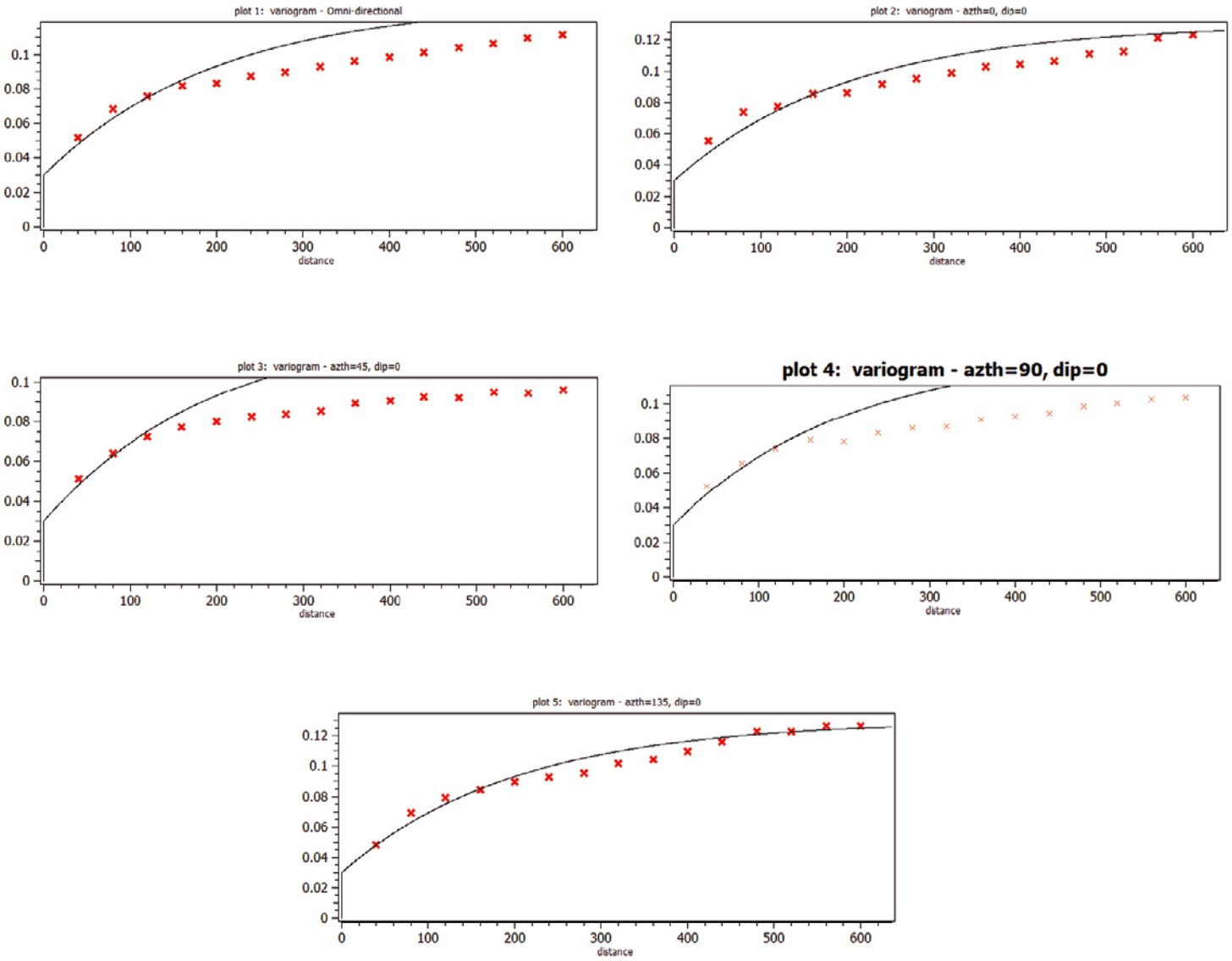

Figure 5-11. *Omnidirectional variogram and the four directional variograms (at 0, 45, 90 and 135 degrees) as obtained by SGeMS after utilising the 4898 points of the upscaled porosity*

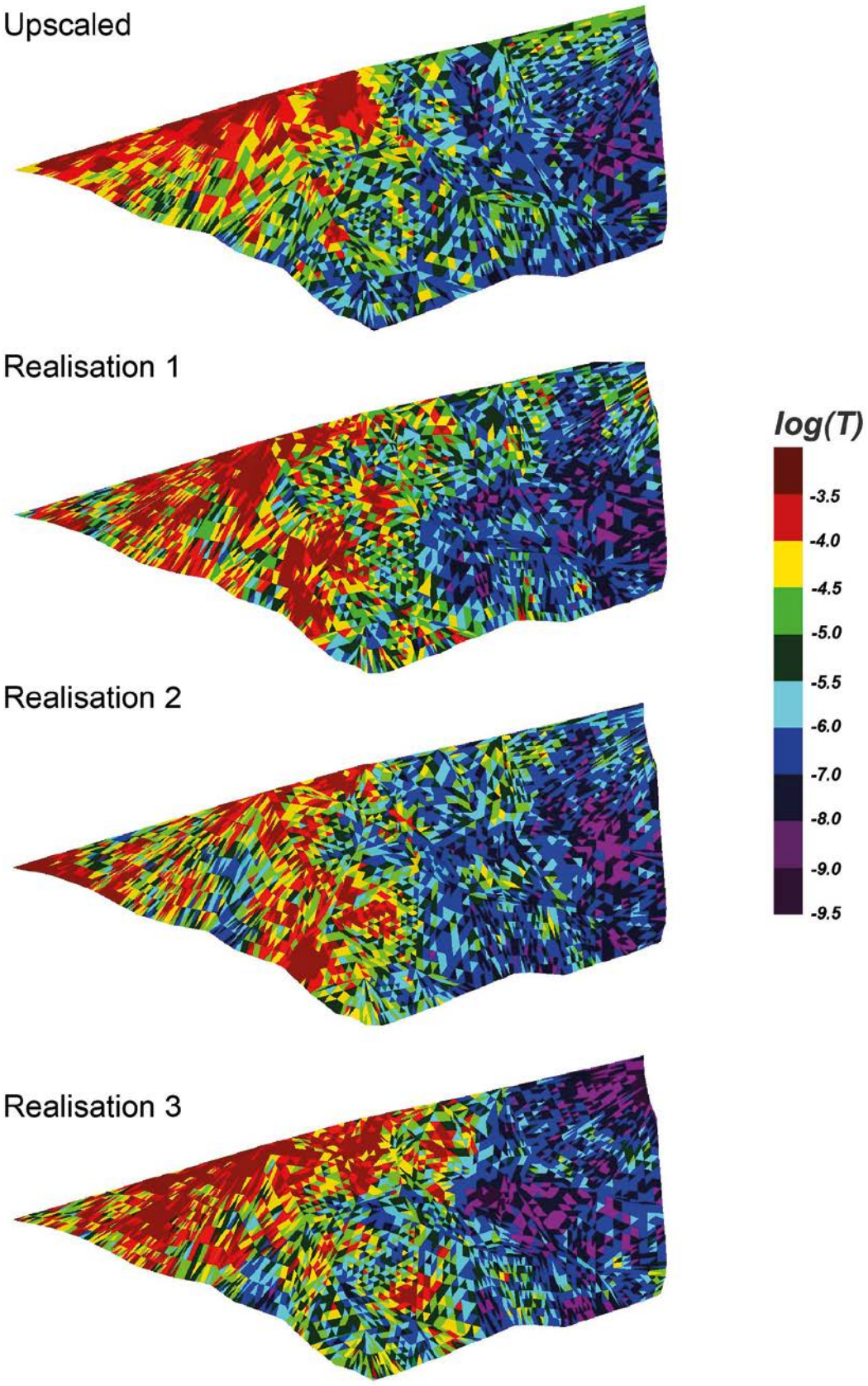

Figure 5-12. *Transmissivity for the original upscaled DFN and three realisations of the Gaussian Simulated transmissivity for BFZ020a.*

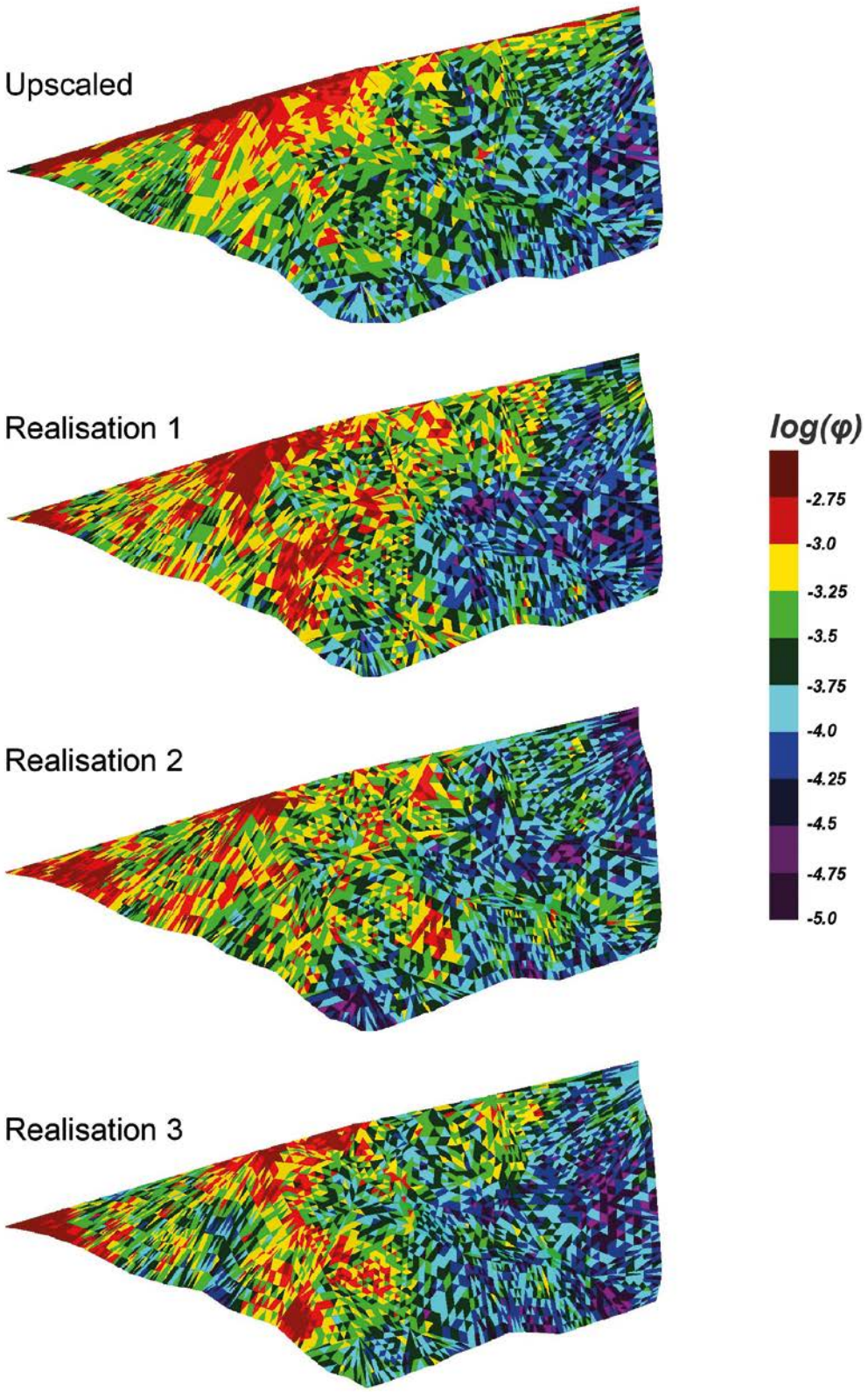

Figure 5-13. *Porosity for the original upscaled DFN and three realisations of the Gaussian Simulated transmissivity for BFZ020a.*

6 Summary and conclusions

In consultation with SKB, Posiva have been developing their methodology for DFN modelling toward the Olkiluoto SDM 2018. The DFN methodology has been elaborated to achieve greater integration between geological sub-models (ductile domains, lithology, and brittle deformation zones) and hydro-geological models. One key element of these methodology changes is the integration of structural/ geometrical DFN descriptions with hydrogeological ones into a single DFN model covering both aspects. In the new methodology, BFZ are modelled as zones of individual fractures each having their properties sampled from statistical distributions, rather than being modelled as a single triangulated surface with effective hydraulic and transport properties.

Although this methodology is an improvement in many aspects, it carries an increased computational cost; for example, it is likely not feasible to use the explicit swarm representation of BFZ to carry out all of the site-scale particle tracking transport calculations required in a typical safety assessment. Thus, a need arises for reducing the computational burden of transport calculations while preserving as much as possible the desirable features of the swarm representation, such as its small-scale heterogeneity structure and directionality. Furthermore, the effective properties implied by either an explicit DFN swarm or upscaled ECPM representation can be difficult to communicate, as can the sensitivity of those properties to uncertain DFN parameters such as size distribution and intensity.

As such, this study details the development of methodologies to upscale components of DFN models to simplified and computationally tractable representation of key features, by deriving ECPM properties on a suitable grid and simplifying the representation of BFZ modelled as fracture swarms to equivalent properties on a planar representation. In each case the developed methods have been evaluated through application to ODFN 3.0 (Hartley et al. 2018), the current DFN model developed in support of the Olkiluoto SDM 2018. Specifically, this report addresses the following three objectives:

1. A methodology has been derived to accurately calculate geocellular transport parameters (travel time and flow-related transport resistance) and their statistics, and use these to also derive ECPM properties for both the background fractures and fault zones. The key conclusions for this objective are summarised in Section 6.1.
2. Through the ECPM properties derived in objective 1, a methodology is developed to upscale these grid cell properties onto the mid-plane of the zone providing effective transmissivity, transport aperture, and flow wetted surface, as well as thickness. The key conclusions for this objective are summarised in Section 6.2.
3. The planar BFZs developed in objective 2 are further analysed for the variability in effective transmissivity and porosity, to provide a geostatistical model to enable the generation of realisations of transmissivity and porosity as an expedient way to assess stochastic uncertainty without having to run and upscale many DFN realisations. The key conclusions for this objective are summarised in Section 6.3.

6.1 Transport-based upscaling

Current upscaling approaches evaluate the equivalent kinematic porosity on a grid cell as the sum of the fracture area times transport aperture of each connected fracture within the element, while the fracture surface area is calculated as the sum of the area. As such, the transport properties derived through this methodology are simple geometric approximations that do not reflect effects of hetero-geneity, channelling or hydraulic gradient. A better approach is to use flow paths through each grid cell to obtain a distribution of travel times, tortuosity and flow resistance for each direction and each element which can subsequently be used to derive equivalent porosity and fracture surface area for the grid cells. Therefore, the first objective of this study was the development of a methodology to accu-rately calculate geocellular transport parameters using a flow-based estimation (as opposed to existing techniques using a geometric approach). Evaluation of block scale models as well as comparison on ODFN 3.0 scale models indicate that transport properties are reasonably consistent between the two upscaling methodologies (flow-based and geometric-based). However, it is noteworthy that

neither method can reproduce all of the details and heterogeneity of the discrete fracture network representation and should not be seen as an alternative for that representation. Instead they should be considered as an alternative conceptual approach, particularly applicable for instances where ECPM models currently provide the only available approach for performing particular calculations in codes such as ConnectFlow. This can be due to considerations of practicality (i.e. models which are larger or over longer timescales than can practically be solved in a DFN) or capability (i.e. models containing physics which cannot currently be included in a DFN calculation, e.g. radionuclide or heat transport).

The analysis performed in this study indicates the flow-based approach for derivation of transport properties forms a robust method. However, one aspect for further consideration would be the dependence of upscaled properties on both the cell size and small fracture cut-off size (i.e. the selection of the right cell size for the application).

6.2 Plane upscaling of BFZ properties

A key feature of the latest ODFN 3.0 model developed for the Olkiluoto site is an updated methodology to model fault zones as swarms of individual fractures, each having their properties sampled from statistical distributions, rather than modelling them as a single triangulated plane (or surface) with effective hydraulic and transport properties. However, although this methodology provides a well-founded approach to the property description of the fault zones, it is often appropriate and necessary to provide a planar representation of the faults, and as such, equivalent properties for this planar structure are required. The second objective of this study involved the development of a methodology to process this conceptual representation of fault zones to derive the effective in-plane transmissivity, porosity and flow wetted surface of each fault. The approach adopted first requires the ODFN 3.0 model (comprising background rock fractures and fault zone fracture swarms) to be upscaled to an ECPM model based on the methodology defined in Chapter 3 (see summary in Section 6.1). Note that, when determining upscaled properties for fault zones, a careful choice is required for the size of grid cells used, with a small size typically appropriate. The thickness of faults at Olkiluoto varies from less than 1 m up to about 30 m, and therefore the typical grid cell should be scaled similarly, to ensure the fault zone fracture swarm dominates the upscaled properties. The derived upscaled properties can then be processed by overlaying the geometrical description of the fault (mid-plane, extent and damage zone thickness) and identifying the grid cells from the upscaled model that are associated with each zone. These grid cells can then be aggregated to determine properties for transmissivity, porosity and flow wetted surface on the mid-plane representation of each fault zone, providing a single triangulated mid-plane surface with effective hydraulic and transport properties for each fault.

The above methodology has been assessed in the context of the interpreted fault zones at Olkiluoto. The following two confirmatory analyses were performed:

- Upward and downward fluxes were calculated at the island scale, with the contribution from the characterised faults extracted. All 298 BFZ in the Olkiluoto version 3 model were represented using the projection methodology defined here and compared to the ODFN 3.0 fracture swarm representation.
- Pathline simulations were performed with release points randomly sampled across six of the major fault zones at Olkiluoto; these are either the faults with the most characterisation data or those with atypically large flows and/or direct influence on the repository layout.

In both cases, simulations representing fault zones as fracture swarms versus their equivalent upscaled mid-plane representation indicate that the fault mid-planes can sometimes over-predict flow by up to a factor of two. This is likely a consequence of the increased connectivity due to simplification of the fault geometry to continuous planes, a limitation in the plane-projected representation which is emphasised for faults with particularly low fracture intensity or thickness.

6.3 Geostatistical models for planar BFZ

The processes of upscaling fracture swarms representing fault zones to equivalent planar properties is a significant computational task, requiring generation of first the DFN model of the faults, subsequent upscaling to ECPM properties and finally processing to equivalent planar values. As such, the assessment of the statistical uncertainty associated with the upscaled fault zones, requiring a number of different stochastic realisations to be generated, can be a time-consuming task. Therefore, the third objective of this study considers a geostatistical analysis of the upscaled faults to further analyse the variability in effective transmissivity and porosity to enable the generation of realisations of the planar fault zone model expediently. The approach adopted prototypes the use of SGeMS to provide an implementation of a sequential Gaussian simulation (SGSIM) algorithm. Computationally the method is light and enables the generation of the desired number of realisations, without having to regenerate the underling fracture network and upscale. Three realisations of transmissivity and porosity for BFZ020a have been generated, and in each case the global trends across the structure are reproduced in each of the realisations, with Gaussian simulation providing a localised variability between realisations.

Although the methodology presented in this study forms only a prototype of a geostatistical approach for representing uncertainty within the fault zones, its benefits are readily apparent. However, to develop this approach further, the following should be considered:

- Development of an approach to combine Gaussian simulation of the uncertainty in upscaled properties with local conditioning on measurements (e.g. transmissivities) at the drillhole intersects.
- Currently, the geostatistics derived for transmissivity and porosity are independent, as are the Gaussian simulations performed. However, these properties are related (e.g. from the underlying upscaling, an increased flow through a cell is likely a consequence of larger aperture fractures/ increased intensity of fractures which will result in both an elevated transmissivity and porosity when upscaled to the fault zone mid-plane). An approach for correlating these properties within the geostatistics could be investigated.

References

SKB's (Svensk Kärnbränslehantering AB) publications can be found at www.skb.com/publications.

Aaltonen I (ed), Kosunen P, Mattila J, Engström J, Paananen M, Paulamäki S, Front K, Gehör S, Kärki A, 2016. Geology of Olkiluoto. Posiva 2016-16, Posiva Oy, Finland.

Abelin H, Birgersson L, Widén H, Ågren T, Moreno L, Neretnieks I, 1994. Channeling experiments in crystalline fractured rocks. Journal of Contaminant Hydrology 15, 129–158.

Al Qassab H M, Al Khalifa M A, Al-Ali Z, Ameen M, Phillips R, Hartley L, 2002. New integrated 3D-fracture modeling and flow simulation study: A giant Saudi Arabian carbonate reservoir. Europec 2002, Aberdeen, UK, 29–31 October 2002. SPE 78295, Society of Petroleum Engineers.

Baxter S, Hartley L, Witterick W, Fox A, 2016. Database design and prototyping for Olkiluoto discrete fracture network (DFN) in support of site descriptive modelling 2016. Posiva Working Report 2016-13, Posiva Oy, Finland.

Brown S R, Scholz C H, 1985. Broad bandwidth study of the topography of natural rock surfaces. Journal of Geophysical Research 90, 12575–12582.

Glover P W J, Matsuki K, Hikima R, Hayashi K, 1998. Fluid flow in synthetic rough fractures and application to the Hachimantai geothermal hot dry rock test site. Journal of Geophysical Research 103, 9621–9635.

Hartley L, Appleyard P, Baxter S, Hoek J, Roberts D, Swan D, 2012. Development of a hydrogeological discrete fracture network model for the Olkiluoto site descriptive model 2011. Volume I. Posiva Working Report 2012-32, Posiva Oy, Finland.

Hartley L, Appleyard P, Baxter S, Mosley K, Williams T, Fox A, 2017. Demonstration area discrete fracture network modelling at Olkiluoto. Posiva Working Report 2017-31, Posiva Oy, Finland.

Hartley L, Appleyard P, Baxter S, Hoek J, Joyce S, Mosley K, Williams T, Fox A, Cottrell M, La Pointe P, Gehör S, Darcel C, Le Goc R, Aaltonen I, Vanhanarkaus O, Löfman J, Poteri A, 2018. Discrete fracture network modelling (version 3) in support of Olkiluoto site description 2018. Posiva Working Report 2017-32, Posiva Oy, Finland.

Jackson C P, Hoch A R, Todman S, 2000. Self-consistency of a heterogeneous continuum porous medium representation of a fractured medium. Water Resources Research 36, 189–202.

Joyce S, Simpson T, Hartley L, Applegate D, Hoek J, Jackson P, Swan D, Marsic N, Follin S, 2010. Groundwater flow modelling of periods with temperate climate conditions – Forsmark. SKB R-09-20, Svensk Kärnbränslehantering AB.

Marsic N, Hartley L, Jackson P, Poole M, Morvik A, 2001. Development of hydrogeological modelling tools based on NAMMU. SKB R-01-49, Svensk Kärnbränslehantering AB.

Posiva, 2012. Olkiluoto site description 2011. Posiva 2011-02, Posiva Oy, Finland.

Remy N, Boucher A, Wu J, 2011. Applied geostatistics with SGeMS: A user's guide. Cambridge: Cambridge University Press. doi:10.1017/CBO9781139150019

Vaittinen T, Ahokas H, Nummela J, Pentti E, Paulamäki S, 2019. Hydrogeological Structure Model of the Olkiluoto Site – Update in 2015. Posiva Working Report 2019-06, Posiva Oy, Finland.

Willis-Richards J, Watanabe K, Takahashi H, 1996. Progress toward a stochastic rock mechanics model of engineered geothermal systems. Journal of Geophysical Research 101, 17481–17496.

Wood, 2016a. ConnectFlow Technical Summary. Release 11.4. Harwell, UK: Wood.

Wood, 2016b. ConnectFlow Verification. Release 11.4. Harwell, UK: Wood.

Arkitektkopia AB, Bromma, 2019

SKB is responsible for managing spent nuclear fuel and radioactive waste produced by the Swedish nuclear power plants such that man and the environment are protected in the near and distant future.

skb.se